

Structure of two-dimensional multilayers and topological superconductors: surfactant mediated growth, intercalation, and doping

You-Ron Lin

Information

Band / Volume 99

ISBN 978-3-95806-716-5

Forschungszentrum Jülich GmbH
Peter Grünberg Institut (PGI)
Quantum Nanoscience (PGI-3)

Structure of two-dimensional multilayers and topological superconductors: surfactant mediated growth, intercalation, and doping

You-Ron Lin

Schriften des Forschungszentrums Jülich
Reihe Information / Information

Band / Volume 99

ISSN 1866-1777

ISBN 978-3-95806-716-5

Bibliografische Information der Deutschen Nationalbibliothek.
Die Deutsche Nationalbibliothek verzeichnet diese Publikation in der
Deutschen Nationalbibliografie; detaillierte Bibliografische Daten
sind im Internet über <http://dnb.d-nb.de> abrufbar.

Herausgeber und Vertrieb: Forschungszentrum Jülich GmbH
Zentralbibliothek, Verlag
52425 Jülich
Tel.: +49 2461 61-5368
Fax: +49 2461 61-6103
zb-publikation@fz-juelich.de
www.fz-juelich.de/zb

Umschlaggestaltung: Grafische Medien, Forschungszentrum Jülich GmbH

Druck: Grafische Medien, Forschungszentrum Jülich GmbH

Copyright: Forschungszentrum Jülich 2023

Schriften des Forschungszentrums Jülich
Reihe Information / Information, Band / Volume 99

D 82 (Diss. RWTH Aachen University, 2023)

ISSN 1866-1777
ISBN 978-3-95806-716-5

Vollständig frei verfügbar über das Publikationsportal des Forschungszentrums Jülich (JuSER)
unter www.fz-juelich.de/zb/openaccess.



This is an Open Access publication distributed under the terms of the [Creative Commons Attribution License 4.0](https://creativecommons.org/licenses/by/4.0/), which permits unrestricted use, distribution, and reproduction in any medium, provided the original work is properly cited.

Acknowledgments

I would like to thank all the people who have supported me and contributed to the research presented in this work:

- Prof. Dr. Christian Kumpf, thank you for providing me the chance to experience the fruitful and happy four years in the world of solid states material research. Your warmth toward colleagues and students is one of the most memorable things I experienced during my 6.5 years stay in Germany. I am grateful to have you as my *Doktorvater* and an example as a group leader.
- Prof. Dr. Moritz Sokolowski, thank you for co-refereeing my PhD thesis. Even though the chance to work with your team was not given during my stay in PGI-3, I could attend several conferences and listen to your lectures. The long-lasting collaboration and friendship in scientific research between you and the professors in PGI-3 are one of the beautiful things I admire.
- Dr. François C. Bocquet, thank you for guiding me through my entire PhD research as a senior. The delightful teamwork we have is very special to me. Your bitter laughter when experiments don't go well relieves me, that even such an outstanding experimentalist like you cannot have everyday in the lab go as planned.
- Prof. Dr. F. Stefan Tautz, thank you for managing the PGI-3 institute and providing the infrastructure for the research in this work. Your leadership and knowledge as head of the institute have set a standard for me. Thank you especially for all the input during submissions of the publications.
- Prof. Dr. Yoichi Ando, Dr. Jens Brede and Mahasweta Bagchi, thank you for providing the Bi_2Se_3 samples and the intriguing topic for the collaboration. For Jens and Sweta, special thanks for the nice time together at the beamtime and the effort writing the publication as a team.

- Prof. Dr. Thomas Seyller and Susanne Wolff, thank you for offering the Sb-intercalated graphene sample and the pleasant collaboration. It is my pleasure to contribute to the graphene Sb-intercalation topic.
- I09 beamline staff, thank you for your prudent support at the beamline, where all the NIXSW measurements in this work were carried out. Special thanks to Dr. Tien-Lin Lee for the thoughtful assistance and warmth as a fellow Taiwanese abroad.
- Markus Franke and Shayan Parhizkar, thank you for taking my hands through the learning curve when I started at PGI-3. There was so much fun with you in the labs. I will always remember the fun times with you guys.
- All colleagues at PGI-3, thank you for the company and conversations during the 3.5 years. Your support and experience in the field of experiments has been important aid for me.
- My volleyball team SV Neptun Aachen D3, you guys supported me mentally with chitchat and workout. Without the fun with you, I wouldn't have started my PhD and couldn't have completed it. Cheers to volleyball and the team spirit!
- My family and friends, thank you for the support and company apart from work. A relaxing afternoon coffee or a long chat with anyone of you has been important to get the next week going.

Contents

1	Introduction	1
2	Experimental techniques	7
2.1	Low energy electron diffraction	7
2.1.1	Spot-profile analysis LEED	8
2.1.2	Diffraction image correction	10
2.2	Photoelectron spectroscopy	16
2.2.1	Theoretical description of photoelectron spectroscopy	16
2.2.2	The photoemission spectroscopy experiment	18
2.3	The normal incidence x-ray standing wave technique	21
2.3.1	Photoelectron emission process in NIXSW	21
2.3.2	Experimental setup at I09 beamline at the DLS	25
3	Epitaxial boron nitride on 6H-SiC(0001)	27
3.1	Sample preparation	28
3.2	Electronic structure and air stability	29
3.3	Growth temperature dependency	32
3.4	Lateral structure	35
3.5	Vertical structure	38
3.6	Conclusion	43
4	0°-rotated Graphene on 6H-SiC(0001)	45
4.1	Lateral structure	46
4.2	Electronic band structure	52
4.3	Vertical structure	54
4.4	Conclusion	61
5	Sb-intercalated freestanding monolayer graphene	63
5.1	Sample preparation	65
5.2	NIXSW Experiment	65
5.3	Conclusion	70

6	Sr-doped and pristine bismuth selenide	71
6.1	Introduction	71
6.2	Sample preparation	73
6.3	Vertical structure revealed by NIXSW	75
6.3.1	Structure model	75
6.3.2	NIXSW data	75
6.3.3	The effect of a finite inelastic mean free path	76
6.3.4	Strontium sites in $\text{Sr}_x\text{Bi}_2\text{Se}_3$	81
6.4	Conclusion	85
7	Summary	87

List of acronyms

2D	two-dimensional
ARPES	angular-resolved photoelectron spectroscopy
BN	boron nitride
BZ	Brillouin zone
DFT	density-functional theory
EDM	energy distribution maps
EG	epitaxial graphene
EMLG	epitaxial monolayer graphene
FWHM	full width at half-maximum
hBN	hexagonal boron nitride
IMFP	inelastic mean free path
LEED	low energy electron diffraction
lqG	low-quality graphene
MCP-LEED	multi-channel plate low energy electron diffraction
ML	monolayer
NIXSW	normal-incidence x-ray standing wave
PES	photoelectron spectroscopy
QFMLG	quasi-freestanding monolayer graphene
QL	quintuple layer
SiC	silicon carbide
SPA-LEED	spot-profile low energy electron diffraction
STM	scanning tunneling microscopy
tBLG	twisted bilayer graphene
TEM	transmission electron microscopy
UHV	ultra-high vacuum
UPS	ultra-violet photoelectron spectroscopy
UV	ultra-violet

Contents

vdW	van der Waal
XPS	x-ray photoelectron spectroscopy
XRD	x-ray diffraction
XSW	x-ray standing wave
ZL	zeroth-layer (or bufferlayer)
ZLG	zeroth-layer graphene (or carbon bufferlayer)
P_e^H	coherent position
F_e^H	coherent fraction

List of Figures

2.1	Schematic of the LEED instrument and the Ewald's construction.	8
2.2	Schematic of a SPA-LEED apparatus and the Ewald's construction.	9
2.3	Screenshot of the WinSPA software.	13
2.4	Screenshot of the LEEDCal software.	14
2.5	Comparison of uncorrected and corrected SPA-LEED images.	15
2.6	Schematic of the photoemission process.	16
2.7	Schematic of the ARPES measurement principle.	19
2.8	Schematic of the ESCA chamber.	20
2.9	Schematic of the XSW at the crystal surface.	22
2.10	Geometry of the NIXSW measurement.	24
2.11	Schematic of the I09 beamline at Diamond Light Source.	26
3.1	ARPES EDMs of (3×3) SiC surface and $B_xN_y-R0^\circ$.	30
3.2	LEED patterns of a $B_xN_y-R0^\circ$ sample before and after air exposure.	31
3.3	Band map of lqG- $R0^\circ$ prepared at 1225°C .	31
3.4	Hard- and soft x-ray core-level spectra of the gradient sample.	33
3.5	Integrated core-level components of the gradient sample.	34
3.6	LEED images of the gradient sample.	35
3.7	SPA-LEED images of $B_xN_y-R0^\circ$ prepared at 1150°C and 1100°C .	36
3.8	Core-level spectra and yield curves of $B_xN_y-R0^\circ$.	39
3.9	Argand diagrams summarizing NIXSW results of $B_xN_y-R0^\circ$ and lqG- $R0^\circ$ on SiC.	41
3.10	Ball-and-stick model of $B_xN_y-R0^\circ$, lqG- $R0^\circ$ and EMLG on SiC.	42
4.1	SPA-LEED images of $B_xN_y-R0^\circ$, lqG- $R0^\circ$ and T graphene.	47
4.2	Step-by-step geometrical construction to explain the origin of diffraction spots of G- $R0^\circ$.	48
4.3	SPA-LEED images of T graphene and S graphene.	50
4.4	SPA-LEED image of G- $R0^\circ$ and diffraction spot profiles.	51
4.5	ARPES EDMs of G- $R0^\circ$ prepared at different temperatures.	53
4.6	Core-level spectra, yield curves and Argand diagram of G- $R0^\circ$.	55

List of Figures

4.7	Intensity of the core-level component G on the gradient sample.	59
4.8	Coverage model for T graphene.	60
5.1	Soft XPS of Sb $3d$ on Sb-QFMLG.	66
5.2	Core-level spectra and yield curves of Sb-QFMLG.	68
5.3	Ball-and-stick models of ZLG- $R30^\circ$ and Sb-QFMLG.	70
6.1	Ball-and-stick model of the Bi_2Se_3 bulk crystal and electron intensity attenuation.	74
6.2	Core-level spectra and yield curves of $\text{Sr}_x\text{Bi}_2\text{Se}_3$	77
6.3	Soft x-ray core-level spectra of Bi_2Se_3 and $\text{Sr}_x\text{Bi}_2\text{Se}_3$	78
6.4	Argand diagram of the Bi_2Se_3 NIXSW result.	80
6.5	Simulation of all possible Sr sites.	82

List of Tables

3.1	NIXSW results of the $B_xN_y-R0^\circ$ sample prepared at 1150°C and the $lqG-R0^\circ$ sample prepared at 1250°C	40
3.2	Bond length analysis for $B_xN_y-R0^\circ$ and $lqG-R0^\circ$ to the ZL.	43
4.1	Color code used in Fig. 4.2 and Fig. 4.4.	47
5.1	NIXSW results of Sb-intercalated QFMLG.	69
6.1	NIXSW results of Bi_2Se_3 and $Sr_xBi_2Se_3$	76

List of own Publications

Papers included in this thesis:

Surfactant-Mediated Epitaxial Growth of Single-Layer Graphene in an Unconventional Orientation on SiC

F. C. Bocquet, You-Ron Lin, M. Franke, N. Samiseresht, S. Parhizkar,
S. Soubatch, T.-L. Lee, C. Kumpf, and F. S. Tautz
Phys. Rev. Lett. **125**, 106102, (2020)

Vertical structure of Sb-intercalated quasifreestanding graphene on SiC(0001)

You-Ron Lin, S. Wolff, P. Schädlich, M. Hutter, S. Soubatch, T.-L. Lee,
F. S. Tautz, T. Seyller, C. Kumpf, and F. C. Bocquet
Phys. Rev. B **106**, 155418, (2022)

Boron nitride on SiC(0001)

You-Ron Lin, M. Franke, S. Parhizkar, M. Raths, V. W.-z. Yu, T.-L. Lee,
S. Soubatch, V. Blum, F. S. Tautz, C. Kumpf, and F. C. Bocquet
Phys. Rev. Materials **6**, 064002, (2022)

The Vertical Position of Sr Dopants in the Sr_xBi₂Se₃ Superconductor

You-Ron Lin, M. Bagchi, S. Soubatch, T.-L. Lee, J. Brede, F. C. Bocquet,
C. Kumpf, Y. Ando, and F. S. Tautz
Phys. Rev. B **104**, 054506 (2021)

Not included in this thesis:

**Growth, domain structure, and atomic adsorption sites of hBN on
the Ni(111) surface**

M. Raths, C. Schott, J. Knippertz, M. Franke, You-Ron Lin, A. Haags,
M. Aeschlimann, C. Kumpf, B. Stadtmüller
Phys. Rev. Materials **5**, 094001, (2021)

Chapter 1

Introduction

For the past decades, the semiconductor industry has been pushing the technology development to meet Moore's Law's postulation, that the number of transistors in an IC of the same size doubles approximately every two years. Obviously, the miniaturization of device size, which is necessary for this, cannot go on forever. Novel materials as alternatives for Si-based semiconductors are therefore much desired. Other than replacing Si with SiGe in the channel area to have higher carrier mobility, materials with single and few atomic layers benefit the scale-down immensely. Bonded by mainly the van der Waals interaction between layers, the so-called "two-dimensional materials" (2D-materials) can be separated layer by layer. Materials with such crystal structure are found with conducting (e.g. NbSe₂, graphene), semiconducting, and insulating electronic properties, all needed to build the "smallest possible transistor". For example, graphene can not only act as contact layers for such vdW devices [1–3], but also can be used as the active layer itself [4, 5]. MoS₂, WS₂ and WSe₂ monolayers are semiconductors with direct bandgaps and can be used for the fabrication of phototransistors, photodetectors, and photomemories [6]. Hexagonal boron nitride (hBN) has a bandgap of about 6 eV and hence can serve as an insulating capping layer in a 2D-transistor [5].

By stacking the 2D-materials with designed orientations and layer thicknesses, one makes so-called "van der Waals heterostructures", which show intriguing electronic properties. Just to name a few, graphene/hBN stacking shows an improvement in the homogeneity of charge density compared to the graphene/SiO₂ [5]. Another example is a WS₂-graphene-based tunneling transistor that shows a high on/off ratio up to 10⁶, which can function on a flexible and transparent substrate as well [1].

Graphene, as the first 2D-material discovered in the breakthrough of the vdW materials, is the thinnest material yet the strongest ever measured [7–9]. Its unusual bandstructure offers possibilities to controllable valleytronics [10]. It develops supercurrent when attached to superconducting contacts [11]. And

graphene in one-dimensional form - as carbon nanoribbons - shows 1000 times higher carrier mobility than bulk silicon [12, 13]. When breaking the valley degeneracy, graphene quantum dots can host spin qubits [14]. Qubits are the fundamental unit in quantum computing, similar to bits in digital computing. Physical hosts for qubits in the next-generation quantum computers are what scientists seek at present. In Ref. [14], several graphene quantum dot structures were suggested as hosts of qubits, e.g. graphene nanoribbons with armchair boundaries or single- or bilayer graphene.

Creating a bandgap opening is a challenging topic for graphene [15] when it comes to an application as a semiconductor. Therefore, numerous studies (see Ref. [16] and references therein) were carried out to explore possibilities for engineering the bandgap of graphene. Not only does the underlying substrate affect the bandgap of graphene [17, 18], the twist angle between two graphene monolayers can also be tuned [19–24]. Two chapters in this work are therefore dedicated to graphene on SiC and its related structure induced by the precursor molecule, to control the lattice orientation of graphene during epitaxial growth.

Besides 2D-materials, also superconducting materials have been a long-lasting topic because of their potential for applications in digital circuits, superconducting magnets, superconducting quantum interference devices (SQUIDs), etc. [25]. In recent years, the so-called "topological superconductors" gained more and more interest. A topological insulator is insulating in its bulk state while its topological surface state exhibits metallic properties. By doping a topological insulator (e.g. Bi_2Se_3) with metallic elements (e.g. Cu, Sr), it is possible to make topological superconductors, such as $\text{Cu}_x\text{Bi}_2\text{Se}_3$ and $\text{Sr}_x\text{Bi}_2\text{Se}_3$ [26]. Understanding the origin of this kind of superconductivity is an important step to optimize superconducting materials. By finding the positions of dopants in the crystal structure, we may be able to answer this question. However, the very little dopant concentration makes it difficult to measure their positions precisely. Therefore, the last chapter of this work is dedicated to the structural determination of Sr dopant in superconducting $\text{Sr}_x\text{Bi}_2\text{Se}_3$ crystal.

This work is located in this emerging working field and utilizes diffraction as well as spectroscopic methods to study crystal structures in detail. Besides one chapter for the theoretical and technical background of the probing methods and sample preparation (chapter 2), the experimental results are structured in three parts: (i) the borazine-mediated epitaxial growth of high-quality single-layer graphene on SiC in an unusual orientation (chapter 4) and it's the boron-nitride intermediate phase (chapter 3), (ii) intercalation of atomic Sb underneath high-quality graphene epitaxially grown on SiC (chapter 5), and (iii) a structural study of the Sr-doped Bi_2Se_3 , aiming for a better understanding of topological superconductivity (chapter 6).

Epitaxial graphene on SiC

After the exfoliation of graphene monolayers, bilayer graphene was found to have very different electronic properties than its monolayer counterpart [27]. While investigating possibilities for stacking graphene bilayers, the twist angle between the bilayer emerges as an important parameter that impacts the hybridization of bandstructures [19, 28]. Besides the twisted-bilayer graphene (tBLG) with 1.1° twist angle that shows superconductivity [20, 21, 23], the 30° -twisted bilayer graphene (30° -tBLG) shows bandgap opening at Dirac points that is induced via Umklapp scattering [29, 30]. For controlled angles between graphene layers with respect to each other or to the substrate lattice, exfoliation has been the main method used to prepare samples for such researches [19–21, 23, 24]. However, exfoliation is not scalable and hardly reproducible. With the ultimate aim of material research being applicable in future industrial products, epitaxial growth of graphene provides a potential solution for mass production [31–34], for which the scalability and reproducibility are indispensable.

In this work, a step forward on the way to an optimal preparation recipe for high-quality single-layer graphene with 0° rotation with respect to the SiC substrate ($G-R0^\circ$) is presented. This could pave the way towards 30° -tBLG. The graphene samples in this work are prepared via thermal decomposition, where a piece of SiC wafer is annealed in either UHV or borazine atmosphere. During the heating process, Si atoms in the SiC wafer sublimate, and the excessive carbon atoms remaining on the surface form graphene, which is then located on a boron or carbon bufferlayer (or zeroth-layer) on the Si-terminated substrate. It is found that the preparation temperature affects the stacked system in its chemical composition, also its lateral and vertical structure. In this work, the stacked system prepared between 1100°C and 1250°C will be presented in chapter 3. Based on the knowledge collected from studying this system, high-quality $G-R0^\circ$ could be prepared at 1300°C , see chapter 4.

The lateral structure is quantitatively studied using spot-profile analysis low electron energy diffraction (SPA-LEED) while the vertical structure model is proposed based on normal-incidence x-ray standing wave (NIXSW) measurements. The electronic bandstructure of the structures is measured with angular-resolved photoemission spectroscopy (ARPES).

Sb-intercalated graphene on SiC

Intercalation is a useful method to decouple 2D-layers from the bulk crystals. For epitaxial graphene (EG) grown from SiC via thermal decomposition, the formation of a zeroth-layer (ZL) between the graphene layer(s) and the SiC substrate is inevitable [35–37]. However, the ZL scatters charge carriers and reduces carrier mobility in the graphene layers [38, 39]. With intercalation of atomic species into the ZL/SiC interface, quasi-freestanding graphene monolayers can be obtained, which demonstrated much-improved device performance [40]. Prominent examples of atomic species that have been successfully intercalated on the EG/SiC system are H, O, Ge, and Pd [41–48]. The typical way to intercalate atomic species is to deposit metallic atoms onto the EG/SiC sample via sublimation, sputtering, or evaporation from a Knudsen-cell, and then anneal the sample to temperature $> 600^\circ\text{C}$ in UHV [48, 50, 51]. In contrast to the UHV method, intercalation of elements from gaseous precursors (H and O) is usually performed under atmospheric pressure [41, 46, 53].

Recently, Wolff *et al.* demonstrated that atomic antimony (Sb) can also be intercalated in the ZL/SiC interface [49]. They annealed a μm -thick Sb layer that was deposited on ZL/SiC under 1 bar Ar atmosphere, and show that a quasi-freestanding graphene monolayer can be obtained in this way. However, the thickness of the intercalated Sb-layer was unknown so far. Since the thickness of the intercalated layer may impact the electronic properties of graphene on top, as already shown for the case of Ag intercalation [54], a chapter in this work is dedicated to answering this question. In chapter 5, the vertical structure of the Sb-intercalated quasi-freestanding graphene is determined using NIXSW technique.

Sr-doped bismuth selenide

As mentioned before, researchers are eager to understand the origin of topological superconductivity in order to further optimize it. One may find the answer by determining the positions of the dopants in topological superconducting crystals. The positions of dopants in topological superconductors such as $\text{Cu}_x\text{Bi}_2\text{Se}_3$ and $\text{Sr}_x\text{Bi}_2\text{Se}_3$ have been debated for the last decade [55–64]. Although defect sites of intrinsic Bi_2Se_3 can provide some hints for possible dopant positions [62, 63], there has been no direct evidence for specific dopant positions in the unit cell so far.

Hor *et al.* proposed that Cu dopants mainly reside in the van der Waals gap [55], and this became a common belief for studies thereafter. M. Wang *et al.* used first-principle calculations to simulate the structure of Cu-doped Bi_2Se_3 and proposed five favorable sites for Cu dopants [56]. Shruti *et al.* suggest Sr dopants locate in the van der Waals gaps [58]. However, with both high-angle annular dark-field scanning transmission electron microscopy (HAADF-STEM) and reflection high-energy electron diffraction (RHEED), Y.-L. Wang *et al.* could only conclude that the Sr atoms are possibly mobile within the van der Waals gaps and therefore difficult to detect [64]. Froehlich *et al.* used neutron diffraction to detect Cu dopant position with no clear conclusion [61].

In this work, the vertical dopant positions of Sr atoms of topological superconducting Sr-doped Bi_2Se_3 crystal could be unambiguously determined, as reported in chapter 6. This study is based on NIXSW, under consideration of the inelastic mean free path of electrons in matter. Our result clearly shows that the Sr dopants are located within the quintuple layers and not in the van der Waals gaps. This knowledge serves as an important step forward toward a better understanding of the origin of superconductivity in this and similar systems.

Chapter 2

Experimental techniques

The experimental techniques for sample characterization in this work require an ultra-high vacuum (UHV) environment to have the crystals and thin layers on top remain free of condensed water and contaminating particles. In this work, electron spectroscopy is used for the determination of the electronic structure. Electron diffraction and normal-incidence x-ray standing wave (NIXSW) technique is used for structural and geometrical determination. These techniques are non-destructive methods and show no beam damage on the systems studied in this work. Besides the above-mentioned advantages, electrons have an inelastic mean free path of several Ångströms at low kinetic energy between 30 to 100 eV [65] and hence can provide surface sensitive information of the sample.

2.1 Low energy electron diffraction

Low energy electron diffraction (LEED) is commonly used in surface science to characterize the lateral periodicity, such as lattice parameters and orientations, of crystals or layers adsorbed atop. Electrons with energies around 100 eV have the shortest mean free path in solids [65] and thus provide surface-sensitive information of the sample. An electron with a kinetic energy E can be described as a wave with wavelength $\lambda = \sqrt{h^2/2m_e E}$ and wave vector \mathbf{k} ($|\mathbf{k}| = \frac{2\pi}{\lambda}$). The electrons with wavelength λ which fulfill the Bragg condition $n\lambda = 2d \sin \theta$, where d is the lateral spacing of the crystal's lattice mesh and θ is the angle between the incidence beam and the diffraction plane, interfere constructively in the detector, resulting in a measurable diffraction intensity. A simplified illustration of the LEED instrument is shown in Fig. 2.1(a). The electron gun emits electrons with tunable energy around 100 eV. In general, only the electrons fulfilling the diffraction condition $\Delta\mathbf{k} = \mathbf{G}$, where \mathbf{G} is the reciprocal lattice vector, will be diffracted and can thus be imaged on the fluorescence

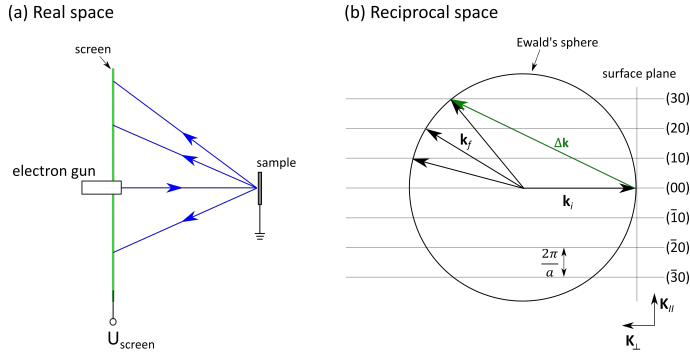


Figure 2.1: (a) Simplified illustration of the LEED technique in real space. Note that the LEED screen is exceptionally shown as flat here (true only for MCP-LEED). Usually it is a hemisphere. (b) Illustration of Ewald's construction in reciprocal space. Electrons with momentum \mathbf{k}_i hit the sample and get diffracted. The direction and length of \mathbf{k}_i are determined by the relative position of the electron gun to the sample and the electron energy, respectively. \mathbf{k}_f are wave vectors of all the elastically scattered electrons. At the points where they intersect with the reciprocal lattice rods, the two-dimensional diffraction condition $\Delta\mathbf{k}_{\parallel} = \mathbf{G}_{\parallel}$ is fulfilled ($\mathbf{G}_{\parallel} = (hk)$).

screen. As shown in Fig. 2.1(b), the Ewald's sphere is a graphical illustration of the diffraction equation $\Delta\mathbf{k} = \mathbf{G}$, representing all scattering vectors that fulfill the diffraction condition. The radius of the Ewald's sphere is $|\mathbf{k}_f| = |\mathbf{k}_i|$. In the case of electron diffraction, due to the small penetration depth of the electrons, the reciprocal lattice vectors lie on "diffraction rods" oriented perpendicular to the sample surface. The problem is hence two dimensional and only the components of $\Delta\mathbf{k}$ and \mathbf{G} parallel to the surface and the lateral lattice vectors \mathbf{a}_1 and \mathbf{a}_2 have to be considered: $\Delta\mathbf{k}_{\parallel} = \mathbf{k}_{f,\parallel} - \mathbf{k}_{i,\parallel} = \mathbf{G}_{\parallel} = h\mathbf{a}_1^* + k\mathbf{a}_2^*$, with \mathbf{a}_1^* and \mathbf{a}_2^* being the lateral reciprocal unit vectors.

2.1.1 Spot-profile analysis LEED

A SPA-LEED instrument [66] is constructed with four major parts: an electron gun, a set of octopole plates for electrostatic field control, an entrance lens to focus the electron beam, and a channeltron for electron detection, see Fig. 2.2(a). The electron gun and channeltron are mounted at fixed positions, defining a fixed angle of 7° at the sample between the incidence beam and the diffracted beam, which is detected by the channeltron. In a SPA-LEED measurement, the reciprocal space is scanned by changing the electrostatic

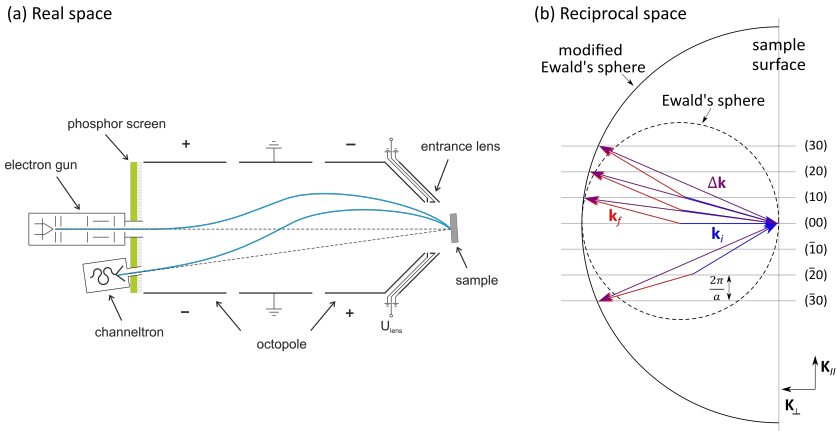


Figure 2.2: (a) Schematic of a SPA-LEED instrument in real space, taken from Ref. [67]. The octopole plates have 3 segments that are individually supplied with designated voltages to control the electrostatic field and direct the electron path in "S-like" trajectories. In a measurement, the angles of the incident and diffracted beams with respect to the sample surface are scanned, whereby the angle between incidence and diffracted beam is kept constant 7° . (b) Modified Ewald's construction for SPA-LEED: The momentum vector of the incidence beam \mathbf{k}_i is shown in blue and that of the diffracted beam \mathbf{k}_f in red. In a SPA-LEED scan, the diffraction vector $\Delta\mathbf{k} = \mathbf{k}_f - \mathbf{k}_i$ (purple) is rotated according to the modified Ewald's sphere, which is about twice as big as in conventional LEED given the same electron energy.

field that controls the electron beams. Note that the electrostatic field has to be passed twice by the electrons (on the incidence and diffracted path), and that influences the electron paths as well as the incidence and exit angles of the electron beams at the sample, but not the angle between the incident and the diffracted beam, which is always 7° . The diffraction condition for a SPA-LEED measurement can be represented by the modified Ewald's construction, which is illustrated in Fig. 2.2(b). With the angle between incidence and diffracted beam kept constant, the scattering vector $\Delta\mathbf{k} = \mathbf{k}_f - \mathbf{k}_i$ is continuously rotated during scanning of the electrostatic field. $\Delta\mathbf{k}$ forms the so-called "modified Ewald's sphere", which is much larger than the (conventional) Ewald's sphere in conventional LEED, see Fig. 2.2(b). All intersection points of the modified Ewald's sphere and the diffraction rods correspond to LEED reflections that can be detected in a SPA-LEED scan.

With the channeltron as a detection device, the method is very sensitive to small electron signals and hence the primary beam intensity and beam intensity can be largely reduced compared to conventional LEED. This is an important advantage for studying sensitive organic adsorbate. The resolution of a LEED, as well as a SPA-LEED, is restricted by the maximum area from which the electrons interfere coherently, which is referred to as *transfer width* of the instrument [68–71]. The transfer width T is observed to be

$$T = \frac{k_{01}}{w} a_0, \quad (2.1)$$

where w is the FWHM of the specular spot, k_{01} is the distance between the first order fundamental spots and the specular spot, a_0 is the lattice parameter of the measured sample [68, 72]. The transfer width of a conventional LEED is about 100 Å [68, 69], while that of a SPA-LEED is about 2000 Å [68]. For this high resolution, the spot profile analysis of diffraction spots can provide information of the domain sizes of the structures on the surface. The beam footprint of the SPA-LEED instrument is several mm², making SPA-LEED insensitive to local defects and providing averaged information on the measured area.

2.1.2 Diffraction image correction

For a precise analysis of conventional LEED as well as SPA-LEED measurements, it is important to correct the diffraction images for systematic distortions. This could be performed using the software LEEDLab and LEEDCal [73] developed by Sojka *et al.* [74].

The image distortion in a conventional LEED measurement is mainly caused by the fact that the fluorescence screen is not spherical, and hence the

spots are seen at too high \mathbf{K}_{\parallel} -values in the outer part of the LEED images, see Fig. 2.1 (a).

In a SPA-LEED diffraction image, the intensity for each \mathbf{K}_{\parallel} -vector is measured at a different angle of incidence at the sample and with a different beam path through the octopole lens. In particular at high \mathbf{K}_{\parallel} -values, the e-beam passes through the electrostatic field relatively far away from the axis of the instrument, and hence in an area where the electrostatic field becomes asymmetrically distorted. Image distortions are the consequence, usually shifting the LEED spots to smaller \mathbf{K}_{\parallel} -values. These distortions are instrument related, and (at identical settings of the instrument) can be measured using a sample with a well-known structure. Such a measurement can be used for calibration, and in turn for correcting the images obtained for unknown samples. Several steps have to be performed in order to obtain a proper image correction:

- 1 Measure the sample under study with optimized parameters for image quality and desired presentation of the diffraction pattern in the image: (i) sample to SPA-LEED position and tilt angle; (ii) offset for (00) spot in \mathbf{k} -space, which is controlled by the voltages set in the red box shown in Fig. 2.3; (iii) image size in \mathbf{k} -space and (iv) in pixels – these two parameters define the image resolution and are set in the blue box shown in Fig. 2.3 –; (v) primary energy of incidence electrons and (vi) lens voltages setting, which are set from the SPA-LEED controller.
- 2 Measure the calibration sample. It is important to use the same parameters to measure a calibration sample. Samples suitable for the calibration measurements are Si(111)-(7 × 7) or PTCDA/Ag(111) since they have a well-known structure with a large unit cell, i.e. rather many visible LEED spots in the relevant \mathbf{k} -space region. In this work, Si(111)-(7 × 7) is used, see Fig. 2.3. Note that if one centered the (00) spot for the surface under study, most likely, using the same measurement parameters (in particular, "X Center" and "Y Center" voltages in the WinSPA software) to do the calibration measurement, one would find the (00) spot of the calibration sample not centered in the diffraction image, as in the case for Fig. 2.3.
- 3 Extract the distortion matrix with the LEEDCal software. It compares the measured Si(111)-(7 × 7) diffraction image with the theoretical lattice. Fig. 2.4 shows a screenshot of the LEEDcal software with a Si(111)-(7 × 7) calibration measurement. First, the radial distortion is extracted by the software. Then, it uses the residuals as a reference point for approximation of the asymmetrical distortion. The radial and asymmet-

ric distortion is described by a distortion matrix that can be applied to future measurements performed with the same parameters [74].

- 4 Apply the distortion matrix to the diffraction image of the sample under study obtained in step 1. Fig. 2.5 shows an example for $G-R0^\circ$ on SiC(0001) before and after applying the distortion correction.

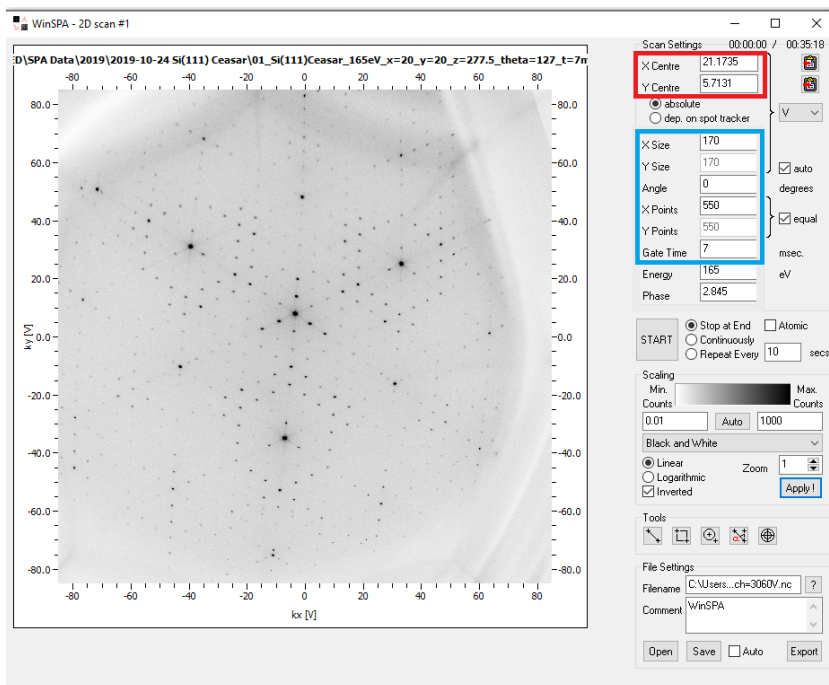


Figure 2.3: Screenshot of the WinSPA software showing the measurement parameters set for a Si(111)-(7 × 7) reconstructed surface. The "X Center" and "Y Center" voltages set in the red box control the position of the diffraction pattern in the image. The parameters in the blue box control the image resolution. "X size" and "Y size" define scan ranges in volts. These voltages control the "S-like" electron paths (in real space) shown in Fig. 2.2(a) and control the scan in reciprocal space. Therefore, the axes can be converted from Volts to $\%BZ$ or \AA^{-1} .

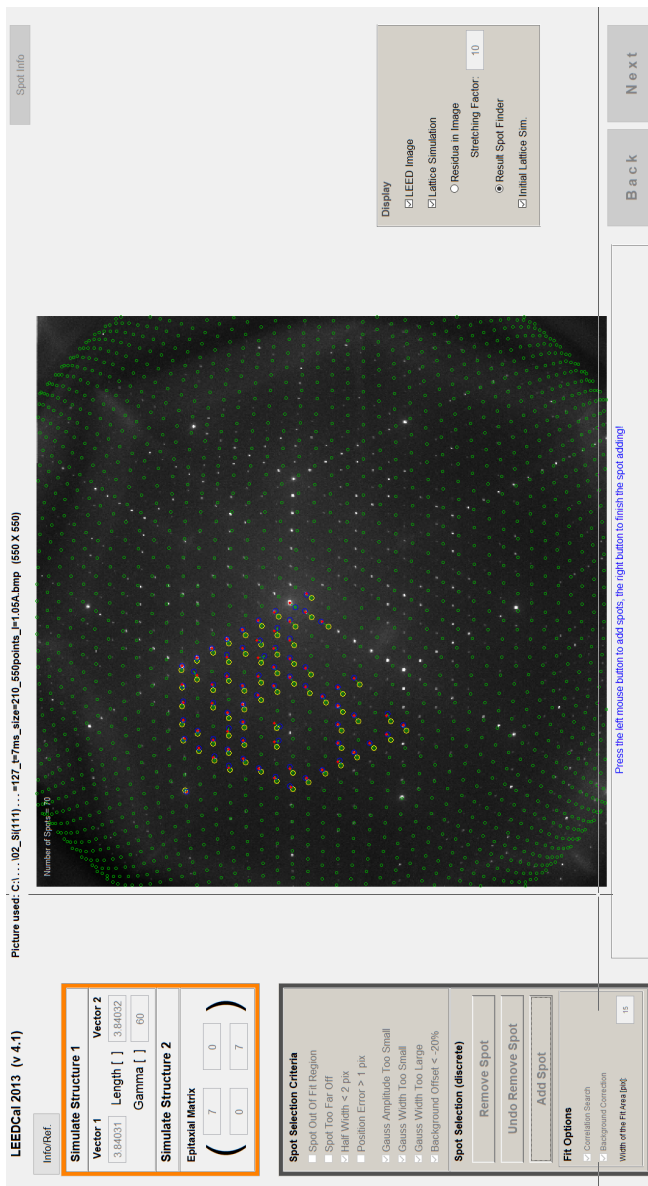


Figure 2.4: Screenshot of the LEEDCal software showing the calibration for a Si(111)-(7 × 7) reconstructed surface. The calibration measurement image obtained from WinSPA (see Fig. 2.3) is inverted (spot intensities in white on dark background) and the theoretical lattice (green circles) is overlaid. LEEDCal then detects neighboring (measured) spot intensities (red dots) and attributes them to the theoretical lattice (yellow circles). The sensitivity and the range of the detection can be tuned in the gray box on the left side. If the automatic spot detection/attribution does not work well enough, manual attribution is also possible.

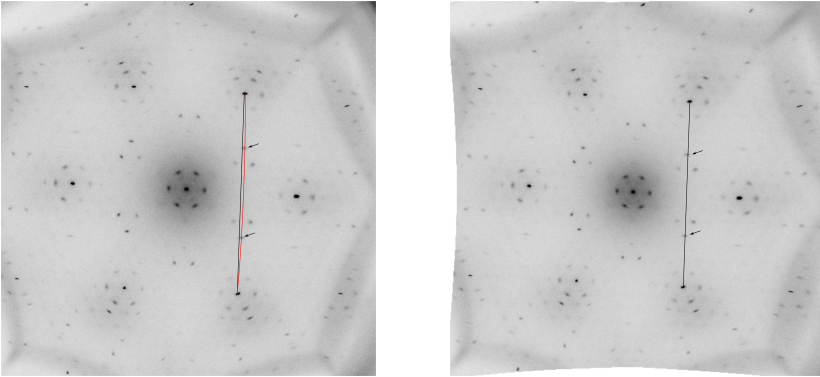


Figure 2.5: Diffraction images of a graphene ($G-R0^\circ$) sample measured at 165 eV by SPA-LEED before (left) and after (right) distortion correction. The black and red lines indicate that the diffraction spots are aligned in the corrected image, but not in the uncorrected. Before correction, the two spots indicated by small arrows are slightly off the black line and rather lie on the red curve.

2.2 Photoelectron spectroscopy

2.2.1 Theoretical description of photoelectron spectroscopy

Photoelectron spectroscopy is widely used in surface science for studying electronic properties. The photoelectric effect describes the absorption of a photon with well-defined energy $h\nu$ in a solid (h is the Planck's constant and ν is the frequency of the photon). The energy $h\nu$ transfers from the photon to an electron and the electron is emitted from the sample with kinetic energy E_{kin} (Fig. 2.6(a)). The system remains in an excited state for a short time and relaxes via Auger electron emission (Fig. 2.6(b)) or fluorescence. In the Auger emission process, an electron from higher energy level relaxes to the hole at lower energy level that was produced by the photo-absorption process. Both photo- and Auger-electrons are detected in photoemission spectroscopy.

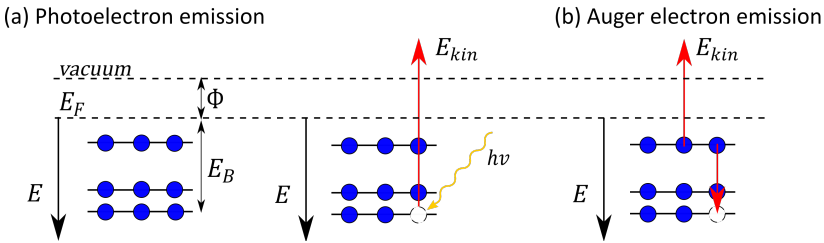


Figure 2.6: Schematic of the photoemission process in the case of metal. (a) Photoemission from the initial state to the excited state. (b) Auger electron emission.

Considering the energy transfer between photon and electron, we can excite one electron in a system of N electrons from its initial state $|\psi_i\rangle$ to an excited state (final state) $|\psi_f\rangle$ with a photon field (namely an electromagnetic field) having the vector potential \mathbf{A} . Assuming that the excitation is sudden and there is no interaction between the escaping photoelectron and the remaining system, the probability $w_{i,f}$ that the initial state transforms to the final state per time unit can be described by Fermi's Golden Rule [75]:

$$w_{i,f} \propto \frac{2\pi}{\hbar} \left| \langle \psi_f | \hat{H}_{int} | \psi_i \rangle \right|^2 \delta(E_f - E_i - h\nu), \quad (2.2)$$

where \hat{H} is the Hamiltonian of interaction between the N electrons and the vector potential of the electromagnetic field \mathbf{A} . E_f and E_i are the energies of the final and initial states of the system. \hbar is the reduced Planck constant. The

δ -function represents the energy conservation in the photo-excitation process. In a general form \hat{H} is:

$$\begin{aligned}\hat{H} &= \frac{(\mathbf{p} + e\mathbf{A})^2}{2m_e} - eU \\ &= \frac{1}{2m_e}(\mathbf{p}^2 + e\mathbf{A}^2 + e\mathbf{p} \cdot \mathbf{A} + e\mathbf{A} \cdot \mathbf{p}) - eU,\end{aligned}\quad (2.3)$$

where U is the vector and scalar potential and \mathbf{p} the momentum operator $\mathbf{p} = i\hbar\nabla$. e is the electron charge, m_e the electron mass, and $\mathbf{A} \cdot \mathbf{p} + \mathbf{p} \cdot \mathbf{A} = 2\mathbf{A} \cdot \mathbf{p} + i\hbar(\nabla \cdot \mathbf{A})$. With $U = 0$, neglecting of the "two-photon process" term $\mathbf{A} \cdot \mathbf{A}$, and assuming that $\nabla \cdot \mathbf{A} = 0$ because of transitional invariance in solids, one obtains

$$\hat{H} = \frac{\mathbf{p}^2}{2m_e} + \frac{e\mathbf{A} \cdot \mathbf{p}}{m_e}.\quad (2.4)$$

According to $\hat{H} = \frac{\mathbf{p}^2}{2m_e} + \hat{H}_{int}$, the interaction Hamiltonian \hat{H}_{int} is therefore

$$\hat{H}_{int} = \frac{e}{m_e} \mathbf{A} \cdot \mathbf{p}.\quad (2.5)$$

Typical photon energies are $h\nu = 10$ to 1000 eV, corresponding to $\lambda = 10^3$ to 10 Å, i.e. rather large wavelength compared to atomic distances. Therefore, \mathbf{A} can be assumed to be constant at atomic scale ($\mathbf{A} = const$). Considering a system with N electrons, the wave function of the system ψ_i^N can be written as a product of the electron orbital k from which one electron is excited and the wave function of the remaining electrons ψ_i^{N-1} , such as

$$\psi_i^N = C\phi_i^k\psi_i^{N-1},\quad (2.6)$$

where C is the operator for breaking the symmetry of the wave function. The final state of the wave function can be written in a similar way:

$$\psi_f^N = C\phi_f^k\psi_f^{N-1}.\quad (2.7)$$

Hence, the matrix element in eq. 2.2 becomes

$$\langle\psi_f|\hat{H}_{int}|\psi_i\rangle \propto \langle\phi_f^k|\hat{H}_{int}|\phi_i^k\rangle \langle\psi_f^{N-1}|\psi_i^{N-1}\rangle.\quad (2.8)$$

The matrix element is thus a product of a one-electron Hamiltonian and an $(N-1)$ -electron overlap integral. With the assumption that orbitals that are not involved in the process do not change (frozen-orbital approximation), we write $\psi_f^{N-1} = \psi_i^{N-1}$, and $\langle\psi_f^{N-1}|\psi_i^{N-1}\rangle = \delta_{i,f} = \delta(E_f^N - E_i^N - h\nu)$. Hence, the Hamiltonian becomes just the one-electron Hamiltonian. Therefore, the probability of the photoemission process can be written as

$$w_{i,f} \propto |\langle\phi_f^k|\mathbf{A} \cdot \mathbf{p}|\phi_i^k\rangle|^2 \delta(E_f^N - E_i^N - h\nu).\quad (2.9)$$

In a photoemission experiment, we can measure the kinetic energy of the excited electron E_{kin} (see Section 2.2.2). We know that the photon energy $h\nu$ excites the system from its equilibrium state (E_i^N) to an excited state (E_f^{N-1}) and releases one electron (with E_{kin}) from the system, thus

$$E_{kin} = h\nu - (E_f^{N-1} - E_i^N) = h\nu - (E_B + \Phi), \quad (2.10)$$

where E_B is the binding energy of the electron (i.e. the energy necessary to lift the electron to the Fermi level E_F) and Φ the work function in the case of metal (see Fig. 2.6). The binding energy E_B is unique for each of the core shells of each element. It also shifts, when the emitting atom is bound to other atoms. Therefore, probing the core-level binding energy also gives information about the chemical environment of the species. The photon energy used for measuring the core-level is 100 to 5000 eV, which is in the (soft) x-ray range. Thus, this measurement is known as x-ray photoelectron spectroscopy (XPS). With lower photon energy in a range of 20 to 100 eV, mostly the valence electron will be excited. In all cases, the electron mean free path is short and provides the surface sensitivity of this method [76].

2.2.2 The photoemission spectroscopy experiment

Angular resolved photoemission spectroscopy (ARPES) allows us to determine the electronic band structure of a system in reciprocal space when not only the energy but also the momentum of the excited electron is measured. By scanning polar (θ) and azimuthal (ϕ) angles, the electron intensity in \mathbf{k} -space can be mapped. Modern electron analyzers are equipped with a two-dimensional photo-detector (channel plate), which is able to record energy and momentum-resolved data, see Fig. 2.7.

The setup for the ARPES measurements performed in this thesis is shown in Fig. 2.8. It consists of three chambers: the main chamber with a Scienta R4000 hemispherical analyzer and a monochromatic UV source (Scienta VUV 5K), a LEED chamber with an Omicron LEED and a preparation chamber. Samples can be introduced via a load lock. For the samples measured in this work, direct current heating and electron bombardment heating is used for sample annealing. The preparation chamber is equipped with gas inlet for borazine. The temperature of the sample is measured with a pyrometer during preparation. After preparation, the sample can be transferred to the LEED chamber to determine its geometric structure. The transfer system is compatible with the I09 beamline at Diamond Light Source (see Sec. 2.3).

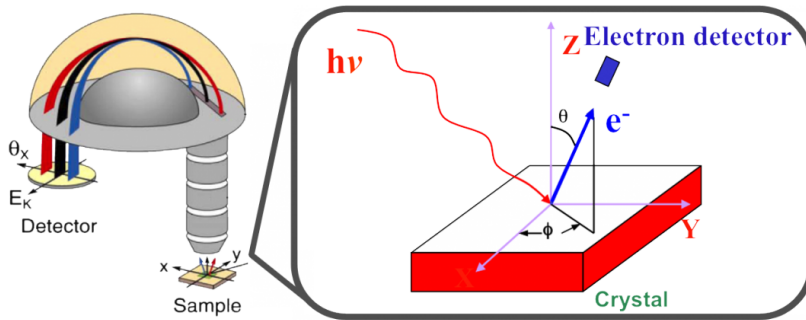


Figure 2.7: Schematic of the ARPES measurement. The left side illustrates the spherical analyzer which is equipped with a two-dimensional detector offering electron detection with both energy and angular resolution. The right side shows the schematic of the measurement geometry at the surface. θ is the angle between the analyzer and the surface normal. ϕ is the surface in-plane rotational angle. By rotating the sample, one can define the two parameters for measurement. This figure is adapted from Ref. [77, 78].

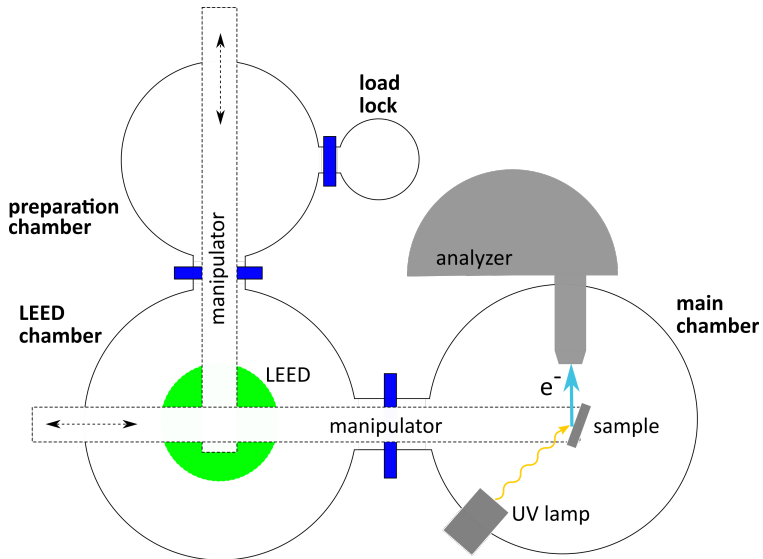


Figure 2.8: Schematic of the ESCA chamber for sample preparation and ARPES measurements. Gate valves to separate the chambers are indicated in blue. Two manipulators are indicated as dashed rectangles. LEED is indicated as a green circle.

2.3 The normal incidence x-ray standing wave technique

Utilizing the chemical sensitivity of XPS, x-ray standing wave technique probes the vertical structure of the adlayers on a crystal with good resolution better than 0.05 Å. The basic principle of the normal incidence x-ray standing wave (NIXSW) technique is as follows: When illuminating a crystal with x-rays under a selected Bragg condition, the incoming and diffracted beam interfere at the proximity of the crystal and form an x-ray standing wave (XSW) field (see Fig. 2.9). The periodicity of the XSW field is equal to the Bragg plane spacing d_{hkl} , and hence defined by the chosen bulk reflection ($h k l$). Therefore, within and above the crystal, there are nodal plane maxima and minima of XSW intensity. The phase Φ of the XSW field, which is the relative position (in vertical direction to the Bragg planes) of the maxima of the XSW to the Bragg planes, can be tuned by changing the photon energy of the incoming beam. By tuning Φ , i.e. varying the photon energy in a range of several eV, the photon absorption of the atoms is varied in an NIXSW scan. The range of this scan covers only an energy range that is slightly larger than the Darwin profile of the Bragg reflection. Φ shifts from π to 0 when scanning through the Bragg condition. Since the amount of photoelectrons excited from the same atom is dependent of the XSW phase, by measuring the emitted photoelectron yield around the Bragg energy, one can extract the vertical distance of the atomic species relative to the Bragg planes. More details will be discussed in the following. Only the basics of the technique will be presented here, while detailed description can be found in Ref. [79] and Ref. [80].

2.3.1 Photoelectron emission process in NIXSW

In this section, we aim for quantifying the photoemission process taking place in an NIXSW experiment. For this, we first calculate the x-ray intensity of the XSW and use this as the primary intensity for the photoemission process resulting in the photoelectron yield Y of a certain atomic species that is emitted in the NIXSW experiment. An incoming wave field of x-rays is diffracted backward as shown in Fig. 2.10:

$$\mathbf{E}_0 = \mathbf{e}_0 E_0 e^{2\pi i(\nu_0 t - \mathbf{K}_0 \cdot \mathbf{r})} \quad (2.11)$$

$$\mathbf{E}_H = \mathbf{e}_H E_H e^{2\pi i(\nu_H t - \mathbf{K}_H \cdot \mathbf{r})}, \quad (2.12)$$

where \mathbf{e}_0 , \mathbf{e}_H are polarization vectors, \mathbf{r} is a real space vector and the wave propagation vectors \mathbf{K}_0 and \mathbf{K}_H are with length $|\mathbf{K}_0| = |\mathbf{K}_H| = K = \lambda^{-1}$, where λ is the x-ray wavelength. Since we consider elastic scattering, $\nu_0 =$

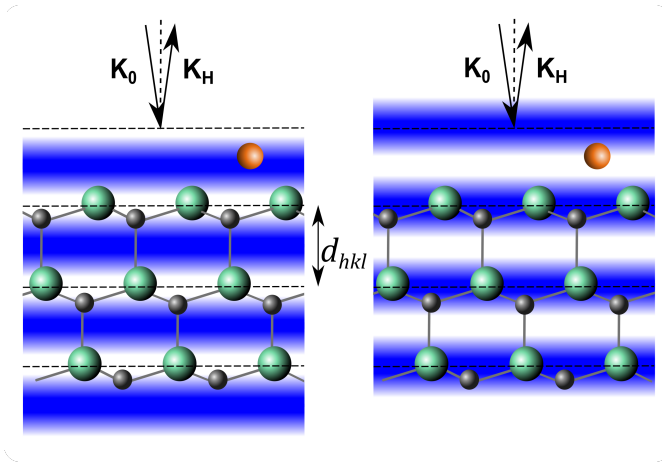


Figure 2.9: Schematic of the crystal surface illuminated by x-ray under Bragg condition with maxima of the XSW in blue. The bulk crystal represented by gray and green spheres has an adatom (orange) on the surface. The Bragg planes are indicated as black dashed lines with the interplanar spacing d_{hkl} . By scanning the photon energy of the incoming beam through the Bragg condition, the phase Φ of the XSW field shifts by π (left to right side of the schematic). Hence, the amount of excited photoelectrons, i.e. the photoelectron yield, varies with the photon energy. The NIXSW technique probes the relative vertical distances of atomic species to Bragg planes.

$\nu_H = \nu$. One important aspect to utilize the XSW field is that the phase Φ of the term $\mathbf{E}_H/\mathbf{E}_0$ varies as one scans through the Bragg condition. Thus, the wave field of the reflected beam is related to the incoming beam as

$$E_H = \sqrt{R}E_0e^{i\Phi}, \quad (2.13)$$

with the amplitude \sqrt{R} and phase Φ . The reflectivity of the x-ray is

$$R = \frac{|E_H|^2}{|E_0|^2}, \quad (2.14)$$

where R and Φ vary across the scanned photon energy range. The total wave field is

$$\begin{aligned} \mathbf{E} &= \mathbf{E}_0 + \mathbf{E}_H = \mathbf{e}_0E_0e^{2\pi i(\nu t - \mathbf{K}_0 \cdot \mathbf{r})} + \mathbf{e}_H E_H e^{2\pi i(\nu t - \mathbf{K}_H \cdot \mathbf{r})} \\ &= E_0 e^{2\pi i \nu t} \left[\mathbf{e}_0 e^{-2\pi i \mathbf{K}_0 \cdot \mathbf{r}} + \mathbf{e}_H \sqrt{R} e^{i\Phi - 2\pi i \mathbf{K}_H \cdot \mathbf{r}} \right] \\ &= E_0 e^{2\pi i(\nu t - \mathbf{K}_0 \cdot \mathbf{r})} \left[\mathbf{e}_0 + \mathbf{e}_H \sqrt{R} e^{i\Phi - 2\pi i \mathbf{H} \cdot \mathbf{r}} \right]. \end{aligned} \quad (2.15)$$

In the last line the diffraction condition $\mathbf{H} = \mathbf{K}_\mathbf{H} - \mathbf{K}_\mathbf{0}$ was used. Hence, the normalized x-ray intensity at a certain position \mathbf{r} is

$$I_{\text{XSW}}(\xi) = \frac{|\mathbf{E}_\mathbf{0} + \mathbf{E}_\mathbf{H}|^2}{|\mathbf{E}_\mathbf{0}|^2} = 1 + R + P_{\text{x-ray}}(\xi)2\sqrt{R}\cos(\Phi - 2\pi\mathbf{H} \cdot \mathbf{r}), \quad (2.16)$$

where $P_{\text{x-ray}}(\xi)$ is the polarization factor. For σ -polarized x-ray, $\mathbf{e}_{0\sigma} = \mathbf{e}_{\mathbf{H}\sigma}$ are both perpendicular to the plane of incidence defined by $\mathbf{K}_\mathbf{0}$ and $\mathbf{K}_\mathbf{H}$. While for π -polarized beam, $\mathbf{e}_{0\pi}$ and $\mathbf{e}_{\mathbf{H}\pi}$ lie in the plane of incidence and are not parallel (see Fig. 2.10). This leads to

$$P_{\text{x-ray}}(\xi)\mathbf{e}_\mathbf{0} \cdot \mathbf{e}_\mathbf{H} = \begin{cases} \cos 2\theta = -\cos 2\xi & \text{for } \pi\text{-polarization} \\ 1 & \text{for } \sigma\text{-polarization} \end{cases} \quad (2.17)$$

where θ is the Bragg angle, and $\xi = 180^\circ - \theta$, see Fig. 2.10.

It is useful to decompose the real space vector \mathbf{r} , pointing to an absorbing core-electron in the crystal into the position of the electron in the crystal \mathbf{r}_a and the position of the electron in an atom \mathbf{r}_e : $\mathbf{r} = \mathbf{r}_a + \mathbf{r}_e$. The electrostatic field \mathbf{E} can therefore be written as:

$$\mathbf{E} = E_0 e^{2\pi i(\nu t - \mathbf{K}_\mathbf{0} \cdot \mathbf{r}_a - \mathbf{K}_\mathbf{0} \cdot \mathbf{r}_e)} \left[\mathbf{e}_\mathbf{0} + \mathbf{e}_\mathbf{H} \sqrt{R} e^{i\Phi} e^{-2\pi i\mathbf{H} \cdot \mathbf{r}_a} e^{-2\pi i\mathbf{H} \cdot \mathbf{r}_e} \right]. \quad (2.18)$$

The photoelectron yield is proportional to the square modulus of the matrix element M_{fi} given by Eq. 2.5

$$\begin{aligned} M_{fi} &\equiv \langle \psi_f | \hat{H}_{\text{int}} | \psi_i \rangle = \langle \psi_f | \frac{e}{m_e} \mathbf{A} \cdot \mathbf{p} | \psi_i \rangle = \langle \psi_f | \mathbf{E} \cdot \mathbf{p} | \psi_i \rangle \\ &= \frac{e}{m_e} E_0 e^{-2\pi i(\nu t - \mathbf{K}_\mathbf{0} \cdot \mathbf{r}_a)} \left[M_\mathbf{0} + \sqrt{R} e^{i\Phi - 2\pi i\mathbf{H} \cdot \mathbf{r}_a} M_\mathbf{H} \right], \end{aligned} \quad (2.19)$$

where $\mathbf{s}_\mathbf{0} = \mathbf{K}_\mathbf{0}/|\mathbf{K}_\mathbf{0}|$, $\mathbf{s}_\mathbf{H} = \mathbf{K}_\mathbf{H}/|\mathbf{K}_\mathbf{H}|$, and

$$\begin{aligned} M_\mathbf{0} &= \langle \psi_f | e^{-2\pi i\mathbf{K}_\mathbf{0} \cdot \mathbf{r}_e} (\mathbf{e}_\mathbf{0} \cdot \mathbf{p}) | \psi_i \rangle \\ M_\mathbf{H} &= \langle \psi_f | e^{-2\pi i\mathbf{K}_\mathbf{H} \cdot \mathbf{r}_e} (\mathbf{e}_\mathbf{H} \cdot \mathbf{p}) | \psi_i \rangle. \end{aligned} \quad (2.20)$$

The emitted photoelectron intensity is proportional to the matrix element squared:

$$I = |M_{fi}|^2 = |E_0|^2 \left\{ S_{\mathbf{00}} + S_{\mathbf{HH}}R + 2\sqrt{R}\text{Re} [S_{\mathbf{0H}}e^{i(\Phi + \mathbf{H} \cdot \mathbf{r}_a)}] \right\}, \quad (2.21)$$

with $S_{\mathbf{00}} = |M_\mathbf{0}|^2$, $S_{\mathbf{HH}} = |M_\mathbf{H}|^2$, $S_{\mathbf{0H}} = M_\mathbf{0}^* M_\mathbf{H}$. Finally, the photoelectron yield can then be written as

$$Y = \frac{I}{I_0} = 1 + S_R R + 2|S_I| \sqrt{R} F_c^{\mathbf{H}} \cos(\Phi - 2\pi P_c^{\mathbf{H}} + \Psi), \quad (2.22)$$

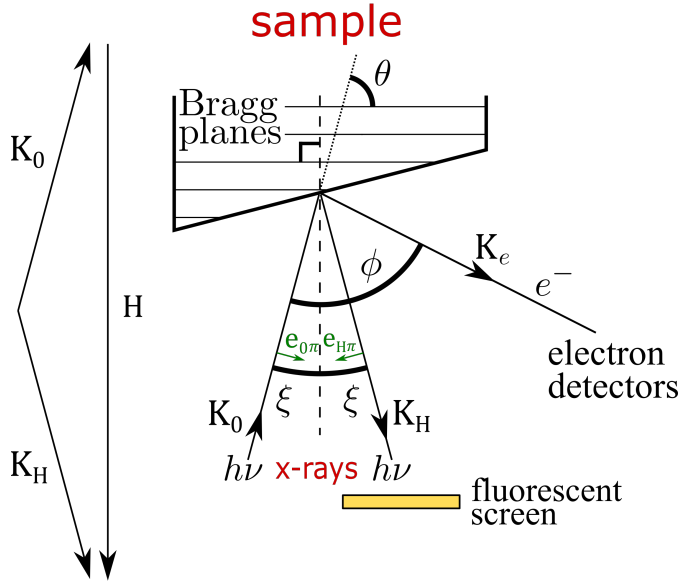


Figure 2.10: Geometry of the NIXSW measurement. \mathbf{K}_0 , \mathbf{K}_H are wave propagation vectors with polarization vectors $\mathbf{e}_{0\pi}$ and $\mathbf{e}_{H\pi}$ lying in the plane of incidence. For σ -polarization, both $\mathbf{e}_{0\sigma}$ and $\mathbf{e}_{H\sigma}$ are oriented perpendicular to the scattering plane (not shown). The diffraction condition is $\mathbf{H} = \mathbf{K}_H - \mathbf{K}_0$. The intensity of the reflected x-ray beam (reflectivity R) is measured by monitoring the intensity on a fluorescent screen. The schematic is adapted from Ref. [82].

where $S_R = S_{\mathbf{H}\mathbf{H}}/S_{\mathbf{0}\mathbf{0}}$, $S_I = |S_I|e^{i\psi} = S_{\mathbf{0}\mathbf{H}}/S_{\mathbf{0}\mathbf{0}}$ include a correction for non-dipolar effects. These parameters depend on geometric parameters (ϕ and ξ), and on γ , a complex number quantifying the d -wave contribution to the photoemission intensity and the phase difference between p - and d -emitted waves. $\xi = 3.5^\circ$ is usually held constant. By analyzing the electron yield ϕ -angle resolved, one can gain information about the non-dipole effect [80,81].

The coherent position $P_c^{\mathbf{H}}$ and coherent fraction $F_c^{\mathbf{H}}$ in Eq. 2.22 are the fitting parameters that are obtained in the data analysis. They allow a direct, model-free determination of the vertical position of the atomic species considered. $P_c^{\mathbf{H}}$ and $F_c^{\mathbf{H}}$, spanning both from 0 to 1, characterize the spatial distribution of the probed atomic species in the direction \mathbf{H} . $P_c^{\mathbf{H}}$ allows the determination of the average height, or vertical distance, modulo d_{hkl} , of the

species to the next lattice plane below. $F_c^{\mathbf{H}}$ is a measure of the vertical order. For $F_c^{\mathbf{H}} = 1$, all atoms of the probed atomic species are well-ordered at the same height that can be calculated from $P_c^{\mathbf{H}}$. For $F_c^{\mathbf{H}} = 0$, there is no periodic order for the species within d_{hkl} . Note that also special cases of multi-site occupation within d_{hkl} can cause very low $F_c^{\mathbf{H}}$ (see chapter 6).

An NIXSW experiment is performed as follows: While scanning the photon energy through the Bragg condition, for each photon energy step the reflected x-ray intensity and a photoelectron spectrum of the region of interest are recorded. The former yields the x-ray reflectivity as a function of the photon energy. The latter (photoelectron spectra) is analyzed in detail, e.g. by background subtraction and peak fitting, so that the integrated photoelectron intensity of the selected core-levels can be extracted. This is done for all the spectra recorded at each photon energy step, and results in the photoelectron yield Y , also plotted versus the photon energy. This yield curve is finally fitted by Eq. 2.22, resulting in values for $P_c^{\mathbf{H}}$ and $F_c^{\mathbf{H}}$.

With

$$z = (n + P_c^{\mathbf{H}})d_{hkl}, \quad (2.23)$$

where n is an integer and d_{hkl} the vertical spacing between two adjacent Bragg planes, one can obtain the relative height z of the probed atomic species X . The coherent position and fraction can be visualized as a vector

$$D^X = F_c^{\mathbf{H},X} e^{2\pi i P_c^{\mathbf{H},X}} \quad (2.24)$$

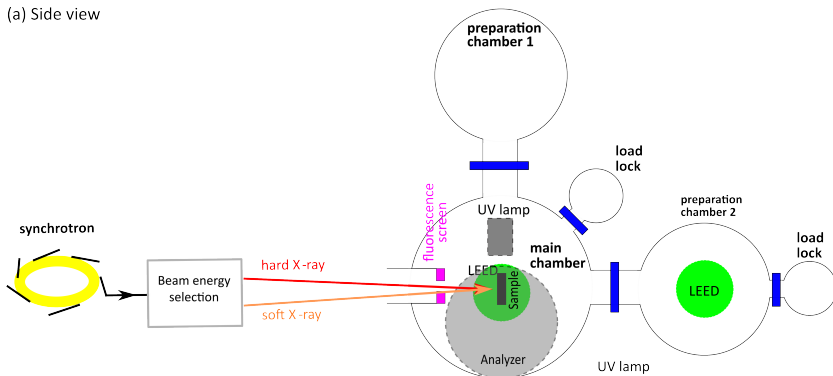
in a polar diagram, where the $P_c^{\mathbf{H}}$ is the polar angle, $F_c^{\mathbf{H}}$ is the length of the vector. For an example see Fig. 3.9 in chapter 3.

2.3.2 Experimental setup at I09 beamline at the DLS

The I09 beamline at Diamond Light Source (DLS), Didcot, UK, is a dedicated beamline for NIXSW experiments based on photoemission. Samples can be introduced through load locks of preparation chambers 1 and 2 as shown in Fig. 2.11. Facilities for sputtering, annealing, and layer deposition are available in both preparation chambers. The six-axis main manipulator (not shown) can transfer samples from preparation chamber 1 into the main chamber for measurements. The main chamber is equipped with a VG Scienta EW4000 hemispherical electron analyzer with an acceptance angle of 56° . The thoughtfully-designed and well-aligned beamline allows both soft and hard x-ray to be focused on the same spot on the sample, which is of great advantage for surface characterization since high-resolution XPS and UPS measurements are possible on the same sample position that is used for NIXSW. An MCP-LEED (Omicron) and a UV-lamp (Scienta VUV 4K) are also available in the

main chamber. When x-rays illuminate the sample, the reflected beam intensity can be measured on the fluorescence screen.

(a) Side view



(b) Top view

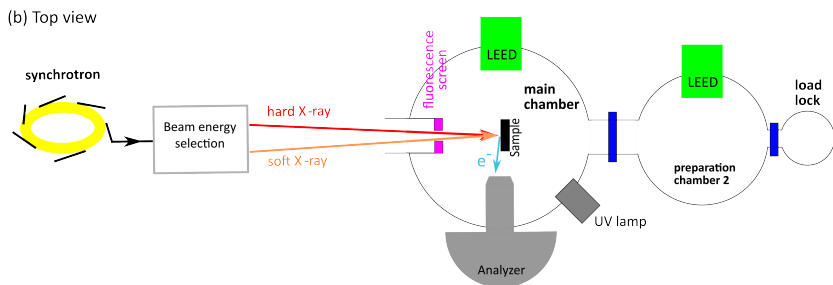


Figure 2.11: Simplified (a) side-view and (b) top-view schematics of the I09 beamline at Diamond Light Source, Didcot, UK. Most parts equipped are labeled. Preparation chamber 1 is not shown in the top-view. The manipulators are not illustrated. Gate valves to separate the chambers are indicated in blue, LEED in green.

Chapter 3

Epitaxial boron nitride on 6H-SiC(0001)

The two-dimensional (2D) material, graphene, as one of the next-generation materials for nanoelectronics, has attracted the highest attention since Novoselov and Geim demonstrated its phenomenal electronic properties [7,83]. It turned out that – among many other variables that can be used to engineer its electronic properties – the twist angle between the individual sheets in bilayer graphene stacks emerges as a highly interesting parameter [84,85]. Not only does the twisted bilayer graphene (tBLG) system show superconductivity at the magic angle of 1.1° [20,21,23,24], it also exhibits topological corner charges at 30° twist angle, potentially making the 30° -tBLG system a higher-order topological insulator [22]. So far, in most cases, the twist angle of bilayer graphene has been realized by stacking two micro-mechanically exfoliated graphene flakes under atmospheric or glove-box conditions [86], however, this method is neither scalable nor well reproducible. For any type of large-scale production, strategies involving epitaxial growth of graphene are highly desirable to circumvent these two disadvantages.

Another 2D-material, hexagonal boron nitride (hBN), can be exfoliated down to single atomic layers [87] and is stable at ambient conditions. Because of its large electronic band gap, it is used as insulating material in heterostacks of 2D-layers [2,4], as the substrate for isolating graphene layers [88] and for encapsulating other 2D-material layers [89,90]. Such potential applications reinforced the interest in growing hBN epitaxially. While this is frequently studied on metallic substrates (Refs. [91–93] and references therein), only a few studies have been performed on semiconducting substrates [94,95].

Usually the precursor molecule borazine ($B_3H_6N_3$) is used for epitaxial growth of hBN. In this chapter, borazine-mediated growth was carried out by annealing a SiC(0001) surface at a temperature in a range of 1100°C to 1250°C

in a borazine atmosphere. At lower preparation temperatures, the boron nitride structure is more dominant, which transitions into a low-quality 0° -rotated graphene (lqG- $R0^\circ$) structure with higher preparation temperatures. The vertical and lateral structure of both the boron nitride structure and the lqG- $R0^\circ$ was determined using the NIXSW technique SPA-LEED. Additional ARPES experiments revealed that the boron nitride structure does *not* exhibit the electronic bands expected for hBN, indicating that the boron nitride overlayer is *not* a decoupled 2D-hBN layer. The boron nitride overlayer is also found *not* robust in air. Therefore, this overlayer is addressed as a 0° -rotated boron nitride (B_xN_y - $R0^\circ$) layer in the following. Note that the B_xN_y - $R0^\circ$ and lqG- $R0^\circ$ layers are both found on a boron bufferlayer (or zeroth-layer, ZL) at the interface to SiC.

In the experiments presented in this chapter, it turns out that the preparation temperature is a crucial parameter for the structure formation of the B_xN_y - $R0^\circ$ and graphene layers. This temperature aspect was noticed, and hence a procedure to apply a certain temperature gradient along one lateral direction on the surface during B_xN_y - $R0^\circ$ growth was developed. These gradient samples allow one to study the effect of the preparation temperature in detail, as demonstrated by the XPS and MCP-LEED experiments shown in Sec. 3.3.

On selected samples, which were prepared with homogeneous preparation temperatures, I investigated the lateral structure in more detail using SPA-LEED (Sec. 3.4) and the vertical structure based on NIXSW data (Sec. 2.3). The comprehensive analysis based on these complementary techniques allows me to understand the transition from B_xN_y - $R0^\circ$ to lqG- $R0^\circ$ taking place in the temperature range from 1150°C to 1250°C .

Please note that this project has been started by Markus Franke, Shayan Parhizkar, and Nafiseh Samiseresht. Samples mentioned in this chapter are prepared by Markus Franke, Dr. François C. Bocquet, and me. The SPA-LEED measurements and most of the ARPES measurements were carried out by me. The NIXSW measurements were carried out by a team of experimentalists during several beamtimes at beamline I09, Diamond, Didcot, UK. The content of this chapter is published with additional DFT calculation as an article, see Ref. [96].

3.1 Sample preparation

Samples were cut from a nitrogen-doped 6H-SiC(0001) wafer purchased from TankeBlue Semiconductor Co. Ltd. The surfaces were cleaned by direct current annealing for 30 minutes at 1150°C in UHV conditions (pressure better than 1×10^{-9} mbar), while applying a Si flux towards the surface in order

to compensate sublimation of Si from the surface at this stage [37]. The Si flux was produced by a heated Si wafer positioned ≈ 10 cm above the sample surface.

During sample preparation, the SiC wafer piece was annealed for another 30 minutes at 880°C, also under Si flux, in order to obtain the Si-rich (3×3) reconstruction [37, 98], which was confirmed using MCP-LEED. At a temperature below 880°C, the Si flux was stopped and a borazine partial pressure of 1.5×10^{-6} mbar was applied. The sample temperature was then quickly increased to the desired value (between 1100°C and 1250°C) within less than five minutes. At this temperature, the sample was annealed for 30 minutes. Note that the SiC samples were mounted in a dedicated way enabling either a very homogeneous temperature distribution across the sample, or a temperature gradient along the direction of direct heating current (see Sec. 3.3). Afterward, the sample was cooled down within 10 minutes and transferred under UHV to the dedicated apparatus for the experiments. Borazine was purchased from Katchem, Praha, Czech Republic.

3.2 Electronic structure and air stability

ARPES measurements were performed in order to identify the 2D structures forming on the SiC surface at different temperatures. Fig. 3.1 shows energy distribution maps around the $\bar{\Gamma}$, \bar{K} and \bar{M} points of the clean SiC(0001) surface (upper part) and of $B_xN_y-R0^\circ$ on SiC, prepared at 1150°C in borazine atmosphere (lower part). The data is recorded using He II radiation ($h\nu = 40.8$ eV), since the band structures are best visible at this photon energy.

The $B_xN_y-R0^\circ$ maps exhibit some broad and faint bands, but no indications of the typical band structure of decoupled 2D-hBN [92, 99]. This finding is in contradiction with Ref. [95], but was confirmed by repeating the experiment using He I UV light and soft x-ray synchrotron radiation ($h\nu = 21$ eV and $h\nu = 110$ eV, respectively, data not shown), with the same result.

The same conclusion – the $B_xN_y-R0^\circ$ layer is *not* a decoupled 2D-hBN layer – can be drawn from diffraction experiments performed on samples which were transferred in air: Fig. 3.2 shows a comparison of LEED patterns recorded from one sample directly after preparation of $B_xN_y-R0^\circ$ and after 48 hours exposure to air. Even with mild annealing in UHV, the original pattern cannot be recovered. hBN, however, is known to be stable in air [92, 100, 101]. In contrast, for samples prepared using the same procedure but higher temperatures (1225°C), a weak and broad Dirac cone was found in the energy dispersion map, as displayed in Fig. 3.3. This confirms that low-quality graphene (lqG- $R0^\circ$) forms from the $B_xN_y-R0^\circ$ structure.

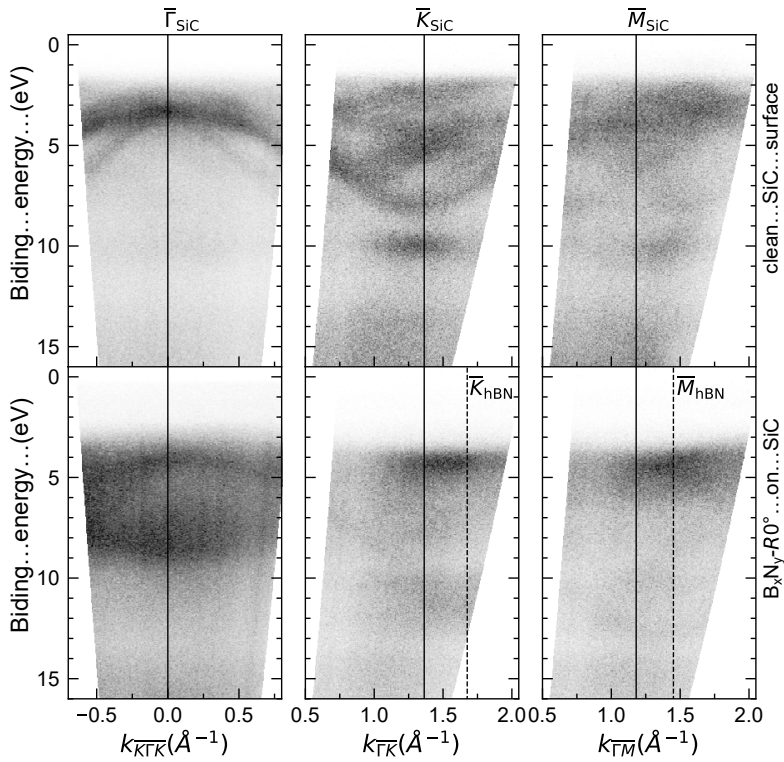


Figure 3.1: Valence band photoemission energy distribution maps of the clean (3×3) reconstructed SiC surface (upper) and a B_xN_y - $R0^\circ$ layer prepared at 1150°C (lower). $h\nu = 40.8$ eV (He II).

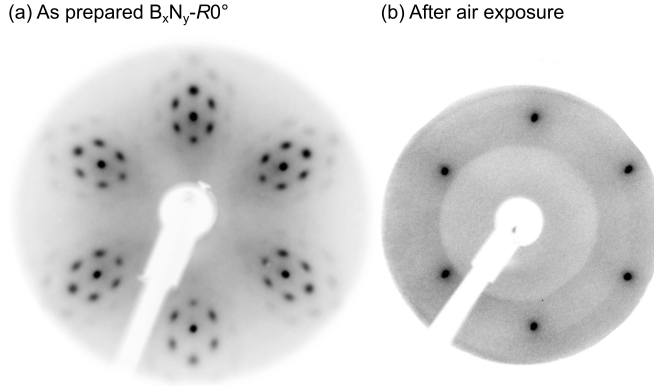


Figure 3.2: Diffraction patterns of a B_xN_y - $R0^\circ$ sample (a) before ($E = 100$ eV) and (b) after exposure to air for 48 hours ($E = 110$ eV). After exposure, all LEED spots have vanished, except those of the substrate.

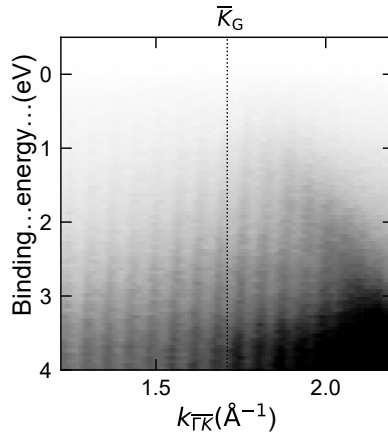


Figure 3.3: Band map of lqG - $R0^\circ$ prepared at 1225°C . $h\nu = 110$ eV.

3.3 Growth temperature dependency

In Fig. 3.4, core-level spectra are shown, obtained using both hard and soft x-rays. The data is recorded at different positions on the temperature gradient sample, correlated to preparation temperatures between 1100°C and 1250°C, as color-coded from blue to red. Three B 1s and two C 1s components were identified. The fact that hard and soft x-rays have different probing depths allows one to find out where the individual components stem from. For C 1s, the situation is very clear, see Fig. 3.4(a-b): The peak at ≈ 284.8 eV is a bulk species (C_{SiC}) since it is stronger at higher photon energy and almost independent from preparation temperature. The other peak at ≈ 286.0 eV is a surface component, very dominant at the smaller photon energy, and only present for higher preparation temperatures. It hence stems from the graphene layer (C_G). For B 1s, it is more difficult to identify the components. Fig. 3.4(f) reveals a bulk-like behavior for the peak at ≈ 190.8 eV (B_{SiC}). Fig. 3.4(d) and (e) also show that this peak is present at all preparation temperatures. Hence, some of the boron atoms must have diffused into the bulk, an effect that has already been reported earlier [102]. The other two components at ≈ 192.6 eV and ≈ 191.8 eV turn out to be located closer to the surface and stem from the B_xN_y - $R0^\circ$ layer ($B_{B_xN_y}$) and the boron bufferlayer underneath (boron zeroth-layer, B_{ZL}), respectively, as can be seen in a careful analysis of the temperature behavior.

Fig. 3.4(c) and (d) reveal that the N 1s and $B_{B_xN_y}$ components decrease in their intensities with increasing preparation temperature. This evolution is better quantified in Fig. 3.5(a), showing normalized intensities of the XPS peaks. It indicates that both the $B_{B_xN_y}$ and N 1s components stem from the same boron nitride structure, which vanishes with increasing preparation temperature. At the same time, the C_G component clearly increases, indicating that the graphene layer (lqG- $R0^\circ$) is formed as B_xN_y - $R0^\circ$ disappears.

In Fig. 3.5(b), the absolute areas of the three B 1s components are shown. At a temperature of $\approx 1100^\circ\text{C}$, $B_{B_xN_y}$ is the dominant component, the B_{ZL} component is also clearly visible, while the B_{SiC} component is small. With $B_{B_xN_y}$ disappearing, the other two components increase, most likely just indicating that the B-N bonding in the boron nitride layer is being broken, which causes a core-level shift towards smaller binding energies. This is supported by the fact that both the B_{ZL} and the B_{SiC} curves are running through a maximum, but at the end of the temperature scale (at 1250°C) reach very much the same intensity as in the beginning (at 1100°C). This indicates that the boron atoms from the B_xN_y - $R0^\circ$ layer in the end either evaporate or diffuse deeper into the bulk so that they are not detected anymore.

Hence, the scenario to be deduced from these measurements is straightfor-

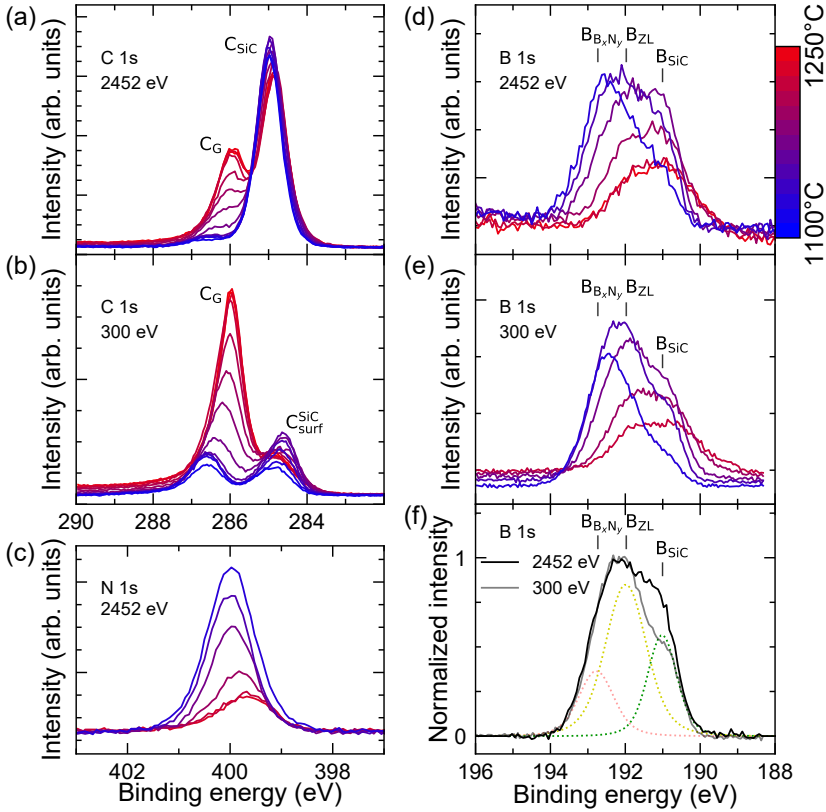


Figure 3.4: (a,b) C 1s, (c) N 1s and (d-f) B 1s core-level spectra measured with hard and soft x-rays on a temperature gradient sample at different positions corresponding to the preparation temperatures color-coded by blue (low T) and red (high T). A comparison of hard (a and d) with soft x-rays (b and e) allows one to identify surface and bulk species, see text. In (f), the comparison is demonstrated for a B 1s spectrum recorded with higher statistics on a B_xN_y - $R0^\circ$ sample. The data are shown after background subtraction, normalization, and calibration of the binding energy scale. All spectra have been measured in a grazing emission geometry.

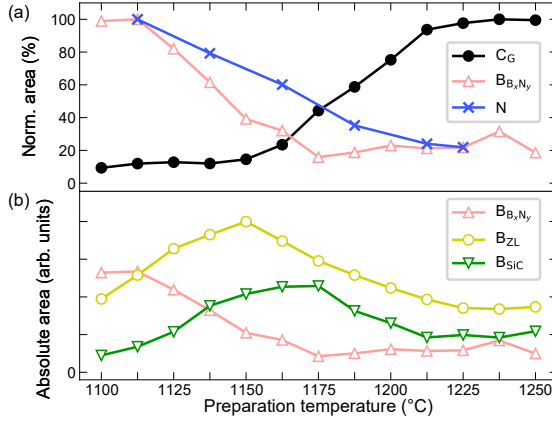


Figure 3.5: Integrated components obtained from the core-level spectra shown in Fig. 3.4(a), (c) and (d) as a function of the preparation temperature. (a) C_G , N , and $B_{B_xN_y}$ intensities normalized to their respective maxima. (b) Absolute intensities of the three B 1s components.

ward: At a transition temperature of $\approx 1150^\circ\text{C}$ the B_xN_y - $R0^\circ$ layer ($B_{B_xN_y}$), which is located above a boron zeroth-layer (B_{ZL}) on the SiC substrate, is gradually replaced by graphene (C_G), while – judging from the core-level spectra – neither the bulk nor the boron zeroth-layer are largely affected.

For the same gradient sample, LEED patterns were recorded and can be correlated to the core-level spectra. Fig. 3.6 shows six diffraction patterns, corresponding to different preparation temperatures. Between 1125°C and 1175°C the LEED patterns are dominated by groups of six reflections in a hexagonal arrangement around each of the SiC $\{10\}$ and $\{01\}$ substrate spots. Their intensity goes through a maximum at 1150°C and decreases afterward so that they are hardly visible anymore at 1200°C . As demonstrated in the following (Sec. 3.4), these spots can be attributed to the B_xN_y - $R0^\circ$ layer. The outermost spots are the B_xN_y - $R0^\circ$ $\{10\}$ and $\{01\}$ spots, all others are explained by multiple diffraction effects. At 1200°C and above the $\{10\}$ and $\{01\}$ spots become very weak and move slightly towards larger k_{\parallel} . This indicates the transition from B_xN_y - $R0^\circ$ to low-quality graphene (lqG - $R0^\circ$), driven by carbon atoms replacing boron and nitrogen [97].

Note the lqG - $R0^\circ$ layer can be obtained by directly ramping the SiC(0001) temperature to 1225°C , as described in Sec. 3.1, as well as by post-annealing the readily prepared B_xN_y - $R0^\circ$ layer in UHV, as discussed Sec. 3.1. However, the much higher quality G - $R0^\circ$ layer that is formed when exposing the SiC

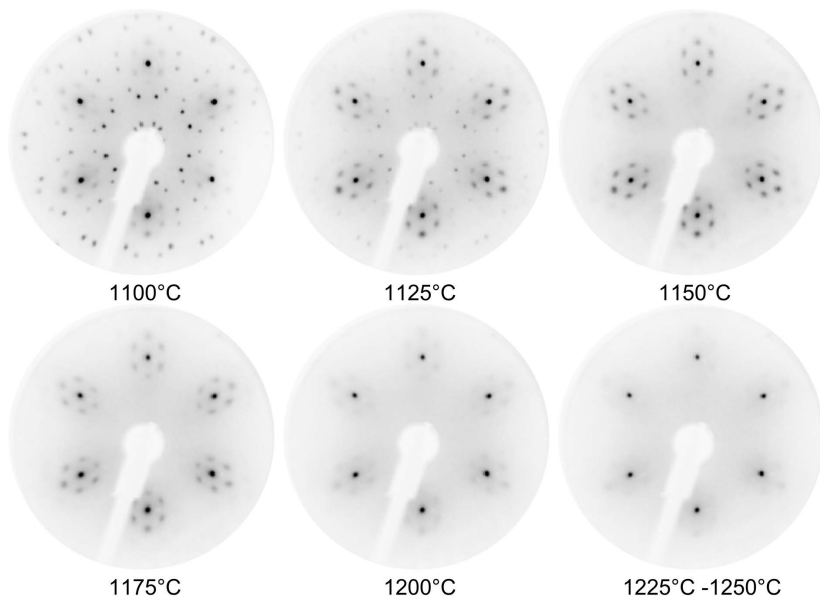


Figure 3.6: Series of LEED images recorded at different positions on the temperature gradient sample, corresponding to preparation temperatures between 1100°C and 1250°C. Electron energy: 100 eV.

sample to borazine at higher temperatures (1330°C, see Fig. 4.1 and the discussion in Sec. 4.1) cannot be obtained by post-annealing of either $B_xN_y-R0^\circ$ or $lqG-R0^\circ$ layers.

Lastly, in the 1100°C pattern, additional spots of a $\begin{pmatrix} 3 & 1 \\ -1 & 2 \end{pmatrix}$ superstructure are visible. They vanish already below 1150°C, i.e., before the N and $B_{B_xN_y}$ XPS peaks disappear, indicating that the underlying reconstruction is lifted even before the $B_xN_y-R0^\circ \rightarrow lqG-R0^\circ$ layer transition process (see below).

3.4 Lateral structure

The data presented so far are recorded from temperature gradient samples, illustrating the effect of the growth temperature on the $B_xN_y-R0^\circ$ and $lqG-R0^\circ$ samples. In the following, results obtained from detailed investigations on homogeneous samples prepared at different temperatures will be presented.

Fig. 3.7(a) displays a SPA-LEED pattern of a sample prepared at 1150°C. The (10) and (01) spots of the SiC substrate spots are marked by red circles,

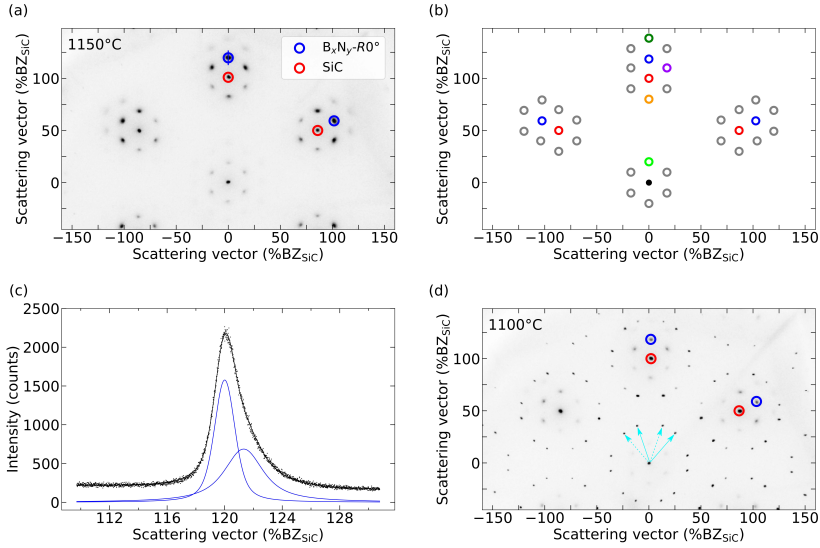


Figure 3.7: (a) Distortion-corrected SPA-LEED pattern of a homogeneous $B_xN_y-R0^\circ$ sample prepared at 1150°C . The (10) and (01) LEED spots of SiC and $B_xN_y-R0^\circ$ are marked by red and blue circles, respectively. The short blue line indicates where the radial line scan shown in (c) is recorded. Electron energy 165 eV. (b) Illustration of the LEED spot positions. Red and blue circles as in (a). All other spots originate from double diffraction processes involving both SiC and $B_xN_y-R0^\circ$, colored spots are explained in the text. (c) Radial line scan through the $B_xN_y-R0^\circ$ (01) diffraction spot. The asymmetric peak is fitted with two symmetric Voigt profiles. (d) As (a), but for a $B_xN_y-R0^\circ$ sample prepared at 1100°C .

and those of $B_xN_y-R0^\circ$ by blue circles. These are the only single diffraction spots visible in the LEED image. All other spots are due to multiple diffraction processes of the $B_xN_y-R0^\circ$ layer and the SiC substrate, as illustrated in Fig. 3.7(b): The "satellites" around the (00) spot are double-diffraction spots of the first order $B_xN_y-R0^\circ$ and SiC spots. E.g., the one indicated by a light green circle is due to diffraction at the $(01)_{\text{BN}}$ and the $(0\bar{1})_{\text{SiC}}$. Those located around the SiC first order reflections involve some higher order $B_xN_y-R0^\circ$ or SiC diffraction spots, e.g., $(02)_{\text{BN}} + (0\bar{1})_{\text{SiC}}$ (dark green), $(0\bar{1})_{\text{BN}} + (02)_{\text{SiC}}$ (orange), and $(10)_{\text{BN}} + (\bar{1}1)_{\text{SiC}}$ (magenta). All other spots marked by gray circles can be explained in a similar way. Note that all spots involving a first-order $B_xN_y-R0^\circ$ reflection are relatively strong and form the hexagon around the first-order SiC reflections. Spots involving the second-order $B_xN_y-R0^\circ$ reflections are weaker and *not* always visible. However, the disappearance of the $B_xN_y-R0^\circ$ $\{10\}$ and $\{01\}$ reflections and all the double diffraction spots at temperatures between 1175°C and 1200°C (see Fig. 3.6 and discussion above) indicates the transformation of the $B_xN_y-R0^\circ \rightarrow \text{lqG-}R0^\circ$ layer in this temperature range.

Owing to the high \mathbf{k} -space resolution of the SPA-LEED technique, radial line scans through the $B_xN_y-R0^\circ$ spots reveal an asymmetric profile as shown in Fig. 3.7(c). This was found for both the $B_xN_y-R0^\circ$ first order (single diffraction) reflections and all double diffraction spots involving a $B_xN_y-R0^\circ$ reflection. The peak broadening is symmetric to the SiC first-order reflections, the satellite is always broadened at the high- \mathbf{K}_\parallel side of the SiC bulk peak, which confirms that the satellites are double diffraction peaks involving the $B_xN_y-R0^\circ$ first order reflections. The asymmetric peak can be fitted by two symmetric Voigt profiles with a difference in \mathbf{k} -space of about 2 %BZ_{SiC}, see Fig. 3.7(c). While the main peak clearly stems from $B_xN_y-R0^\circ$, the side peak is possibly due to the formation of $\text{lqG-}R0^\circ$ at a very early stage. This is not only indicated by the difference in lattice parameters between $B_xN_y-R0^\circ$ and graphene but also by the small C_G component in the C1s XPS spectrum already visible at 1100°C, see Fig. 3.4(e).

Using the LEEDLab software [73, 74] the SPA-LEED images were corrected for distortions in order to determine the lattice parameters of the involved structures. Lattice parameters of 3.08(4) Å were determined for the SiC bulk and 2.60(3) Å for the $B_xN_y-R0^\circ$ layer. The latter indicates a $(3.6 \pm 1.2)\%$ expansion compared to literature values for hBN (2.51 Å [103]), i.e., the $B_xN_y-R0^\circ$ layer is significantly less densely packed than a 2D-hBN layer. From the width of the $B_xN_y-R0^\circ$ SPA-LEED peaks, in comparison to that of SiC bulk peaks, the average size of the $B_xN_y-R0^\circ$ domains can also be estimated. The main component of the line scan shown in Fig. 3.7(c) has a full width at half maximum (FWHM) of 1.709(8) %BZ_{SiC}, which is approximate twice the width

of the SiC bulk peaks ($0.853(1) \%BZ_{SiC}$). From these numbers, an approximate average domain size of 30 nm for the $B_xN_y-R0^\circ$ domains is estimated.

Fig. 3.7(d) shows a SPA-LEED pattern of a sample prepared at a lower temperature (1100°C). Besides the $B_xN_y-R0^\circ$ and SiC diffraction spots, this pattern also shows some additional spots stemming from a $(\frac{3}{-1} \frac{1}{2})$ superstructure. The unit cell is indicated by cyan arrows (solid and dashed for two mirror domains) in Fig. 3.7(d). As mentioned above, this pattern disappears when higher preparation temperatures are applied, clearly before the $B_{B_xN_y}$ and N 1s XPS peaks vanish. Furthermore, the reflections are sharp and rather intense in relation to the $B_xN_y-R0^\circ$ $\{10\}$ and $\{01\}$ reflections, suggesting that this superstructure does *not* stem from the $B_xN_y-R0^\circ$ layer but rather from a reconstruction of the SiC(0001) surface. Based on the preparation temperature (1100°C), it is expected that this reconstruction consists of B and Si adatoms, since it is known that a Si-rich reconstruction of SiC(0001) is stable in UHV up to 1050°C [104]. The $(\frac{3}{-1} \frac{1}{2})$ surface reconstruction is destroyed even before the $B_xN_y-R0^\circ \rightarrow \text{lqG-}R0^\circ$ layer transformation, i.e. already at preparation temperatures higher than 1100°C .

3.5 Vertical structure

In this section, the vertical structures of the $B_xN_y-R0^\circ$ and $\text{lqG-}R0^\circ$ samples determined by NIXSW are presented. Typical XPS spectra and the yield curves extracted from the XPS data are shown in Fig. 3.8(a)-(e) for the $B_xN_y-R0^\circ$ sample (preparation temperature 1150°C) and Fig. 3.8(f)-(j) for the $\text{lqG-}R0^\circ$ sample (1250°C).

The first crucial step in an analysis of NIXSW data is finding the best-fitting model for the XPS spectra. This is straightforward for the N 1s and Si 2s species since the spectra contain only one slightly asymmetric peak and can both be fitted well with one (asymmetric) Voigt profile. Also, the C 1s data is easily fitted, since the SiC and graphene species are well separated (see also Sec. 3.3). For B 1s, the analysis is more difficult. As discussed in Sec. 3.3, there are three components showing relatively small core-level shifts. It turned out that the data set recorded on the sample prepared at 1150°C can best be fitted with all three components under tight constraints, namely fixed binding energy differences of the $B_{B_xN_y}$ and B_{ZL} component relative to the B_{SiC} peak (1.76 eV and 0.97 eV, respectively). The B 1s fitting model is shown in Fig. 3.8(a) (see also Fig. 3.4(a)).

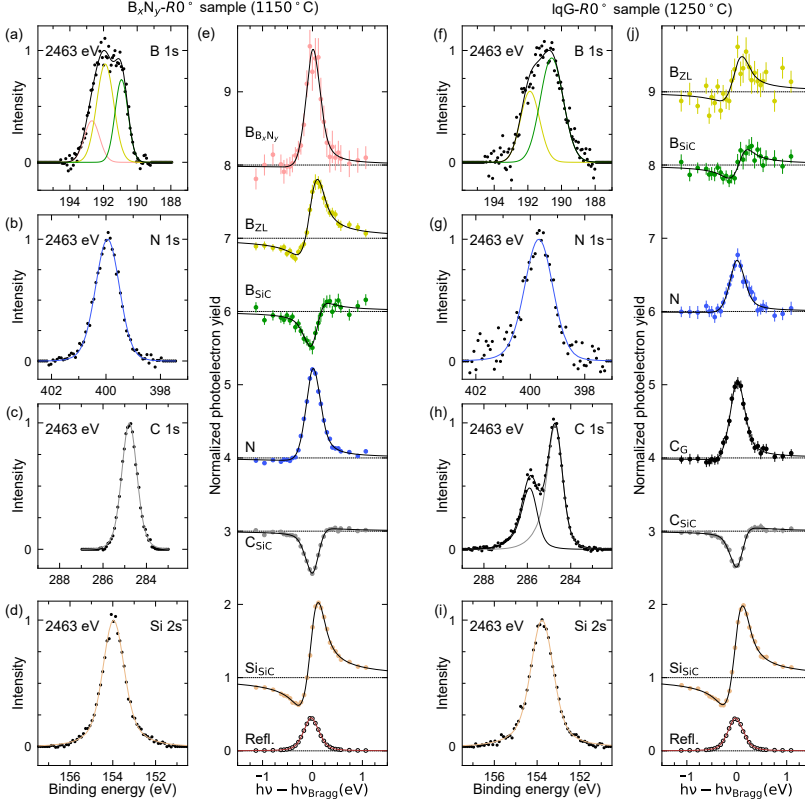


Figure 3.8: NIXSW results of the $B_xN_y-R0^\circ$ sample prepared at 1150°C and the $lqG-R0^\circ$ sample prepared at 1250°C . (a-d, f-i) Core-level spectra recorded at a photon energy ≈ 2 eV below the (0006) Bragg energy. Single peaks (solid lines) were fitted to the data, except for the B $1s$ (both samples) and C $1s$ spectra ($lqG-R0^\circ$ sample only), which were fitted using two- or three-component models. (e, j) Yield curves of the probed core-levels and reflectivity curve of the SiC(0006) Bragg reflection. In (e), the yield curves for $B_{B_xN_y}$, B_{ZL} , B_{SiC} , N, and C_{SiC} are displaced vertically by 7, 6, 5, 3, and 2, in (j) those for B_{ZL} , B_{SiC} , N, C_G and C_{SiC} by 8, 7, 5, 3, and 2, respectively.

Table 3.1: NIXSW results (averaged values from measurements on several spots on the sample) for the $B_xN_y-R0^\circ$ sample prepared at 1150°C and the lqG- $R0^\circ$ sample prepared at 1250°C. The distances z are given with respect to the topmost Si atoms of the substrate. $d_{hkl} = 2.520 \text{ \AA}$.

X	N_X	$B_xN_y-R0^\circ$			$lqG-R0^\circ$		
		P_c^H	F_c^H	$z [\text{\AA}]$	P_c^H	F_c^H	$z [\text{\AA}]$
$B_{B_xN_y}$	2	0.19(1)	0.95(10)	5.50(3)	–	–	–
N	2	0.18(1)	0.73(2)	5.46(3)	0.16(2)	0.36(7)	5.43(5)
C_G	2	–	–	–	0.18(1)	0.55(4)	5.47(3)
B_{ZL}	1	0.02(1)	0.69(3)	2.54(3)	-0.02(2)	0.50(10)	2.45(5)
Si_{SiC}	0	0.01(1)	1.06(4)	0.0	0.00(1)	1.02(1)	0.0
B_{SiC}	-1	0.78(1)	0.90(3)	–	0.82(1)	0.62(8)	–
C_{SiC}	-1	0.75(1)	0.92(1)	-0.65(3)	0.76(1)	0.85(1)	-0.62(3)

These models were used to extract NIXSW yield curves from the XPS data. Several yield curves on different sample positions were recorded. Fig. 3.8(e) shows a set of typical yield curves of each of the probed species and a reflectivity curve of the SiC(0006) reflection. From fitting the yield curves, the values for the coherent fractions F_c^H and coherent positions P_c^H are obtained, and their averages listed in Table 3.1. Fig. 3.9(a) shows a so-called Argand diagram, which illustrates the results of all individual scans as vectors in a polar diagram with F_c^H as the length and P_c^H as the polar angle. This diagram illustrates very well the basic findings of our NIXSW analysis: All coherent fractions are sufficiently high to indicate single-height adsorption of the individual species, with some slight disorder in some cases, see below. In particular, three different boron species are very clearly confirmed, since their coherent positions are very different.

For the sample prepared at 1150°C, both $B_{B_xN_y}$ and N have very similar P_c^H , indicating that these species are located within one layer with only a small buckling. The B_{ZL} layer below is similarly flat, since its F_c^H is close to that of N in the $B_xN_y-R0^\circ$ layer, although smaller than that of $B_{B_xN_y}$. The third boron species, B_{SiC} , is attributed to boron atoms diffusing into the bulk. Its F_c^H is surprisingly high, indicating that boron adopts well-defined doping sites in the bulk.

In the sample prepared at 1250°C, the $B_xN_y-R0^\circ$ layer was replaced by lqG- $R0^\circ$, as discussed in Sec. 3.3. Hence, when fitting the B 1s spectra, the best results were obtained with the $B_{B_xN_y}$ component removed from the fitting model, and with constraining the FWHM of the B_{SiC} component to 1.2 times that of B_{ZL} (see Fig. 3.8(f)). Alternatively, I also tried to use the three-

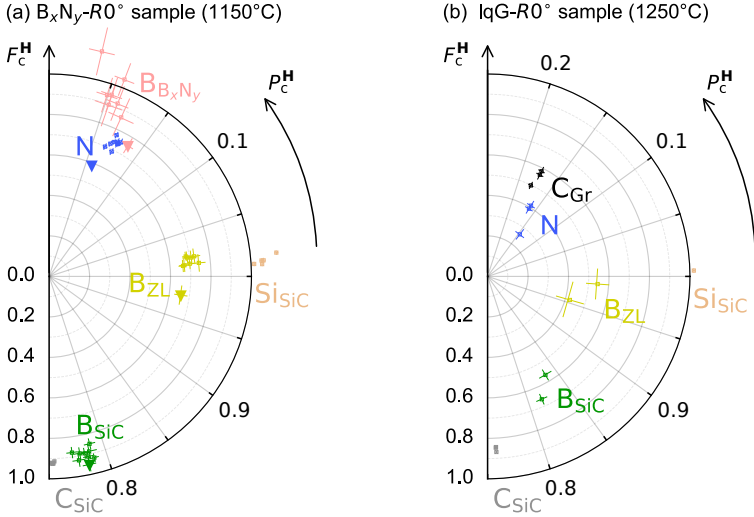


Figure 3.9: Argand diagrams summarizing the NIXSW fit results of (a) $B_xN_y-R0^\circ$ and (b) $lqG-R0^\circ$ on SiC. The results of all individual measurements are shown as data points representing a polar vector with F_c^H as its length and P_c^H as its polar angle.

component fitting model used for the $B_xN_y-R0^\circ$ sample, but the fitting was more unstable, and the results, therefore, were less reliable. For the other spectra (C 1s, N 1s, and Si 2s) the fitting models are unchanged. The NIXSW yield curves obtained for this sample are presented in Fig. 3.8(j). The NIXSW results are shown in the Argand diagram in Fig. 3.9(b) and their averages are listed in Table 3.1.

It is obvious that some coherent fractions are smaller for the $lqG-R0^\circ$ compared to the $B_xN_y-R0^\circ$ sample, in particular for B_{ZL} , B_{SiC} , and N. For the latter, this is easy to understand, since the $B_xN_y-R0^\circ$ layer does not exist anymore and the small remaining amount of N does not occupy such a well-defined vertical position. Its coherent position, however, which is very close to that of carbon in the $lqG-R0^\circ$, indicates that the majority of the remaining nitrogen acts as a dopant of the $lqG-R0^\circ$ layer, similar to Ref. [105].

For the two boron species B_{ZL} and B_{SiC} , it means that more vertical disorder is introduced by the higher temperature. This is, in particular, interesting for the boron zeroth-layer, since it might explain why the graphene layer above also exhibits a significantly smaller coherent fraction compared to the $B_xN_y-R0^\circ$ layer. For the $B_xN_y-R0^\circ$ layer F_c^H of 0.73 and 0.95 were found for N and

B_xN_y , respectively. After the transformation of this layer to $lqG-R0^\circ$, $F_c^H = 0.55$ for was measured for C_G in $lqG-R0^\circ$. This is attributed to the fact that the graphene layer is of lower quality compared to the sample produced by the alternative scenario at even higher temperatures, where no $B_xN_y-R0^\circ$ precursor structure can form [97]. It also agrees with the finding of a rather weak Dirac cone in the ARPES experiments (Fig. 3.3) and rather weak and blurry LEED spots (Fig. 3.6).

Based on these results, structural models for the $B_xN_y-R0^\circ$ and the $lqG-R0^\circ$ samples are shown in Fig. 3.10. It is remarkable that the boron nitride layer in the $B_xN_y-R0^\circ$ sample and the graphene layer in the $lqG-R0^\circ$ sample are almost precisely found at the same height above the SiC surface – 5.48 Å (average of the B and N heights) and 5.47 Å, respectively – while the boron zeroth-layer is slightly closer to the substrate in the $lqG-R0^\circ$ sample compared to $B_xN_y-R0^\circ$ (2.45 Å instead of 2.54 Å). But when considering the distances in units of the expected van der Waals (vdW) bonding distance, it can be seen that the effective interaction strength does not differ significantly. In these units, the distances to the zeroth-layers are almost identical (80.6% for the average of B and N in $B_xN_y-R0^\circ$, and 83.4% for C in $lqG-R0^\circ$, see Table 3.2).

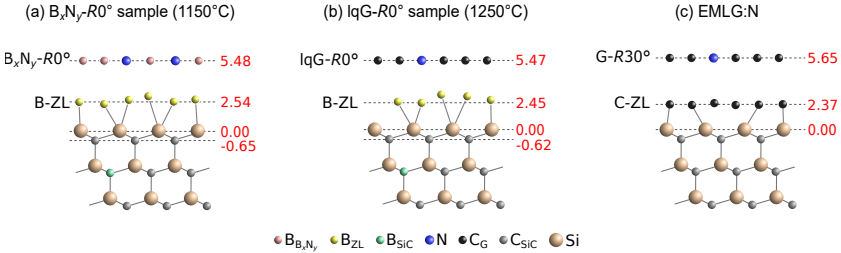


Figure 3.10: Ball-and-stick models of the vertical structures of (a) $B_xN_y-R0^\circ$ and (b) $lqG-R0^\circ$ and (c) EMLG:N on SiC. The latter is reproduced from Ref. [105]. Note that in (a) and (b) the ZL consists of boron, and in (c) of carbon. Numbers represent vertical distances to the uppermost Si layer in Å.

A comparison to values obtained by Sforzini [105] for the N-doped monolayer graphene (EMLG:N), which is located on a carbon bufferlayer (graphene zeroth-layer), is more instructive: Although the van der Waals radii of the species in the zeroth-layer are smaller in the EMLG:N system (1.70 Å for C compared to 1.92 Å for B), the distance of the EMLG:N layer itself to the zeroth-layer is clearly larger, even in absolute units (3.28 Å vs. 3.02 Å for $lqG-R0^\circ$). This difference, 83.4% vs. 90.6% of the vdW distances, indicates the rather strong interaction of $lqG-R0^\circ$ to its substrate, in agreement with weak

and broad Dirac bands seen in ARPES and faint reflection spots in LEED, while the decoupling of the EMLG:N layer from the substrate is significantly better.

Table 3.2: Bond length analysis. The distances between the layers ($B_xN_y-R0^\circ$ layer to ZL, $lqG-R0^\circ$ layer to ZL, and ZL to substrate) as obtained from NIXSW, are listed in Å and in percentage of the corresponding van der Waals bonding distance (% vdW). For $B_xN_y-R0^\circ$ and $lqG-R0^\circ$, the ZL consists of boron, and for EMLG:N of carbon. Van der Waals radii are taken from Ref. [106].

Bond type	vdW [Å]	Distances [Å] and [%vdW]					
		$B_xN_y-R0^\circ$		$lqG-R0^\circ$		EMLG:N [105]	
$B_{B_xN_y} - ZL$	3.84	2.94	77.1%	–	–	–	–
$N_{BN} - ZL$	3.47	2.92	84.1%	2.98	85.9%	3.35	96.5%
$C_{lqG} - ZL$	3.62	–	–	3.02	83.4%	3.28	90.6%
ZL - Si	4.02	2.54	63.2%	2.45	60.9%	2.37	59.0%

Another obvious conclusion to be drawn from the analysis of bonding distances is that the $B_xN_y-R0^\circ$ layer is located closer to the ZL than a mere van der Waals interaction would suggest. $B_{B_xN_y}$ and N are located at 77% and 84% of the B-B and N-B van der Waals bonding distances, respectively, see Table 3.2. This can be understood as a first indication of an (at least partly) chemisorptive (covalent) interlayer interaction.

3.6 Conclusion

The transition of $B_xN_y-R0^\circ$ to $lqG-R0^\circ$ on SiC(0001) at preparation temperatures between 1100°C and 1250°C is investigated. At 1150°C, a $B_xN_y-R0^\circ$ layer is formed, which is located above a boron zeroth-layer and aligned with the substrate (0° rotation). It turned out that this layer is *not* decoupled from the surface, as it does *not* show the typical band structure of a 2D-hBN layer and it is *not* stable in air. Nevertheless, it has only a small corrugation as indicated by a high coherent fraction obtained from NIXSW.

At preparation temperatures higher than 1225°C, the $B_xN_y-R0^\circ$ layer transforms gradually to $lqG-R0^\circ$ conserving its orientation, hence, graphene is formed in the unconventional orientation of 0° with respect to the SiC substrate. Some of the nitrogen atoms remain in the layer as dopants, as indicated by the almost identical adsorption heights for C and N in $lqG-R0^\circ$. This high doping level might also be contributing to the fact that the quality of the graphene layer is rather poor. An important finding is that in both cases

(the $B_xN_y-R0^\circ$ layer before and the lqG- $R0^\circ$ layer after the transition) the interaction of the topmost layer with the underlying substrate is relatively strong, much stronger than for the case of an N-doped EMLG- $R30^\circ$ layer. This is indicated by relative bonding distances of $\approx 80\%$ (average of B and N in $B_xN_y-R0^\circ$), 83% (lqG- $R0^\circ$), and more than 90% (EMLG- $R30^\circ$) of the expected vdW distances.

Note that the quality of the lqG- $R0^\circ$ can be significantly improved by using the so-called "surfactant method" for preparation, as proposed in Ref. [97]. With this preparation route, which basically applies an even higher preparation temperature, no $B_xN_y-R0^\circ$ precursor structure is formed prior to the formation of a high quality $R0^\circ$ graphene layer that is decoupled from the SiC substrate by a graphene zeroth-layer. This system is supposed to serve as a perfect starting point to produce a 30° twisted bilayer graphene by transforming the carbon zeroth-layer into a (conventionally oriented) graphene layer, e.g., by hydrogen intercalation.

Chapter 4

0°-rotated Graphene on 6H-SiC(0001)

As motivated in chapter 1 and 3 for the bilayer graphene, the twist angle between graphene layers influences the electronic properties of the stacked system [85]. In 30°-tBLG, electrons are expected to localize, giving rise to flat bands and strong correlation physics [120–123]. Also, large twist angle tBLG is predicted to show nontrivial higher-order band topology [22]. In chapter 3, it was found that the B_xN_y - $R0^\circ$ on SiC(0001) transitions to lqG - $R0^\circ$ with increasing preparation temperature. It is rather intuitive to study the system at even higher preparation temperatures, since this kind of epitaxial growth provides not only reproducible control of lattice orientation but also scalability.

In this chapter, two routes to prepare epitaxial single-layer graphene with unconventional 0° orientation on SiC(0001) are compared. The first route, the template method, uses a B_xN_y - $R0^\circ$ sample as a template (see chapter 3) and anneals it in UHV at 1300°C for 30 min. The B_xN_y - $R0^\circ$ layer is thus replaced by G - $R0^\circ$ conserving the 0° orientation. This route (also reported in Ref. [95]) produces so-called "template graphene" (template-induced unconventionally oriented graphene, T graphene), which is prepared in the same way as the lqG - $R0^\circ$ only at higher temperatures. The second route, the surfactant method, uses borazine as a surfactant. The (3×3) reconstructed SiC(0001) surface is prepared at 880°C, thereafter, exposed to borazine atmosphere at 1×10^{-6} mbar. The preparation temperature is then quickly ramped up to 1300°C and kept for 30 min, leading to the formation of high-quality G - $R0^\circ$. This route produces "surfactant graphene" (surfactant-induced unconventionally oriented graphene, S graphene). For both systems, SPA-LEED measurements were performed to study their lateral structures. ARPES was used to verify the existence of graphene and compare its quality. And, in particular, the NIXSW technique provided crucial insight into the vertical structure of

the stacking as well as the coverages of the graphene layers.

Please note that this project was originally started by Markus Franke and continued by Shayan Parhizkar, Nafiseh Samiseresht, and me. Samples mentioned in this chapter were prepared by Markus Franke, Dr. François C. Bocquet, and myself. The SPA-LEED measurements were carried out by me with some assistance from Shayan Parhizkar. The NIXSW measurements were carried out by a team of experimentalists during several beamtimes at beamline I09, Diamond Light Source, Didcot, UK. This chapter is published in Ref. [97]. The ARPES measurements in this chapter are performed by Markus Franke, Nafiseh Samiseresht, and Dr. François C. Bocquet.

4.1 Lateral structure

As discussed in chapter 3, $B_xN_y-R0^\circ$ is a structure related to $G-R0^\circ$ because of the same lattice orientation and similar way of preparation. Fig. 4.1 shows the transition from $B_xN_y-R0^\circ$ to T graphene in high-resolution LEED patterns. In Fig. 4.1(a), the diffraction spots corresponding to $B_xN_y-R0^\circ$ (dotted black circles) are broader in the radial direction than the substrate spots, indicating that the average $B_xN_y-R0^\circ$ domain size is smaller than the SiC terrace size. In Fig. 4.1(b), the lattice parameter corresponding to the spots marked by dashed blue circles is smaller compared to the one found for $B_xN_y-R0^\circ$ and corresponds to $G-R0^\circ$. The average domain size of this sample is even smaller than that of $B_xN_y-R0^\circ$, indicating the $G-R0^\circ$ to be of low quality. Moreover, if these samples are exposed to air for 48 hours, the diffraction patterns of both cannot be recovered by mild annealing in UHV (see also Sec. 3.2). As hBN and graphene are known to be stable in air, such observations suggest that neither $B_xN_y-R0^\circ$ nor $lqG-R0^\circ$ form a closed layer, thus allowing the oxidation of SiC and the interface layer.

In Fig. 4.1(c), the elongated diffraction spots marked by blue circles are assigned to $G-R0^\circ$. Additionally, diffraction spots (purple circles) corresponding to a similar lattice parameter but aligning with $\Gamma\bar{K}_{SiC}$ ($G-R30^\circ$) are present. They originate from $G-R30^\circ$ that is formed most likely underneath the $G-R0^\circ$ (see Sec. 4.3). Nonetheless, the background remains noticeable, indicating that large areas without long-range order exist. Therefore, it appears that neither $B_xN_y-R0^\circ$ nor $lqG-R0^\circ$ are adequate starting points to form high-quality 30° -tBLG by further annealing.

Before going in-depth with the experimental results of SPA-LEED on S graphene and T graphene, it is useful to consider the diffraction patterns expected for $G-R0^\circ$, $G-R30^\circ$, and $ZLG-R30^\circ$ layers on SiC(0001). The diffraction spots stemming from each of the structures present at the surface of S graphene samples are represented in Fig. 4.2(b, d, f) by circles and by the

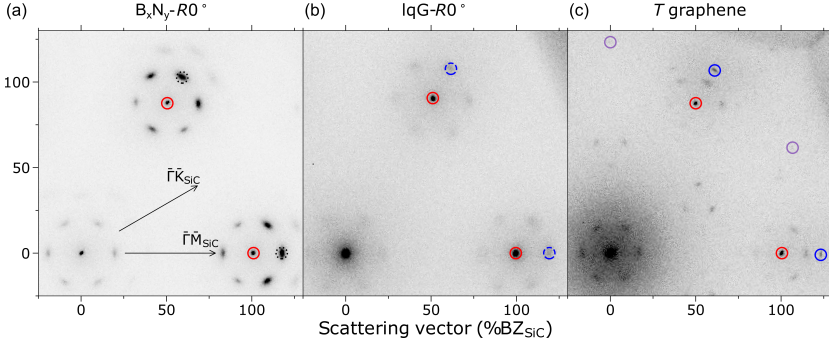


Figure 4.1: Diffraction pattern of (a) $B_x N_y$ - $R0^\circ$ (b) lqG - $R0^\circ$ and (c) T graphene measured with SPA-LEED at 165 eV. First-order diffraction spots are assigned as follows: red - $6H$ -SiC(0001); dotted black - $B_x N_y$ - $R0^\circ$; dashed blue - lqG - $R0^\circ$; blue - G - $R0^\circ$ and purple - G - $R30^\circ$. The high symmetry directions of the SiC surface Brillouin zone are indicated by arrows in (a). The gray scale is linear. Images are not corrected for distortion.

following colors: SiC(0001) – red, ZLG - $R30^\circ$ – green, G - $R0^\circ$ – blue. Diffraction spots stemming from multiple diffraction involving more than one structure are represented by a color that is the red-green-blue (RGB) sum of the assigned colors of the involved structures. Different symbols represent a different number of structures involved: \diamond for two, and \square for three structures. The resulting color code is summarized in Table 4.1. Note that only spots and vectors relevant to the present discussion are displayed. That is, not all visible spots are shown. The lattice vectors of the structures simulated are represented by arrows with corresponding colors in Fig. 4.2(a, c, e).

Table 4.1: Color code used in Fig. 4.2 and Fig. 4.4 for indicating single, double, and triple diffraction spots in the (schematic) LEED images.

	<i>Involved structures</i>	<i>(RGB) value</i>	<i>color</i>
\circ	SiC	(1,0,0)	red
\circ	ZLG - $R30^\circ$	(0,1,0)	green
\circ	G - $R0^\circ$	(0,0,1)	blue
\diamond	SiC + ZLG - $R30^\circ$	(1,1,0)	yellow
\diamond	SiC + G - $R0^\circ$	(1,0,1)	magenta
\diamond	ZLG - $R30^\circ$ + G - $R0^\circ$	(0,1,1)	cyan
\square	SiC + ZLG - $R30^\circ$ + G - $R0^\circ$	(1,1,1)	white

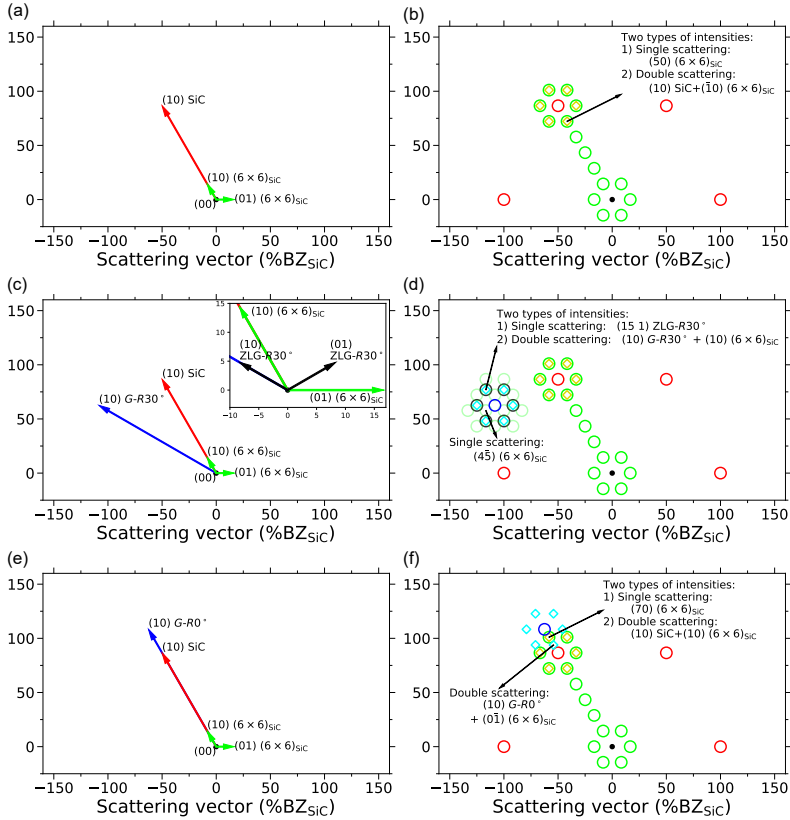


Figure 4.2: Step-by-step geometrical construction to explain the origin of diffraction spots of $G-R0^\circ$. For the satellites centered around the $\{10\}$ SiC spots, the relevant vectors are defined in (a), and a selection of spots is shown in (b) together with a list of possible diffraction paths. Additional information regarding the satellites around the $G-R30^\circ$ $\{10\}$ spots are given in (c-d) and for the satellites around the $G-R0^\circ$ $\{10\}$ spots in (e-f).

In Fig. 4.2(a), the relevant reciprocal surface lattice unit vectors of SiC and $(6 \times 6)_{\text{SiC}}$ reconstruction are depicted. The $(6 \times 6)_{\text{SiC}}$ spots stemming from the ZLG- $R30^\circ$ reconstruction (independent of the presence of G- $R0^\circ$ or G- $R30^\circ$ atop) are shown in Fig. 4.2(b) by summing up the (10) scattering vector of SiC and the fundamental vectors of the $(6 \times 6)_{\text{SiC}}$ reconstruction. Because of the commensurability ($6a_{\text{SiC}} = a_{(6 \times 6)_{\text{SiC}}}$, where a_{SiC} and $a_{(6 \times 6)_{\text{SiC}}}$ are the lattice parameters of the SiC and $(6 \times 6)_{\text{SiC}}$ reconstruction, respectively), scattering only on the $(6 \times 6)_{\text{SiC}}$ vectors (green circles) is equivalent to scattering on both $(6 \times 6)_{\text{SiC}}$ and SiC vectors (dark yellow diamonds) in Fig. 4.2(b).

In Fig. 4.2(c), reciprocal surface lattice unit vectors of G- $R30^\circ$ and ZLG- $R30^\circ$ ($(6\sqrt{3} \times 6\sqrt{3})$ - $R30^\circ$) are added. The inset presents a zoom around the origin. Note that $a_{\text{ZLG-R}30^\circ} \approx 13a_{\text{G-R}30^\circ}$, where $a_{\text{ZLG-R}30^\circ}$ and $a_{\text{G-R}30^\circ}$ are the lattice parameters of the ZLG- $R30^\circ$ and G- $R30^\circ$, respectively. In Fig. 4.2(d), the (10) spot of G- $R30^\circ$ is depicted as a blue circle. The six spots around it at a distance of 16.67 %BZ $_{\text{SiC}}$ can be explained both by scattering with ZLG- $R30^\circ$ vectors only (black circles), or by the double scattering on both ZLG- $R30^\circ$ and $(6 \times 6)_{\text{SiC}}$ vectors (cyan diamond). Scattering on the $(6 \times 6)_{\text{SiC}}$ vectors only (light green circles) cannot reproduce these six spots.

Finally, one can turn to the case of G- $R0^\circ$ on ZLG- $R30^\circ$ (Fig. 4.2(e-f)). Given the structural relationship between the $(6 \times 6)_{\text{SiC}}$ and G- $R0^\circ$, the question arises immediately as to the nature of the six scattering spots around the G- $R0^\circ$ spots as in Fig. 4.1(c) (indicated by cyan diamonds in Fig. 4.2). Since they do not coincide with the genuine $(6 \times 6)_{\text{SiC}}$ but at the same time their distance to the G- $R0^\circ$ (10) spot corresponds to the $(6 \times 6)_{\text{SiC}}$ unit vectors, only one explanation remains: They must stem from the double scattering on vectors of both $(6 \times 6)_{\text{SiC}}$ and G- $R0^\circ$, as shown in Fig. 4.2 (e-f).

Note that recent x-ray diffraction results by two independent groups revealed that the ZLG- $R30^\circ$ is not commensurate to the bulk of SiC [136–138]. Actually, the ZLG- $R30^\circ$ and the Si-terminated SiC substrate surface form an incommensurate supercell with a real space period of $6.037(2)a_{\text{SiC}}$. Additionally, the presence of a graphene layer affects the lattice parameter of the ZLG- $R30^\circ$ below. It is also established that ZLG- $R30^\circ$ has a slightly different lattice parameter than graphene. However, the deviation from the commensurate case is small and can not be resolved by electron diffraction. Both LEED and SPA-LEED see SiC, ZLG- $R30^\circ$, and G- $R30^\circ$ as commensurate to each other. It has even been demonstrated that the G- $R0^\circ$ /ZLG- $R30^\circ$ stack exhibits quasi-crystalline order [30, 135, 139]. For this reason, although there are only small deviations in either twist angle or lattice parameters, no commensurability between ZLG- $R30^\circ$ and G- $R0^\circ$ is expected.

Fig. 4.3(a) and (b) display the high-resolution LEED measurement of T graphene and S graphene, respectively. For S graphene, compared to

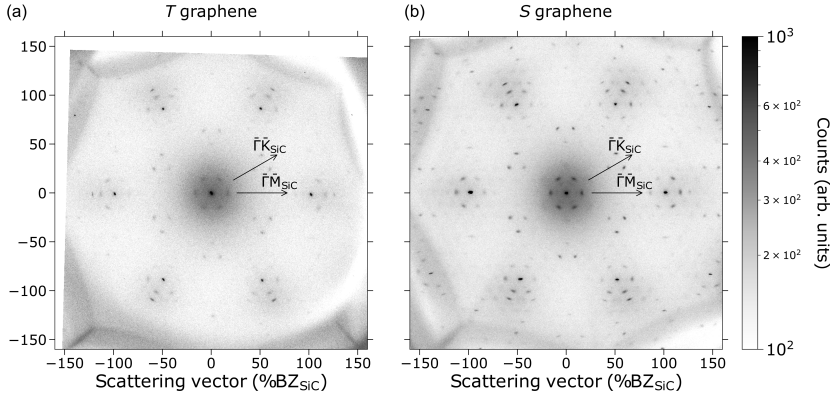


Figure 4.3: Diffraction pattern of (a) *T* graphene and (b) *S* graphene measured with SPA-LEED at 165 eV. The gray scale is logarithmic to enhance the intensity diffraction spots. Image distortion was corrected with LEED-cal-corr (v. 1.3).

T graphene, the diffraction spots are narrower, and more ZLG- $R30^\circ$ spots (in particular the $(6 \times 6)_{\text{SiC}}$ spots) as well as multiple scattering spots are visible. This indicates *S* graphene is of higher layer quality than *T* graphene. Note that the G- $R30^\circ$ diffraction spots are not really visible on *S* graphene, while on *T* graphene, the G- $R30^\circ$ spots can be seen in all six directions. Nonetheless, the G- $R30^\circ$ $\{10\}$ diffraction spots are weaker compared to the G- $R0^\circ$ $\{10\}$ spots (see Fig. 4.1(c) and Fig. 4.3(a)). Two possible scenarios may lead to this result: (1) G- $R30^\circ$ lies underneath G- $R0^\circ$ and give rise to lower spot intensity due to attenuation. (2) G- $R30^\circ$ and G- $R0^\circ$ lie on the same height and the intensity ratio corresponds to the relative amount of the two. So far, there is no direct way to determine which scenario leads to this measurement result. However, with the help of NIXSW, it is possible to correlate the lateral structure to the vertical and have a reasonable hypothesis, see Sec. 4.3 and Sec. 4.4. Note that the diffraction pattern of *S* graphene can be recovered by mild annealing in UHV after two months of air exposure. It indicates that the surfactant route yields a closed layer of G- $R0^\circ$ on ZLG- $R30^\circ$ with high crystalline quality and coverage, which protects the SiC surface quality against oxidation.

Fig. 4.4(a) shows the upper half of Fig. 4.3(b) with the left side superimposed with simulated diffraction spots. Fitting the corrected diffraction pattern yields lattice parameters of $32.1 \pm 0.4 \text{ \AA}$ for ZLG- $R30^\circ$ and $2.45 \pm 0.04 \text{ \AA}$ for G- $R0^\circ$. Fig. 4.4(b) shows the spot profiles of the SiC (10) in the radial

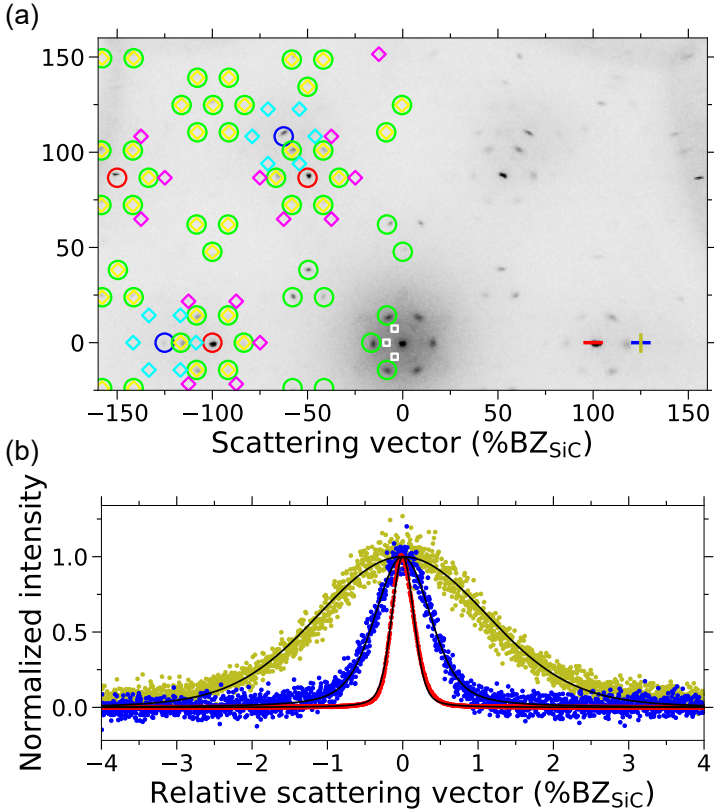


Figure 4.4: (a) Distortion-corrected SPA-LEED pattern of S graphene. Diffraction spot positions were simulated for each of the three structures (empty circle: SiC(0001), red; ZLG- $R30^\circ$, green; G- $R0^\circ$, blue) and for multiple electron diffraction by two (\diamond) and three (\square) structures (see color code in Table 4.1). (b) Typical radial profile of the $\{10\}$ SiC spot (red) as well as radial (blue) and azimuthal (olive green) profiles of the $\{10\}$ spot of G- $R0^\circ$. Colored dots represent experimental data, black lines represent the best fits. The paths used for the spot profiles are indicated in (a) as colored lines.

direction (red), the radial (blue) and azimuthal (olive green) direction of the G - $R0^\circ$ spot. The full widths at half maxima w of the radial spot profiles arise from the combined effects of the finite instrumental resolution and the finite size of crystalline domains. Hence, $2\pi/w$ represents a lower limit to the average domain size. An azimuthal profile broader than the radial profile is a direct indication of azimuthal disorder. To estimate the azimuthal distribution, assumed in this particular case to be Gaussian, the radial fit profile (Voigt) is convoluted with a Gaussian in order to fit the azimuthal profile. The fitted standard deviation σ of the Gaussian is a measure of the azimuthal disorder. The $\{10\}$ SiC spots (red) have a circular shape and the radial profile is fitted by a Voigt function with $w = (0.341 \pm 0.004) \%BZ_{\text{SiC}}$. In contrast, the $\{10\}$ radial spot profiles of the G - $R0^\circ$ (blue) are broader, $(0.863 \pm 0.009) \%BZ_{\text{SiC}}$, indicating a smaller average domain size than the average SiC terrace size. Moreover, the $\{10\}$ spots of G - $R0^\circ$ are elongated in the azimuthal direction (olive green), corresponding to an azimuthal disorder with the standard deviation $\sigma = (0.458 \pm 0.002)^\circ$.

In this section, a qualitative comparison between S graphene and T graphene was given with high-resolution LEED measurements, indicating that S graphene has a larger average domain size than T graphene. Quantitative spot profile analysis on S graphene was carried out, showing that the G - $R0^\circ$ average domain size is smaller than the average SiC terrace size by a factor of 2.5. The G - $R0^\circ$ has an azimuthal disorder and has the lattice orientation distributing with a standard deviation of $(0.458 \pm 0.002)^\circ$. Since the diffraction measurements only provide information about lateral order, the electronic properties are determined using ARPES (see next section) and NIXSW experiments were carried out to determine the vertical order of these stacked systems (see Sec. 4.3).

4.2 Electronic band structure

To track the presence of graphene in both 0° and 30° orientations with respect to the SiC lattice, and to assess graphene quality, ARPES measurements were performed on samples prepared at different temperatures. Energy distribution maps (EDMs) were taken around \bar{K}_{0° (stemming from G - $R0^\circ$) and \bar{K}_{30° (from G - $R30^\circ$) to verify the Dirac cones of graphene. The intensity grayscale around \bar{K}_{30° is enhanced by a factor of 2 with respect to the data around \bar{K}_{0° . Note that the samples are prepared in a way that there is always a temperature gradient on the sample during preparation, see Sec. 3.3. Therefore, even though the preparation temperatures for both T graphene and S graphene are set at 1300°C , the actual preparation temperatures of each sample are slightly different.

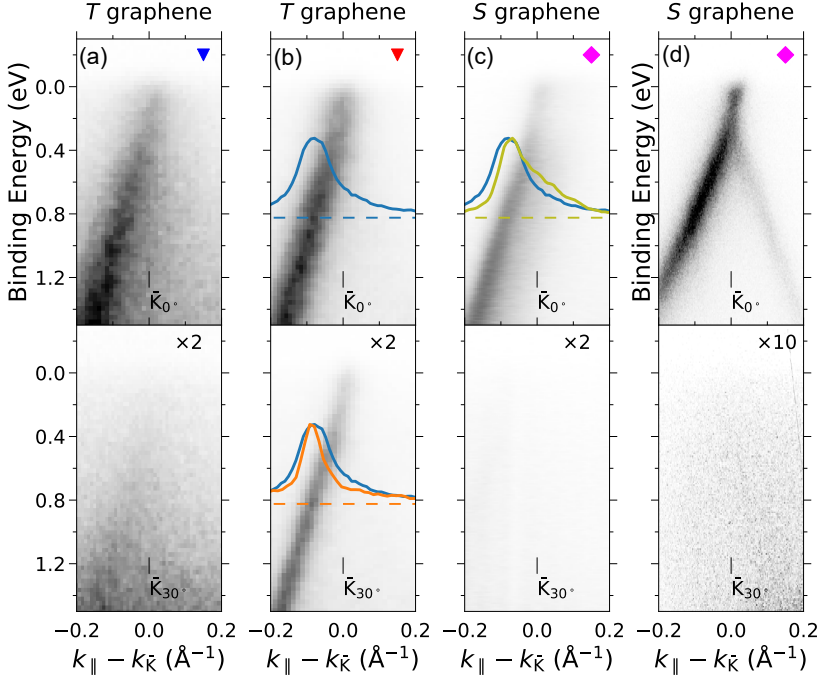


Figure 4.5: ARPES EDMs taken at beamline I09 of the Diamond light source with $h\nu = 110$ eV for (a)-(c) around \bar{K}_{0° (upper) and \bar{K}_{30° (lower, color scale magnified by a factor of 2) for T graphene prepared at (a) 1270°C and (b) 1330°C (75° incidence angle) and (c) for S graphene prepared at 1330°C (87° incidence angle). (d) Same maps as in (c) but measured with $h\nu = 21$ eV at our home laboratory (color scale for \bar{K}_{30° magnified by a factor of 10). Normalized momentum distribution curves taken at a binding energy of about 0.8 eV (dashed lines) around \bar{K}_{0° (blue) and \bar{K}_{30° (orange) are shown as solid lines. These measurements were carried out by Markus Franke, Nafiseh Samiseshrt, and Dr. François C. Bocquet.

Fig. 4.5(a) and (b) show EDMs of T graphene prepared at 1270°C and 1330°C, respectively. With increasing preparation temperature, the signal-to-background ratio increases. Also, the Dirac cone intensity ratio of G- $R30^\circ$ over G- $R0^\circ$ increases and the FWHM of the π band decreases with increasing preparation temperature. Fig. 4.5(c) and (d) show EDMs of S graphene prepared at 1330°C measured with $h\nu = 110$ eV and 21 eV, respectively. With both photon energies, S graphene shows a Dirac cone around \overline{K}_{0° of comparable quality as for the high preparation temperature side of T graphene, but no intensity was found around \overline{K}_{30° . Moreover, the EDMs remain unchanged for preparation temperatures ranging from 1300°C to 1360°C, thus only the one recorded at 1330°C is shown.

By comparing the EDMs of both T graphene and S graphene, one may notice that for T graphene, a lower coverage of G- $R30^\circ$ comes along with a broad π band for G- $R0^\circ$ (Fig. 4.5(a)). For S graphene, a sharp π band can be achieved for G- $R0^\circ$, without growing G- $R30^\circ$, proving improved homogeneity and quality of G- $R0^\circ$. This supports again that the S graphene is a better platform for preparing tBLG than T graphene. Interestingly, for T graphene, the FWHM of the π band is smaller around \overline{K}_{30° than around \overline{K}_{0° (see colored curves in Fig. 4.5(b)). However, for both G- $R0^\circ$ and G- $R30^\circ$ in either T or S graphene, the FWHM of the π band remains larger than for EMLG [105] and the Dirac point is located at about 200 meV below the Fermi level. Two facts can explain these observations. First, doping by substitutional N and B atoms is observed in XPS, and this doping is known to have led to band broadening [105]. Second, the sizeable azimuthal distribution observed in SPA-LEED for the G- $R0^\circ$ layer in S graphene (Fig. 4.4) and T graphene (Fig. 4.1(c)) samples can also contribute to the broadening around \overline{K}_{0° .

4.3 Vertical structure

In order to disentangle the vertical structure, XPS and NIXSW were performed. However, the situation is rather difficult in this case, since carbon species are located in up to three layers (ZLG- $R30^\circ$, G- $R30^\circ$, and G- $R0^\circ$) at (potentially) different heights. In other cases, it would be easy to separate the signals stemming from different layers that have different chemical surroundings, and hence, different core-level shifts. But, as expected, chemical shifts in the graphene components of the C 1s core-level are found neither in T or S graphene (Fig. 4.6(a)). Hence, a more sophisticated analysis of the NIXSW data is required, based on some assumptions, but in the end, providing insight into the coverages of the individual graphene layers.

As discussed in Sec. 3.3, also the samples presented in this section are prepared with temperature gradients. In Fig. 4.6(a), C 1s core-level spectra

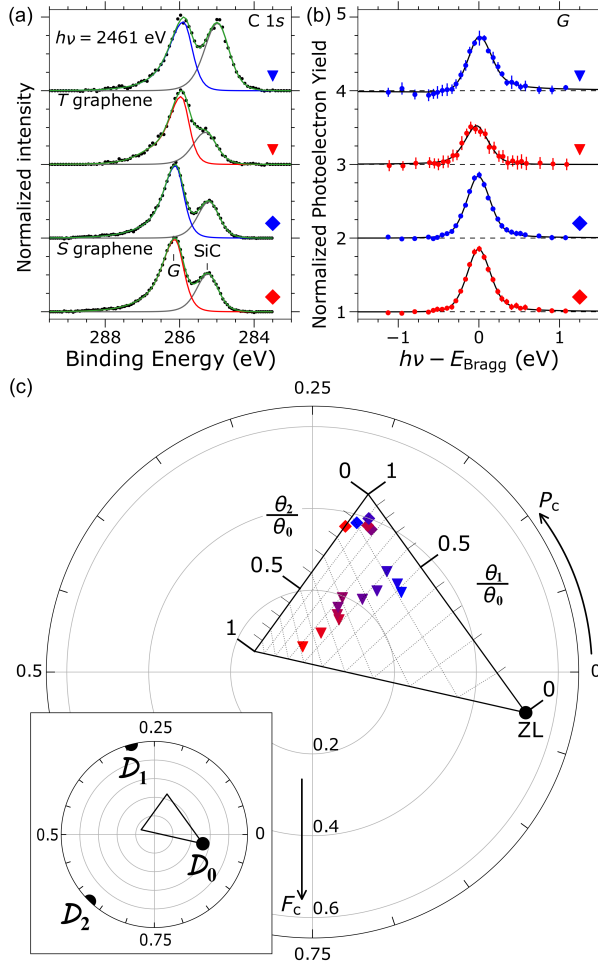


Figure 4.6: (a) C 1s core-level spectra taken off Bragg with a two-component fit model for T graphene and S graphene. Blue (red) corresponds to 1270°C (1330°C) for T graphene and 1300°C (1360°C) for S graphene. (b) The corresponding yield curves of the high-binding-energy component (G) are shifted by 1 in yield for clarity. The colored points are the data; the black lines are the fits. (c) Argand diagram summarizing all NIXSW fit results obtained from T graphene (filled inverted triangles) and from S graphene (filled diamonds). The large black full circles in the inset represent the expected vectors \mathcal{D}_0 , \mathcal{D}_1 and \mathcal{D}_2 and constitute the anchoring points of the additional axes θ_1/θ_0 and θ_2/θ_0 .

are shown for the lowest (blue) and highest (red) preparation temperature for T and S graphene. The component at low binding energy can clearly be attributed to carbon in the SiC bulk, while the component at higher binding energy is graphene-related, representing the sum of the C 1s yields from the ZLG- $R30^\circ$, the G- $R0^\circ$, and the G- $R30^\circ$ layers. Furthermore, NIXSW identifies graphene-related layers by their different adsorption heights (G -ZL, G -1st, and G -2nd) independently from their azimuthal orientations.

For such a three-layer system, an NIXSW analysis was carried out to disentangle the relative coverages of the individual layers. Since the G -ZL, G -1st and G -2nd layers are inseparable in XPS (only one peak entitled G in Fig. 4.6(a)). In a NIXSW experiment, the Fourier transform

$$\mathcal{D} = \int_0^{d_{hkl}} D(z) e^{2\pi i \frac{z}{d_{hkl}}} dz \quad (4.1)$$

at spatial frequency $2\pi/d_{hkl}$, where d_{hkl} is Bragg spacing, of the height distribution function

$$D(z) = \frac{1}{N} \sum_{i=1}^N \delta(z - d_i) \quad (4.2)$$

of photoemitters is measured [79,189]. N is the total number of photoemitters that contribute to a given signal. As a number in the complex plane,

$$\mathcal{D} = F_c^{\mathbf{H}} e^{2\pi i P_c^{\mathbf{H}}} \quad (4.3)$$

is parameterized by two parameters, the modulus $F_c^{\mathbf{H}}$ is known as the coherent fraction, and the reduced phase $P_c^{\mathbf{H}}$, the coherent position, see Sec. 2.3.

For the case of a stacked system with three graphene-like layers, the distribution function of photoemitters is a superposition of three sharp delta distributions at the height of each layer n ($n = 0, 1, 2$),

$$D(z) = \frac{1}{N_0 + N_1 + N_2} \left(\sum_{i=1}^{N_0} \delta(z - d_{0i}) + \sum_{i=1}^{N_1} \delta(z - d_1) + \sum_{i=1}^{N_2} \delta(z - d_2) \right) \quad (4.4)$$

which can equivalently be written as

$$D(z) = \frac{N_0}{N} \left(\frac{1}{N_0} \sum_{i=1}^{N_0} \delta(z - d_{0i}) \right) + \frac{1}{N} \sum_{i=1}^{N_1} \delta(z - d_1) + \frac{1}{N} \sum_{i=1}^{N_2} \delta(z - d_2) \quad (4.5)$$

with N_0 , N_1 and N_2 the number of emitters in the layers 0, 1, and 2, respectively, and with $N = N_0 + N_1 + N_2$, the total number of emitters. It is also assumed that the zeroth-layer is buckled and thus the emitters within this layer have different heights d_{0i} , while the G -1st and G -2nd layers are assumed to be

perfectly flat, with unique values for the emitters (d_1 and d_2). Note that in this analysis the attenuation of the XPS signal from deeper layers is ignored. Taking the Fourier transform (Eq. 4.1) yields

$$\mathcal{D} = \frac{N_0}{N} F_{c,0}^{\mathbf{H}} e^{2\pi i P_{c,0}^{\mathbf{H}}} + \frac{N_1}{N} e^{2\pi i \frac{d_1}{d_{hkl}}} + \frac{N_2}{N} e^{2\pi i \frac{d_2}{d_{hkl}}}, \quad (4.6)$$

where $F_{c,0}^{\mathbf{H}}$ and $P_{c,0}^{\mathbf{H}}$ are coherent fraction and position of the zeroth-layer, which are known from a previous study [105].

Here, θ_n is defined as the coverage in layer n as the number of photoemitters in this layer relative to θ_0^{\max} , the maximal number of photoemitters in the zeroth-layer, i.e.,

$$\theta_n \equiv \frac{N_n}{N_0^{\max}} \in [0, \theta_n^{\max}] \text{ with } \theta_n^{\max} \equiv \frac{N_n^{\max}}{N_0^{\max}}, \quad (4.7)$$

where N_n^{\max} is the maximal number of photoemitters the layer n can have independently of its environment. Equivalently, one can write θ_n^{\max} in terms of the surface density of photoemitters \mathcal{N}_n/A_n in the completely "filled" crystalline structure of layer n where \mathcal{N}_n is the number of photoemitters per surface unit and A_n the surface unit area:

$$\theta_n^{\max} \equiv \frac{\mathcal{N}_n/A_n}{\mathcal{N}_0/A_0}. \quad (4.8)$$

From this definition, one can see that $\theta_0^{\max} = 1$ and obtain

$$\mathcal{D} = \frac{\theta_0 N_0^{\max}}{N} F_{c,0}^{\mathbf{H}} e^{2\pi i P_{c,0}^{\mathbf{H}}} + \frac{\theta_1 N_0^{\max}}{N} e^{2\pi i \frac{d_1}{d_{hkl}}} + \frac{\theta_2 N_0^{\max}}{N} e^{2\pi i \frac{d_2}{d_{hkl}}} \quad (4.9)$$

or

$$\mathcal{D} = \frac{\theta_0 F_{c,0}^{\mathbf{H}} e^{2\pi i P_{c,0}^{\mathbf{H}}} + \theta_1 e^{2\pi i \frac{d_1}{d_{hkl}}} + \theta_2 e^{2\pi i \frac{d_2}{d_{hkl}}}}{\theta_0 + \theta_1 + \theta_2}. \quad (4.10)$$

It is thus possible to decompose the measured signal \mathcal{D} on the left-hand side of Eq. 4.3, into a normalized vector sum of three vectors in the complex plane. Hereby, the orientation of each of the three summed vectors remains fixed, because the height of each layer is fixed. However, according to Eq. 4.10 the length of each summed vector is given by the coverage of the respective layer. Note that the vector for the zeroth-layer is additionally scaled by its coherent fraction $F_{c,0}^{\mathbf{H}}$. Also note that in Eq. 4.9 a common scaling factor N_0^{\max}/N remains unspecified. This means that, e.g., θ_1 and θ_2 can only be determined relative to θ_0 . For this reason, it is auspicious to write Eq. 4.10 in the form

$$\mathcal{D}_G = \frac{F_{c,0}^{\mathbf{H}} e^{2\pi i P_{c,0}^{\mathbf{H}}} + (\theta_1/\theta_0) e^{2\pi i \frac{d_1}{d_{hkl}}} + (\theta_2/\theta_0) e^{2\pi i \frac{d_2}{d_{hkl}}}}{1 + (\theta_1/\theta_0) + (\theta_2/\theta_0)} \quad (4.11)$$

for the graphene component in the C 1s core-level.

If one considers now the result of a NIXSW experiment, given by a measured coherent fraction $F_c^{\mathbf{H}}$ and position $P_c^{\mathbf{H}}$, represented by the point in the Argand diagram $\mathcal{D} = F_c^{\mathbf{H}} e^{2\pi i P_c^{\mathbf{H}}}$, we can decompose this result in the sum of three terms representing the contribution of the three layers:

$$\mathcal{D}_G = \frac{\mathcal{D}_0 + (\theta_1/\theta_0)\mathcal{D}_1 + (\theta_2/\theta_0)\mathcal{D}_2}{1 + \theta_1/\theta_0 + \theta_2/\theta_0} \quad (4.12)$$

where \mathcal{D}_i , ($i = 0, 1, 2$) are the Argand vectors representing the G -ZL, G -1st and G -2nd layers, respectively. And $\mathcal{D}_i = F_{c,i}^{\mathbf{H}} e^{2\pi i P_{c,i}^{\mathbf{H}}}$, with their individual coherent fractions $F_{c,i}^{\mathbf{H}}$ and positions $P_{c,i}^{\mathbf{H}}$. In order to solve this equation for θ_1 and θ_2 , \mathcal{D}_0 and \mathcal{D}_1 are assumed to be identical to the experimental results obtained for EMLG [105], and that \mathcal{D}_2 reflects the G -1st to G -2nd layer distance of 3.37Å, as found in Ref. [142], with $F_c^{\mathbf{H}} = 1.0$, same as for \mathcal{D}_1 .

In the inset of Fig. 4.6(c), the three vectors used in the sum, \mathcal{D}_0 , \mathcal{D}_1 , and \mathcal{D}_2 are indicated by large black full circles. These three vectors are necessary to form the additional axes θ_1/θ_0 and θ_2/θ_0 in Fig. 4.6(c). The fit result \mathcal{D}_G of the yield curve is displayed in the Argand diagram in terms of $(F_{c,G}^{\mathbf{H}}; P_{c,G}^{\mathbf{H}})$ and can be directly reread in terms of the additional axes $(\theta_1/\theta_0; \theta_2/\theta_0)$.

Therefore for each data point p , \mathcal{D}^p is a weighted sum of the known \mathcal{D}_0 , \mathcal{D}_1 and \mathcal{D}_2 vectors and is dependent only on the relative coverage pair $(\theta_1^p/\theta_0^p; \theta_2^p/\theta_0^p)$ while θ_0^p remains undetermined. In order to ease reading from the plot in Fig. 4.6(c), additional axes in terms of $(\theta_1/\theta_0; \theta_2/\theta_0)$ are drawn. For the specific system G -R30°/ZLG-R30° we have $\mathcal{N}_0 = \mathcal{N}_1 = 2$ and thus following Ref. [136] we obtain $\theta_1^{\max} = \frac{A_0}{A_1} = 1.0029 \pm 0.0017$. In other words, for NIXSW, the differences in photoemitters density between G -ZL, G -1st and G -2nd are negligible and one can set $\theta_1^{\max} \simeq \theta_2^{\max} \simeq \theta_0^{\max} = 1$. Moreover, the G -1st layer can only be present on top of the G -ZL, i.e., $\theta_0^p \in [0, 1]$, $\theta_1^p \in [0, \theta_0^p \leq \theta_0^{\max}]$, and $\theta_2^p \in [0, \theta_1^p \leq \theta_1^{\max}]$. For each experimental data point p , the corresponding coverage θ_n^p/θ_0^p for $n = 1, 2$ as defined in Eq. 4.7, can be read off directly in Fig. 4.6(c). The total coverage of all graphene overlayers Θ for data point p is decomposed:

$$\Theta^p \equiv \theta_0^p + \theta_1^p + \theta_2^p, \quad (4.13)$$

into partial coverages $\theta_0^p, \theta_1^p, \theta_2^p$ in the G -ZL, G -1st and G -2nd layers respectively, one obtains

$$\begin{aligned} \Theta^{T-G, \text{highT}} &= \theta_0^{T-G, \text{highT}} \left(1 + \frac{\theta_1^{T-G, \text{highT}}}{\theta_0^{T-G, \text{highT}}} + \frac{\theta_2^{T-G, \text{highT}}}{\theta_0^{T-G, \text{highT}}} \right) \\ &\simeq \theta_0^{T-G, \text{highT}} (1 + 0.7 + 0.6) = 2.3 \theta_0^{T-G, \text{highT}}, \end{aligned} \quad (4.14)$$

$$\Theta^{T-G, \text{lowT}} \simeq \theta_0^{T-G, \text{lowT}} (1 + 0.5 + 0.1) = 1.6 \theta_0^{T-G, \text{lowT}} \quad (4.15)$$

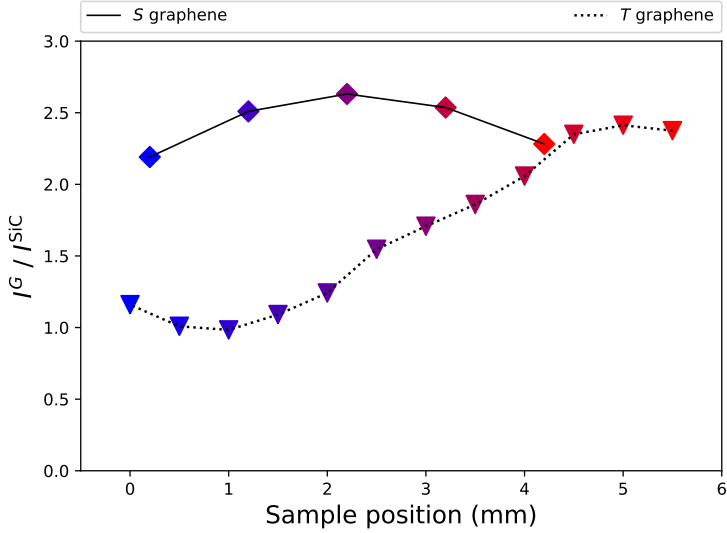


Figure 4.7: Intensity of the overlayer component G (G -ZL + G -1st + G -2nd) in Fig. 4.6(a) normalized to the SiC bulk component for different preparation temperatures. \diamond for S graphene and ∇ for T graphene, for the color code see Fig. 4.6.

and

$$\Theta^{S-G} \simeq \theta_0^{S-G}(1 + 0.9 + 0.1) = 2.0 \theta_0^{S-G}, \quad (4.16)$$

Finally, in order to enable the comparison to XPS data, it is further assumed that $\theta_0^{T-G, \text{highT}} \simeq \theta_0^{T-G, \text{lowT}} \simeq \theta_0^{S-G}$. From Eqs. 4.14, 4.15, 4.16, one thus recovers the relations

$$\Theta^{T-G, \text{highT}} > \Theta^{S-G} > \Theta^{T-G, \text{lowT}}. \quad (4.17)$$

In addition to the overall coverages, NIXSW also yields coverages of the various layers (Eqs. 4.14, 4.15, 4.16) relative to the coverage of G -ZL. The NIXSW analysis does not reveal θ_0^p . However, the fact that S graphene is stable in air, indicates that $\theta_0^p \simeq \theta^{\text{maxo}} = 1$ and that G -ZL is covering SiC nearly completely, thus protect it from oxidation in air. As a consequence, $\theta_1^{S-G}/\theta_0^{S-G} = 0.9 \pm 0.1$ means that also G -1st layer covers almost the complete sample.

Fig. 4.7 displays the integrated intensity of the graphene component (I^G : I^{S-G} for S graphene and I^{T-G} for T graphene), normalized by the bulk substrate component (I^{SiC}), of C 1s core-level measured off the Bragg energy as a

function of the preparation temperature (corresponding to the position along the sample, see Sec. 3.3). The symbols and the color code are identical to Fig. 4.6(c).

It is readily visible in Fig. 4.7 that I^{S-G}/I^{SiC} is much less changing with temperature than I^{T-G}/I^{SiC} . Moreover, for high temperatures, it is observed that

$$I^{T-G, \text{highT}}/I^{\text{SiC}} \simeq I^{S-G}/I^{\text{SiC}} \simeq 2.4, \quad (4.18)$$

while for low temperatures

$$I^{T-G, \text{lowT}}/I^{\text{SiC}} \simeq 1.2. \quad (4.19)$$

To a first approximation, one can expect I^G/I^{SiC} to be proportional to the total coverage Θ of all graphene overlayers, that is

$$I^G/I^{\text{SiC}} = c^{-1}\Theta, \quad (4.20)$$

with $c = \text{const.}$ Thus,

$$\Theta^{T-G, \text{highT}} \simeq \Theta^{S-G} \simeq 2.4c \quad (4.21)$$

and

$$\Theta^{T-G, \text{lowT}} \simeq 1.2c, \quad (4.22)$$

leading to the conclusion

$$\Theta^{S-G} \simeq \Theta^{T-G, \text{highT}} > \Theta^{T-G, \text{lowT}}, \quad (4.23)$$

which is at least partly in agreement with Eq. 4.17.

In agreement with ARPES results, it is found that T graphene is very inhomogeneous with $\theta_1^{T-G}/\theta_0^{T-G} = 0.6 \pm 0.1$ and $\theta_2^{T-G}/\theta_0^{T-G}$ varying from

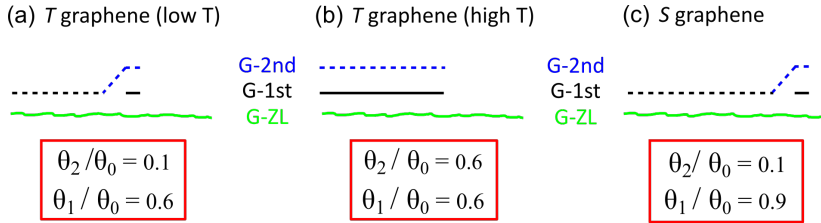


Figure 4.8: Coverage model for T graphene. Coverages relative to the ZLG- $R30^\circ$ in the red boxes are results from the NIXSW analysis. Suggested graphene orientations are indicated by dashed ($R0^\circ$) and solid ($R30^\circ$) lines, see text for detailed discussion.

0.1 to 0.6 depending on the preparation temperature. It shows that about 40% of the G -ZL remains always uncovered on the T graphene sample, see Fig. 4.8. With increasing preparation temperature, $\theta_2^{T-G}/\theta_0^{T-G}$ increases with the concomitant appearance of a π band at \bar{K}_{30° in ARPES, see Fig. 4.5(b). In contrast, S graphene is much more homogeneous with $\theta_1^{S-G}/\theta_0^{S-G} = 0.9 \pm 0.1$ and $\theta_2^{S-G}/\theta_0^{S-G} = 0.1 \pm 0.1$, independent of the preparation temperature. This means that almost only G - $R0^\circ$ is present on top of ZLG - $R30^\circ$ and that both have essentially the same coverage, while G - $R30^\circ$ is almost absent. In conclusion, S graphene is composed of a highly homogeneous G - $R0^\circ$ / ZLG - $R30^\circ$ stack, almost fully covering SiC(0001). Therefore, it constitutes an ideal platform to study 30° -tBLG with different doping levels, as well as different interaction strengths to the substrate, by choosing the atomic species used for intercalation.

As depicted in Fig. 4.8, G -2nd exist only on top of G -1st. Even though there is no direct evidence to link the orientations to the heights of graphene layers, it is believed that G - $R30^\circ$ only grows underneath G - $R0^\circ$ because of two facts: (1) The borazine-mediated SiC surface produces G - $R0^\circ$ at a preparation temperature of about 1300°C . (2) With even higher preparation temperature, graphene multi-layers with $R30^\circ$ orientation form epitaxially on the SiC substrate [37]. Therefore, it is reasonable to have the assumption that after the borazine-mediated SiC surface is used up for G - $R0^\circ$ growth, G - $R30^\circ$ grows from excessive carbon atoms from the substrate (more precisely ZLG - $R30^\circ$) and adopts the $(6\sqrt{3} \times 6\sqrt{3})$ - $R30^\circ$ lattice orientation.

4.4 Conclusion

In this chapter, the differences between T graphene and S graphene in terms of lateral, and vertical structures as well as electronic properties were compared. With high-resolution LEED, the origins of the diffraction spots measured were discussed in detail. S graphene showed higher layer quality and larger grain size than T graphene from qualitative comparison. Quantitative spot profile analysis of the S graphene showed that the G - $R0^\circ$ has a smaller domain size than the averaged SiC terrace width and has an azimuthal disorientation of $\sigma = 0.458^\circ$ around the 0° direction of SiC lattice. ARPES measurement showed that there was G - $R30^\circ$ present on T graphene, which is in agreement with the high-resolution LEED measurement. On the other hand, S graphene showed no sign of G - $R30^\circ$ and therefore can serve as a platform for 30° -tBLG preparation. With NIXSW, coverages of G -1st and G -2nd could be determined relative to the G -ZL layer under some assumptions. The relative coverages are in agreement with the XPS intensity ratio of the graphene component to the SiC bulk component.

Finally, I briefly comment on the growth mechanism of graphene on SiC in a borazine atmosphere leading to the unconventional orientation of 0° . Because of the high temperature at around 1300°C , B_xN_y - $R0^\circ$ does not stabilize despite the presence of borazine. Yet, due to the presence of the surfactant borazine molecule, the graphene layer that grows at this temperature is forced to adopt the lattice orientation of B_xN_y - $R0^\circ$. The layer underneath $\text{G-}R0^\circ$ has not been exposed to borazine atmosphere, and therefore $\text{ZLG-}R30^\circ$ keeps the $R30^\circ$ orientation. At preparation temperature higher than 1300°C , $\text{G-}R30^\circ$ grows from excessive carbon atoms underneath $\text{G-}R0^\circ$. For S graphene, the growth of $\text{G-}R0^\circ$ is a self-limiting process. This new preparation method, in which the borazine enables epitaxial growth of a graphene layer in an unconventional 0° orientation, can foster a new way to produce large-scale tBLG and bring its intriguing properties closer to applications.

Chapter 5

Sb-intercalated freestanding monolayer graphene

Following the epitaxial-graphene-related studies in the previous two chapters, this chapter focuses on the intercalation of antimony into ZLG- $R30^\circ$ and the layer property of the quasi-freestanding graphene obtained. As discussed in chapter 3 and 4, it is known that SiC decomposes at temperatures above 1200°C , at which the volatile silicon atoms sublime whereas the carbon atoms arrange in a $(6\sqrt{3} \times 6\sqrt{3})$ - $R30^\circ$ superstructure with respect to the SiC substrate [144, 145]. This carbon layer, which is denoted as the zeroth-layer graphene (ZLG- $R30^\circ$) in this work, is strongly coupled to the SiC substrate and lacks typical π -bands of graphene [146, 147] while exhibiting the same lateral structure as epitaxial monolayer graphene (EMLG). At even higher preparation temperature ($> 1250^\circ\text{C}$), the ZLG- $R30^\circ$ transforms into graphene, as indicated by the appearance of its characteristic electronic band structure, since a new ZLG- $R30^\circ$ is formed underneath, which decouples the first one from the substrate [144, 145]. In this way, one can rather easily prepare EMLG and even stacked graphene multilayer. However, the decoupling is not complete, the ZLG- $R30^\circ$ influences the electronic properties of the graphene layers on top, resulting in n-type doping with a Dirac point energy E_D of 450 meV [148] and undesirable temperature dependence of the carrier mobility [149].

An elegant way to avoid the influence of the ZLG on the electronic properties of the graphene layers is to decouple it from the SiC substrate by intercalation. Thereby, a certain element (intercalant) is brought between the SiC(0001) surface and the ZLG- $R30^\circ$, which decouples the latter from the substrate and transforms it into so-called quasi-freestanding monolayer graphene (QFMLG).

A prominent example is the intercalation of hydrogen [41, 44], which produces QFMLG on an H-saturated SiC(0001) surface. Such a QFMLG shows lit-

tle temperature dependency in charge carrier mobility [149] and excess of holes due to the spontaneous polarization of the hexagonal SiC substrate [150–152]. Several other elements have been used to intercalate ZLG- $R30^\circ$ [54]. Depending on the type of intercalant and its amount, it is possible to induce interesting electronic properties of QFMLG. For example, ambipolar doping was observed for germanium intercalation [43], where the charge carrier type depends on the amount of intercalated Ge. This effect can also be seen for gold intercalation [48]. Another example is lithium- or calcium-doped graphene showing superconductivity [153]. For bismuth intercalated graphene, depending on the amount of the intercalated material, two phases of different crystalline and electronic structures can be distinguished [154].

Recently a new method for intercalation of solid elements with high vapor pressure was reported [49]. In this process, intercalation under the ZLG- $R30^\circ$ was achieved by annealing the Sb-covered SiC(0001) sample in Ar at atmospheric pressure [49]. X-ray photoelectron spectroscopy (XPS) verified the decoupling of the ZLG- $R30^\circ$ and the formation of a QFMLG [49]. Sb 3*d* core-level spectra indicated a layer of metallic Sb at the interface between SiC(0001) and QFMLG. The reported changes in the low-energy electron diffraction (LEED) pattern in Ref. [49], namely a strong reduction of the Moiré spots associated with the ZLG- $R30^\circ$, supported the decoupling observed in XPS. This is typical for ZLG- $R30^\circ$ intercalation on SiC and was observed, for instance, for H [41], Au [48], Ge [43], Si [155], Cu [52], and Yb [156] intercalants. Using angle-resolved photoelectron spectroscopy (ARPES) it was shown that QFMLG formed in this way is n-doped [49]. However, no information about the vertical structure of this system has been reported so far, such as the thickness of the Sb layer or its vertical distances to the graphene layer and to the substrate, despite such information would be highly relevant, since the layer distance is a good indicator of interaction strength [105, 157–161].

LEED also revealed clear signatures of the intercalation, i.e., a strong reduction of the Moiré spots associated with the ZLG- $R30^\circ$. Besides diffraction spots arising from graphene and SiC(0001), only very weak spots from multiple electron scattering were observed, which suggests an efficient decoupling. The thickness of the intercalated layer can affect the electronic properties and the possible application of the system, as in the case of two-dimensional Ag layers on epitaxial graphene [54]. In this chapter, the success and homogeneity of the Sb decoupling are unambiguously confirmed using LEED and normal incidence x-ray standing wave (NIXSW). The latter also reveals the vertical structure of QFMLG, which is intercalated by metallic Sb, with a precision better than $\pm 0.2 \text{ \AA}$.

Please note that this project was a collaboration with the group of Prof. Thomas Seyller, TU Chemnitz. Susanne Wolff intercalated the samples and

carried out LEED and ARPES measurements at TU Chemnitz. The NIXSW experiments were performed by a team of experimentalists from PGI-3 (including myself), and with the help of Dr. Tien-Lin Lee at the Diamond Light Source, Didcot, UK. The data analysis and interpretation, however, were part of my PhD project. The content of this chapter is published [162].

5.1 Sample preparation

Nitrogen-doped 6H-SiC(0001) wafers purchased from SiCrystal GmbH, Germany were used for sample preparation. Prior to the graphitization process, the SiC substrate was etched in a hydrogen atmosphere [163]. The ensuing ZLG- $R30^\circ$ growth process was performed in a furnace in an Ar atmosphere at a pressure of 1000 mbar and an Ar flow rate of 0.1 slm. By annealing the substrate at a temperature of 1475°C for 15 min, a ZLG- $R30^\circ$ sample was obtained as described in Ref. [163]. The deposition of 50 nm Sb on top of the ZLG- $R30^\circ$ sample was carried out in a separate system by molecular beam epitaxy using a calibrated Sb Knudsen cell [49]. During the deposition process, the pressure was maintained at or below 1×10^{-9} mbar.

Since annealing in UHV leads to desorption of Sb before intercalation, it was necessary to intercalate the Sb-covered sample *ex-situ* by annealing the Sb covered ZLG- $R30^\circ$ sample in Ar atmosphere at a pressure of 1000 mbar and a flow rate of 0.1 slm [49]. The furnace was identical to that used for ZLG- $R30^\circ$ growth [163]. A consecutive two-step annealing at 400°C for 30 min and at 550°C for 60 min was used to intercalate Sb and obtain QFMLG [49]. Note that most of the Sb deposited on top of the ZLG- $R30^\circ$ desorb from the surface during this process. Only a minor part of the Sb intercalates at the interface between SiC and QFMLG.

After intercalation, and again after transport of the samples to the synchrotron, LEED and ARPES (He I) measurements were performed to confirm the quality of the QFMLG. In all cases, the obtained data were of comparable quality as those shown in Fig. 4(a) and Fig. 5(b) of Ref. [49].

5.2 NIXSW Experiment

Core-levels spectra and NIXSW data for all relevant species: Sb, C, and Si, for Sb-intercalated QFMLG are recorded. In the data analysis, an important first step is the identification of all relevant components in the spectra. In the Sb 3d data, beside the $3d_{5/2}$ and $3d_{3/2}$ doublet (peaks at 527.8 eV and 536.5 eV, respectively, see the orange curve in Fig. 5.1), we find an additional small signal at 532.5 eV that we attribute to oxygen. One might suspect that this

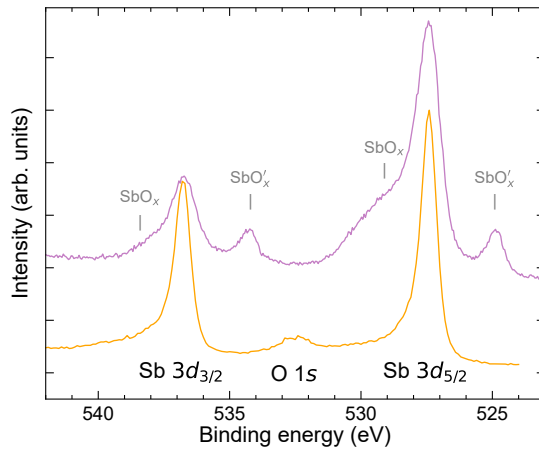


Figure 5.1: Sb 3d core-level spectra. Orange line: Sb-intercalated quasi-freestanding graphene on SiC(0001) (photon energy of 2458 eV). Magenta line (adapted from Ref. [49]): ZLG- $R30^\circ$ sample with incomplete Sb intercalation (photon energy of 700 eV). Two oxidized Sb species are marked.

little amount of oxygen is located in the Sb intercalation layer forming SbO_x . However, in such a case, a doublet of (chemically shifted) Sb $3d$ peaks should be present [49], as it is visible in the magenta spectrum in Fig. 5.1 recorded on an oxidized sample with incomplete Sb intercalation. In our spectrum, such a chemically shifted doublet is not present, which lets us conclude that no significant amount of SbO_x is formed on Sb-intercalated QFMLG. Therefore the oxygen peak in our spectrum originates most likely from residual oxygen at step edges where the ZLG- $R30^\circ$ or QFMLG do not offer perfect protection against the oxidization of the SiC substrate, thus not affecting the conclusions about the predominant graphene-covered areas.

For the NIXSW data analysis, only the Sb $3d_{3/2}$ is used, since the O $1s$ peak is sufficiently far away at the lower binding energy side. Typical spectra for all core-levels (recorded using hard x-rays) are shown in Fig. 5.2(a-c). In the C $1s$ spectrum, we see two well-separated peaks stemming from QFMLG and bulk SiC. Asymmetric Lorentzian functions were used to fit all core-levels after subtraction of a linear background. The full width at half maximum values of the best fits are 0.46 eV for the C_{Gr} component, 0.56 eV for C_{SiC} , 0.62 eV for Sb $3d_{3/2}$ and 1.21 eV for Si $2s$.

The resulting photoelectron yield curves are shown in Fig. 5.2(d). Fits were performed using the software package TORRICELLI [82, 164], under consideration of non-dipolar effects in the photoemission process and a small (unavoidable) deviation from normal incidence ($\theta = 86.5^\circ$ in our case) [81]. Note that a proper correction of non-dipolar effects can only be performed for photoemission from an s -state [79, 165]. Hence, for Sb $3d$ the data are uncorrected, but the correct polarization factor (differing from unity due to $\theta \neq 90^\circ$) was considered. For more details on these corrections and on the treatment of the experimental uncertainties see Ref. [81, 82].

Note that several such yield curves were measured for C $1s$, Sb $3d_{3/2}$, and Si $2s$ core-levels on different positions on the sample surface, whereby the homogeneity of the sample was verified by XPS. The averaged results from these multiple scans are listed in Table 5.1. It is remarkable that the intercalated Sb layer shows a very high coherent fraction of 1.09(2), comparable with the values obtained for the bulk species C_{SiC} and Si_{SiC} . The nonphysically high value (above 1.0) is most likely due to non-dipolar effects that cannot be corrected for d -shell emission [81], and due to a known non-linearity of the electron analyzer for high photoelectron count rates (still below the saturation threshold) [166]. In either case, the coherent positions P_c^{H} are not affected, and the high coherent fraction F_c^{H} does indicate a high vertical order of the Sb atoms. In other words, a very flat Sb layer is formed by the intercalation process, thus excluding the formation of a Sb multilayer. This is in agreement with the fact that we do not see any shifted component in the Sb $3d$ spectra

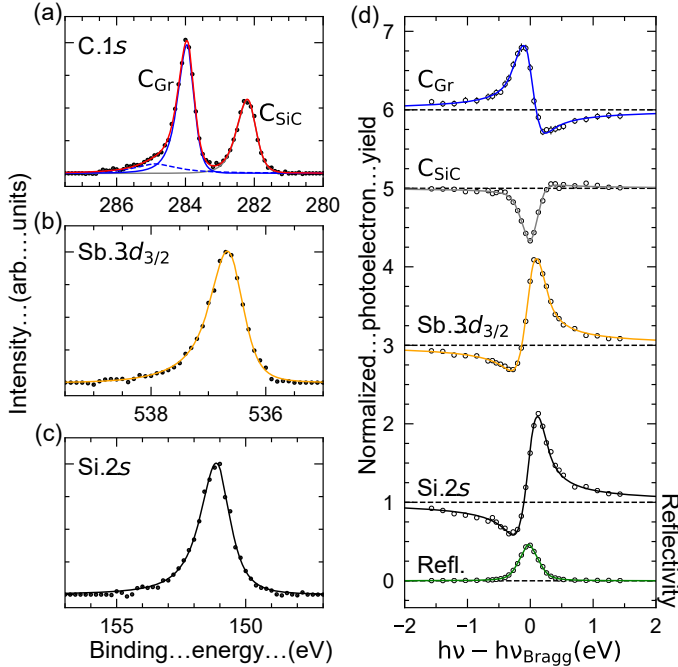


Figure 5.2: (a)-(c) C 1s, Sb 3d_{3/2}, and Si 2s core-level spectra recorded on Sb-intercalated quasi-freestanding graphene on SiC(0001) at a photon energy of 2465 eV, that is 4 eV below the SiC(0006) Bragg energy. A linear background was subtracted. (d) Corresponding NIXSW yield curves and a typical reflectivity of the SiC(0006) reflection. The curves for C_{Gr}, C_{SiC} and Sb 3d_{3/2} are vertically displaced by 5, 4 and 2, respectively.

which would indicate Sb is located in different chemical environments.

The graphene layer exhibits a much smaller F_c^{H} of 0.71(7). It should be mentioned that for hydrogen intercalated graphene a very similar value of F_c^{H} = 0.68 has been found [161]. Therefore, it's straightforward that the coherent position P_c^{H} obtained from the C_G component gives the adsorption height of the graphene layer above the Sb intercalation layer. A structure model based on the obtained coherent positions P_c^{H} is displayed in Fig. 5.3(b). It shows the intercalation layer at a height of $z_{\text{Sb}} = 2.58(2)$ Å above the topmost Si atomic plane, in other words, in a distance very close to the sum of the covalent radii of Si (1.16 Å) and Sb (1.40 Å) [167] and in good agreement with the Sb-Si bond length observed in tetrakis(trimethylsilyl)distibane (2.594 Å) [168].

Table 5.1: Average results of all individual NIXSW scans on Sb-intercalated quasi-freestanding graphene on SiC(0001). Parameters used in the fitting: Bragg angle $\theta = 86.5^\circ$, electron emission angle relative to the incident synchrotron beam $\phi = 80.9^\circ$, non-dipolar correction factors $\gamma_{\text{C1s}} = 1.022$, $\Delta_{\text{C1s}} = -0.218$, $\gamma_{\text{Si2s}} = 0.707$, and $\Delta_{\text{Si2s}} = 2.645$, for details see Ref. [81,164]. n is the number of lattice planes to the surface.

	P_c	F_c	n	z (Å)
C _{Gr} 1s	0.47(1)	0.71(7)	2	6.19(2)
Sb 3d _{3/2}	0.03(1)	1.09(2)	1	2.58(2)
Si _{SiC} 2s	0.01(1)	1.12(2)	0	0.00
C _{SiC} 1s	0.76(1)	1.02(2)	-1	-0.63(2)

This measured distance corresponds to only $\approx 62\%$ of the typical van der Waals bonding distance between these two species (4.16 Å) [169], and clearly indicates the chemical interaction between the Sb layer and the SiC substrate. It also suggests that all Sb atoms are located at on-top sites of the uppermost Si atoms (no Sb atoms at other sites), as indicated in Fig. 5.3(b). Given the covalent Si-Sb bonding distance, a position on a 3-fold hollow site of the SiC substrate would result in a smaller height for Sb of ≈ 2.28 Å.

The tentative conclusion that all Sb atoms are occupying on-top sites of the uppermost Si atoms of the SiC(0001) surface, saturating their dangling bonds, is consistent with the fact that LEED shows no indications of any surface reconstruction, but the (1×1) surface unit mesh of the Sb-terminated SiC surface (only diffraction spots of graphene and the substrate are visible [49]). It is furthermore supported by DFT calculations by Hsu *et al.* [170], showing the Sb intercalant to be stable at on-top sites of the SiC(0001) substrate. A similar scenario, Sb saturating the dangling bonds of the top Si atoms, is found for a monolayer Sb on Si(111). Although the surface is $(\sqrt{3} \times \sqrt{3})$ - $R30^\circ$ reconstructed in this case, the bonding distance between Sb and Si is similar (2.74 Å [171]) to what was observed in this chapter.

The distance between the graphene layer and the Sb intercalation-layer is much larger, 3.62(4) Å. This value corresponds to about 96% of the van der Waals bonding distance (3.76 Å [169]) and is clearly higher than the expected covalent bonding distance (2.16 Å [167]). In very good agreement with our observation, DFT calculations by Hsu *et al.* [170] predicted a Sb-QFMLG distance of 3.659 Å. Hence, one can conclude that the Sb intercalation layer decouples the QFMLG electronically well from the substrate. The observation of a sharp and well-visible Dirac cone [49] supports this finding of a mere van der Waals-like interaction between the atomic species of the QFMLG and the Sb intercalation layer.

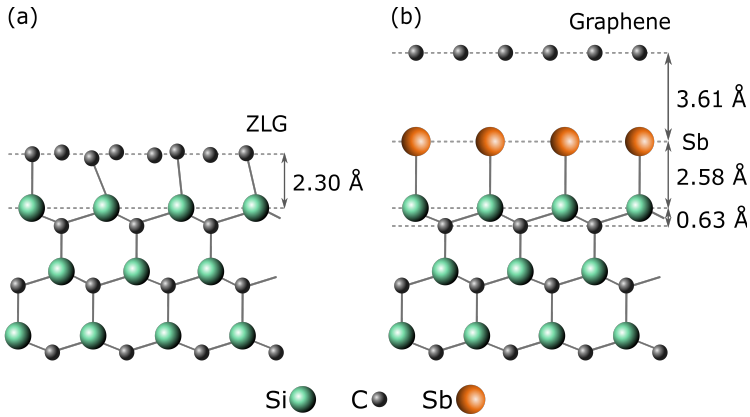


Figure 5.3: Ball-and-stick models of the vertical structure of (a) ZLG- $R30^\circ$ before intercalation, from Ref. [105], and (b) of Sb-intercalated quasi-freestanding graphene on SiC(0001)

5.3 Conclusion

Using a combination of LEED, XPS and NIXSW, the vertical structure of QFMLG, which was obtained by intercalating ZLG- $R30^\circ$ on 6H-SiC(0001) with Sb has been determined. Homogeneity and intercalation quality were checked by XPS. The vertical structure consists of a flat single layer of Sb, covalently bound to the top Si atoms of the substrate. Multiple Sb layers can clearly be excluded. The measured layer distance of 2.58 Å and the (1×1) LEED pattern suggest an on-top position of Sb above the topmost Si atoms.

The QFMLG layer above the Sb intercalation layer is located much further away, 3.61 Å above Sb. This indicates van der Waals bonding only between these layers, and hence a very good decoupling of the QFMLG. The structural parameters obtained from our study are in very good agreement with the theoretical prediction by Hsu *et al.* [170].

Chapter 6

Sr-doped and pristine bismuth selenide

The discovery of topological superconductivity in doped Bi_2Se_3 made this class of materials highly important for the field of condensed matter physics. However, the structural origin of the superconducting state remained elusive, despite being investigated intensively in recent years. Scanning tunneling microscopy and the normal incidence x-ray standing wave (NIXSW) technique were applied in order to determine the vertical position of the dopants – one of the key parameters for understanding topological superconductivity in this material – for the case of $\text{Sr}_x\text{Bi}_2\text{Se}_3$. In a novel approach, the NIXSW data was analyzed in consideration of the inelastic mean free path of the photoemitted electrons, which allows one to distinguish between symmetry equivalent sites. The Sr atoms were found not situating inside the van der Waals gap between the Bi_2Se_3 quintuple layers but rather *in* the quintuple layer close to the outer Se planes.

Note that the content in this chapter is published in Ref. [172]. It is a collaboration with the group of Prof. Yoichi Ando, University of Cologne. The samples measured in this chapter are prepared by Mahasweta Bagchi, who also studied them using a superconducting quantum interference device (SQUID). Supplementary STM experiments (not shown in this thesis) were performed and analyzed by Mahasweta Bagchi and Dr. Jens Brede. The NIXSW experiments were performed and analyzed by a team of experimentalists (including myself) at Diamond Light Source, Didcot, UK.

6.1 Introduction

Shortly after the discovery of superconductivity in Cu-doped Bi_2Se_3 crystals [55], Fu and Berg [173] proposed that any electron-doped Bi_2Se_3 is indeed a

viable candidate for hosting topological superconductivity with spin-triplet-like pairing. The spin-triplet-like nature of the pairing was successively confirmed by temperature-dependent nuclear magnetic resonance Knight shift (K_S) experiments [174] which found no change in K_S below T_c for magnetic fields applied parallel to the c -direction. Moreover, the same experiments found that the threefold symmetric Bi_2Se_3 lattice showed a two-fold anisotropy of K_S when the magnetic field was rotated in the a - b plane. Such a two-fold symmetry was successively also observed in scanning tunneling microscopy (STM) [175], specific heat [176], or high-resolution x-ray diffraction (XRD) experiments [177]. Theoretically, this breaking of the rotational symmetry in doped Bi_2Se_3 due to an anisotropy of the superconducting gap amplitude is only compatible with nematic superconductivity [178]. In the case of doped Bi_2Se_3 superconductors, the nematic superconducting state corresponds to the gap function with E_u symmetry, which is topological due to its odd parity [179]. Intriguingly, while this topological superconducting state has odd parity and is unconventional, it is still protected from the disorder due to the generalized Anderson's theorem [180]. Since the superconducting state of this material class has been extensively characterized, it is surprising that the structural characterization of the dopant location remains comparatively poor.

Theoretical studies based on density functional theory (DFT) show that doping by Cu [56] and Sr [57] atoms between Bi_2Se_3 quintuple layers is energetically most favorable. However, no direct experimental observations of dopants in the van der Waals (vdW) gap have been reported to date. An expansion of the c -axis in $\text{Sr}_x\text{Bi}_2\text{Se}_3$ [58, 181] as well as in $\text{Cu}_x\text{Bi}_2\text{Se}_3$ [59–61] was observed with XRD and was interpreted as a piece of evidence for dopant atoms inside the vdW gap. However, neutron-scattering experiments (in the case of $\text{Cu}_x\text{Bi}_2\text{Se}_3$ [61]) and transmission electron microscopy (TEM) studies (in the case of $\text{Sr}_x\text{Bi}_2\text{Se}_3$ [57]) did not observe dopants inside the vdW gap for superconducting single crystals. In the case of TEM, it was suggested that lateral movement of the dopants (due to the low diffusion barrier [56]) inside the vdW gap at room temperature precludes an observation [57]. However, a recent TEM study of native defects in Bi_2Se_3 demonstrated that Bi atoms inside the vdW gap can be observed [62].

STM data of Cu-doped Bi_2Se_3 thin-films grown by molecular beam epitaxy showed Cu atoms inside the quintuple layer, but no direct evidence of Cu inside the vdW gap [56]. It was suggested that STM is not sensitive to Cu atoms inside the vdW gap, however, a recent study of native defects in Bi_2Se_3 by Dai *et al.* [63] indicated that Se atoms inside the vdW gap can be resolved. Interestingly, Cu-doped (as well as more recently studied Sr-doped [64]) Bi_2Se_3 thin films grown under UHV conditions have carrier concentrations similar to those of bulk single crystals [56, 59, 64] but do not show superconductivity. The

absence of superconductivity in these films strongly suggests that contrary to what was originally proposed [55], the role of the dopants in inducing superconductivity in these materials goes beyond simple electron donation into the Bi_2Se_3 lattice. In this context, it is important to note that Cu- (or Sr-) doped Bi_2Se_3 single crystals only exhibit superconductivity reproducibly when carefully tuned heating and rapid cooling/quenching are employed [58, 60]. This indicates that a significant amount of dopants in the superconducting single crystals are trapped in metastable sites (likely not the energetically most favorable sites according to DFT) and that these dopants are indeed responsible for inducing superconductivity [58, 60]. Thus, deepening the understanding of superconductivity in doped Bi_2Se_3 requires advanced structure characterization in order to elucidate the intricate role played by the dopant.

The general goal of this project is to identify the (vertical) positions of the Sr-dopants in the $\text{Sr}_x\text{Bi}_2\text{Se}_3$ crystal, since these are of utmost importance for understanding the superconductivity of this material. Motivated by previous STM studies on near-surface defects in Bi_2Se_3 [63, 182] and by findings of the Ando group, NIXSW measurements on Bi_2Se_3 and $\text{Sr}_x\text{Bi}_2\text{Se}_3$ were performed. In contrast to the local technique STM, this method integrates over a macroscopic, sub-millimeter-sized surface area. This method turned out to be ideally suited for this problem and allowed unambiguous identification of the dominant vertical position of the dopant species.

6.2 Sample preparation

Sample preparation and characterization using STM took place in Cologne. Single crystals of $\text{Sr}_x\text{Bi}_2\text{Se}_3$ (nominal $x = 0.06$) were grown from high-purity elemental Sr chunk (99.99%), Bi shots (99.9999%), and Se shots (99.9999%) by a conventional melt-growth method. The raw materials with a total weight of 4.0 g were mixed and sealed in an evacuated quartz tube. The tube was heated to 850°C for 48 h. It was then slowly cooled from 850°C to 600°C within 80 h and finally quenched into water at room temperature.

Single crystals of Bi_2Se_3 were grown by melting stoichiometric amounts of Bi and Se shots (99.9999%) in a sealed evacuated quartz tube by the modified Bridgman method. The tube was heated to 850°C for 48 h with intermittent shaking to ensure the homogeneity of the melt, followed by cooling to 550°C in 100 h. It was then quickly cooled down to room temperature in 2 h. The $\text{Sr}_x\text{Bi}_2\text{Se}_3$ sample was found to be superconducting with a transition temperature of $T_c = 2.7$ K. Its superconducting shielding fraction of 76% was estimated from its magnetic moment at $T = 1.78$ K, after zero-field cooling.

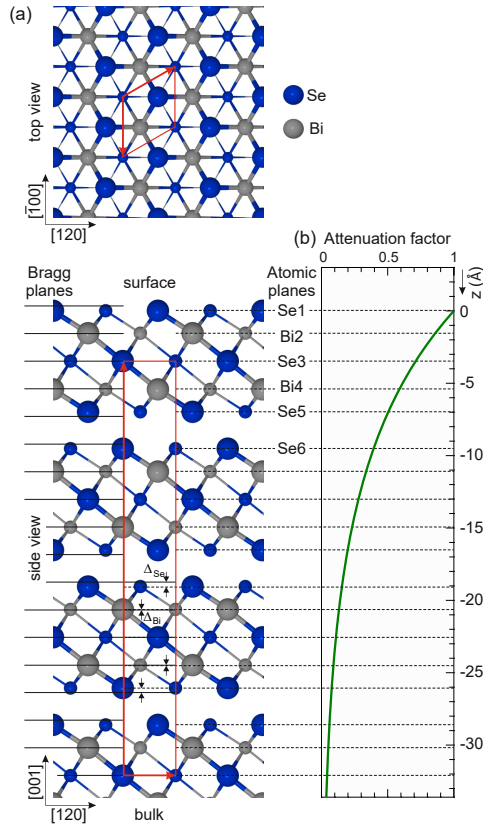


Figure 6.1: (a) Ball-and-stick model of the Bi_2Se_3 bulk crystal, shown as top view along the $[00\bar{1}]$ -direction (upper part) and side view along $[\bar{1}00]$ (lower part). The sizes of balls and sticks are linearly scaled with the distance of the atoms to the front plane (in the top view that is the crystal surface, in the side view it is the plane spanned by $[120]$ and $[001]$ corresponding to the lower edge of the top view). The unit cell (in the side view its projection) is indicated by the red parallelogram and rectangle. In the side view, also the z -positions of the atomic planes (right part, dashed lines extending into (b)) and the $(0\ 0\ 0\ 15)$ Bragg planes (left part, solid lines) are indicated. (b) Attenuation factor for the yield of a photoemission process occurring in the depth z , according to continuous exponential damping with an inelastic mean free path of $\lambda = 65 \text{ \AA}$, as obtained from fitting the NIXSW data, and an emission angle with respect to the surface normal of $\phi = 80.9^\circ$.

6.3 Vertical structure revealed by NIXSW

6.3.1 Structure model

The structure model that was used for analyzing this data is shown in Fig. 6.1. Panel (a) shows the Bi_2Se_3 crystal structure in the top-view (upper part) and side-view (lower part). The top view contains the atoms of the uppermost three atomic layers only, drawn as blue (Se) and gray (Bi) balls, the size of which indicates the depth below the surface. In the side view, the crystal terminated by a complete quintuple layer (QL, atomic layers from Se1 to Se5) is shown. The hexagonal unit cell is indicated by red lines and contains three QLs, i.e., 15 atomic planes. The vertical (z) positions of the atomic planes are marked as dashed lines in the right half of the figure (extending into Fig. 6.1 (b)). For NIXSW, the $H = (0\ 0\ 15)$ Bragg reflection ($(hkl) = (0\ 0\ 0\ 15)$ in hexagonal notation) was used, and thus, 15 Bragg planes can be found within the unit cell. They are equidistantly spaced by $1.908\ \text{\AA}$ in z , in contrast to the atomic planes. Therefore, while the central Se layer of each QL (Se3, Se8, ...) lies precisely on a Bragg plane, all other atomic planes lie close to but not on the Bragg planes, as indicated by the small gaps labeled Δ_{Se} and Δ_{Bi} in the side view of Fig. 6.1 (a). This will be important for the interpretation of the NIXSW data (see below).

6.3.2 NIXSW data

NIXSW data sets for an undoped and a Sr-doped Bi_2Se_3 sample were recorded. Bi $5d$, Se $3s$ and (in case of the doped sample) Sr $3d$ core-level spectra have been recorded in a $\pm 3\ \text{eV}$ interval around the Bragg energy $h\nu_{\text{Bragg}} = 3256\ \text{eV}$ of the $(0\ 0\ 0\ 15)$ Bragg reflection, and the partial photoelectron yield was extracted for all species as a function of the photon energy. The spectra were fitted with CASAXPS [141] using one asymmetric Voigt peak for Se $3s$ and Bi $5d_{5/2}$, and two symmetric Voigt peaks for the Sr $3d$ doublet with their relative intensity constrained to a ratio of 2:3. Exemplar spectra and fit curves (for $\text{Sr}_x\text{Bi}_2\text{Se}_3$ only) are shown in Fig. 6.2(a)-(c). These simple fitting models were sufficient since no indications for multiple components in different chemical environments were detected in XPS, neither with the hard x-ray beam nor using the soft x-ray beam that allows for a higher resolution. The latter data are shown in Fig. 6.3 and demonstrate that no significant spectroscopic differences were detected between the Bi_2Se_3 and the $\text{Sr}_x\text{Bi}_2\text{Se}_3$ samples. This indicates that – as expected from the small dopant concentration – the dopants do not cause any spectroscopically relevant change to the chemical environment of the bulk species. Taking into account the photoemission cross-sections at the x-ray energies used, the relative intensities of the Sr, Bi, and Se PES peaks are in

Table 6.1: NIXSW results of Bi_2Se_3 and $\text{Sr}_x\text{Bi}_2\text{Se}_3$, as averaged from all individual NIXSW scans. The data are corrected for non-dipolar effects and a deviation from normal incidence geometry ($2\theta < 180^\circ$) [81, 183].

	Bi_2Se_3		$\text{Sr}_x\text{Bi}_2\text{Se}_3$	
	P_c^{H}	F_c^{H}	P_c^{H}	F_c^{H}
Bi $5d_{5/2}$	0.98(2)	0.89(1)	0.95(2)	0.74(2)
Se $3s$	0.96(2)	0.71(1)	0.91(2)	0.64(1)
Sr $3d$	–	–	0.86(2)	0.49(7)

qualitative agreement with the expected stoichiometry of $\text{Sr}_x\text{Bi}_2\text{Se}_3$.

Typical partial yield curves, together with the x-ray reflectivity, are shown in Fig. 6.2(d), again only for the $\text{Sr}_x\text{Bi}_2\text{Se}_3$ data set. The yield curves were fitted using the dedicated NIXSW analysis software TORRICELLI [82, 164], which is able to consider non-dipolar effects in the photoemission process as well as a finite deviation from the ideal normal incidence geometry that cannot be avoided in the experiment [81, 183]. All final results (after averaging up to 7 equivalent measurements) are listed in Table 6.1. Despite the statistics of the Sr yield curve being apparently poor, obviously caused by the small density of Sr atoms in the crystal, the Sr data actually imposes a sufficient constraint on the fitting for reliably extracting values for the Sr coherent position P_c^{H} and coherent fraction F_c^{H} .

Note that the experimentally obtained P_c^{H} for all species of both samples Bi_2Se_3 and $\text{Sr}_x\text{Bi}_2\text{Se}_3$ are not zero. For Se and Bi, this is remarkable since the symmetry of the layer structure of the QLs (and the entire unit cell) should actually cancel out any effect that causes a finite P_c^{H} , as discussed in detail in the following section.

6.3.3 The effect of a finite inelastic mean free path

Commonly, the NIXSW technique is used as a method to determine the height of specific atomic species above a surface, which is very useful to evaluate, e.g., the interaction of adsorbates (atoms or molecules) with the surface or with other adsorbates on the surface [79, 97, 184–193]. In such experiments, NIXSW data of the bulk species are often also recorded, in order to monitor the surface quality or simply for reasons of completeness. For crystals with a mono-atomic primitive unit cell, the structural parameters obtained by NIXSW for the bulk species are very close to $P_c^{\text{H}}=0.0$ and $F_c^{\text{H}}=1.0$ in many cases, indicating that the atoms are located on Bragg planes (which is the case per definition) and that the crystal is well ordered. But in multinary crystals both F_c^{H} and P_c^{H} may vary from these values, depending on the number of inequivalent layers of

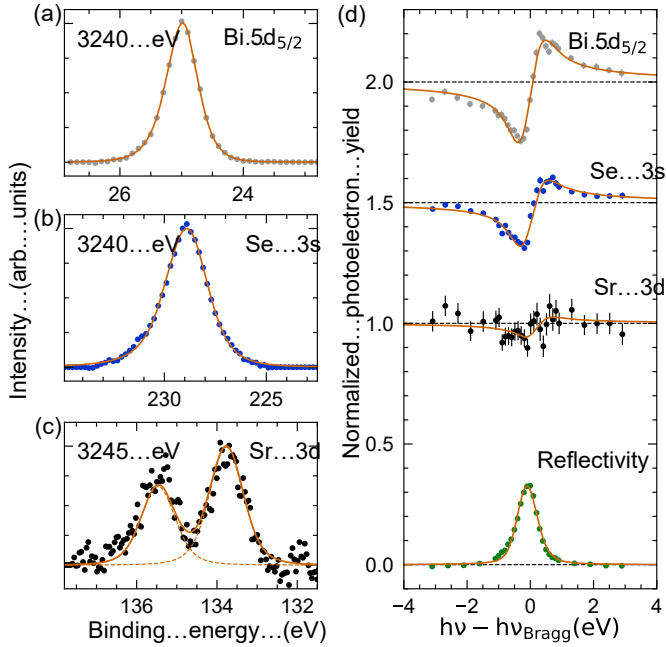


Figure 6.2: (a-c) Typical core-level spectra of Bi $5d_{5/2}$, Se $3s$ and Sr $3d$, respectively. The data were recorded about 3 eV off the Bragg energy. (d) NIXSW photoelectron yield curves (top), obtained from fitting XPS data that were recorded in an energy window of ± 3 eV around the Bragg energy of the Bi_2Se_3 (0 0 0 15) reflection, and reflectivity curve of this reflection (bottom). For Bi and Se individual XPS and NIXSW scans are displayed, while for Sr the sum of five individual scans is shown because of the low count rate. The curves for Se and Bi are displaced vertically by 0.5 and 1.0, respectively.

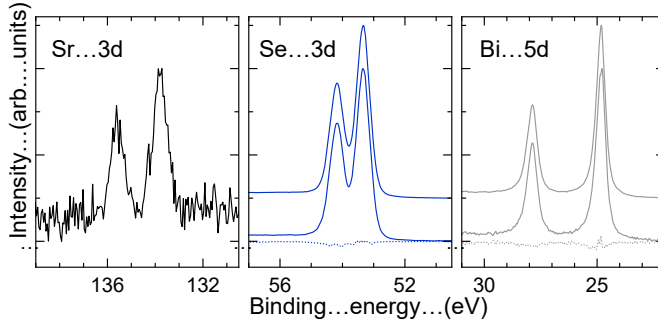


Figure 6.3: Core-level spectra of Bi_2Se_3 and $\text{Sr}_x\text{Bi}_2\text{Se}_3$, taken at photon energy of 700 eV. The Se 3d and Bi 5d spectra of the undoped (upper) and doped (lower) Bi_2Se_3 sample are vertically displaced in order to improve visibility. Difference plots ($\text{Sr}_x\text{Bi}_2\text{Se}_3 - \text{Bi}_2\text{Se}_3$) are shown as dotted lines.

the relevant species and their position(s) relative to the Bragg planes. When bulk species are considered, attenuation effects due to the finite inelastic mean free path have to be considered additionally [194,195], as discussed below.

In this case, for the bulk species of both Bi_2Se_3 and $\text{Sr}_x\text{Bi}_2\text{Se}_3$, there are two (for Bi) and three (for Se) inequivalent layers within the unit cell, namely those within one QL. This is illustrated in the side-view model shown in Fig. 6.1(a). All layers, except the central Se3 layer of a QL, are not located on diffraction planes of the (0 0 0 15) Bragg reflection used for the NIXSW measurements. The difference is very small for the Bi planes ($\Delta_{\text{Bi}} = 0.02 \text{ \AA}$), but much more significant for Se ($\Delta_{\text{Se}} = 0.31 \text{ \AA}$), and has different signs (negative for Se1 and Bi2, positive for Bi4 and Se5). Consequently, P_c^{H} of the individual atomic planes are equal to zero only for the central Se3 layer, not for the other four layers. For Se1 and Se5 one expects $P_{c,\text{Se}1,5}^{\text{H}} = \pm 0.164$, for Bi2 and Bi4 $P_{c,\text{Bi}2,4}^{\text{H}} = \pm 0.009$. This is illustrated in the Argand diagram presented in Fig. 6.4. Data points in this diagram represent radial vectors with their length corresponding to F_c^{H} and their polar angle to P_c^{H} . Multiple-site emission, as it occurs in the Bi_2Se_3 crystal, is then accounted for by the vector average of the Argand vectors representing the individual layers of identical species. For the three Se layers Se1, Se3, and Se5 of one QL, the individual Argand vectors are indicated by small blue circles at $(F_c^{\text{H}}, P_c^{\text{H}}) = (1.0, 0.164)$, $(1.0, 0.0)$, and $(1.0, 0.836)$ in Fig. 6.4. Note that the latter is equivalent to $(1.0, -0.164)$, and hence the average of the three vectors, which corresponds to the expected experimental result of a Se based NIXSW measurement, would be $(0.678, 0.0)$, i.e., in particular, P_c^{H} would be zero for such a measurement. This is to be expected, as long as the mirror symmetry of the full QL with

respect to the central Se layer is in place.

However, this symmetry is broken in the NIXSW experiment, not for structural reasons, but in its effect on the photoelectron yield that is obtained from the individual layers, due to the finite inelastic mean free path λ of electrons in matter. The photoemission yield that can be recorded from deeper layers is attenuated by a factor of $\alpha(z) = \exp(z/(\lambda \cos \phi))$, with $\phi = 80.9^\circ$ being the angle between the surface normal and the direction towards the electron analyzer. (Note that the positive z axis is defined towards the vacuum, and hence $z < 0$ for all atomic layers below the surface layer Se1.) Hence, all layers of the structure – even if they are structurally equivalent – contribute differently to the total photoelectron yield that is experimentally accessible. The attenuation factor, as found by fitting the experimental data (see below), is plotted in Fig. 6.1 (b).

The attenuation effect has obvious consequences for the averaging of Argand vectors. In the example mentioned above, the Argand vectors representing the three Se layers Se1, Se3, and Se5 have to be scaled in their lengths before averaging (i.e., their effective coherent fractions become $\alpha(z) \cdot F_c^{\mathbf{H}}$) and hence depend on the depth z of the corresponding layers below the surface. Accordingly, the averaged $P_c^{\mathbf{H}}$ will deviate from zero. In this example, Se1, the layer with $P_c^{\mathbf{H}} = -0.164$, is dominant due to its higher scaling factor. Depending on the specific value for λ , the resulting averaged Argand vector ends on the blue line shown in Fig. 6.4, between the two extreme cases of $(F_c^{\mathbf{H}}, P_c^{\mathbf{H}}) = (0.678, 0.0)$ for $\lambda \rightarrow \infty$ (all three layers contribute equally) and $(F_c^{\mathbf{H}}, P_c^{\mathbf{H}}) = (1.0, 0.836)$ for $\lambda \rightarrow 0$ (only the uppermost layer contributes). It can be seen that the experimental data points representing the Se $3s$ NIXSW results (blue diamonds) lie very close to the blue curve, which allows us to estimate the inelastic mean free path in the undoped Bi_2Se_3 . Note that the same calculation was performed for Bi2 and Bi4, as shown in Fig. 6.4, with small gray circles and lines (see also inset). However, the effect is much smaller for Bi due to the small distance Δ_{Bi} between the corresponding atomic and Bragg planes, and the experimental data points (gray diamonds) lie further away from the calculated ones (gray line running from $(F_c^{\mathbf{H}}, P_c^{\mathbf{H}}) = (1.0, 0.009)$ to $(1.0, 0.000)$ for $\lambda = 0$ to ∞).

With what has been said so far, it is clear that the inelastic mean free path effect fully explains the experimental NIXSW results of Se $3s$, but is not sufficient to account for those of Bi, regarding both coherent fraction and position ($(F_c^{\mathbf{H}}, P_c^{\mathbf{H}}) = (0.98, 0.89)$). For $F_c^{\mathbf{H}}$ this is not surprising, since the data was taken using a d -state emission line (the Bi $5d_{5/2}$), and hence the correction of non-dipolar effects cannot be properly performed for this species [183]. But for $P_c^{\mathbf{H}}$, usually much less affected by non-dipolar effects, the situation can only be improved when a relaxation of the uppermost layers of the crystal is taken

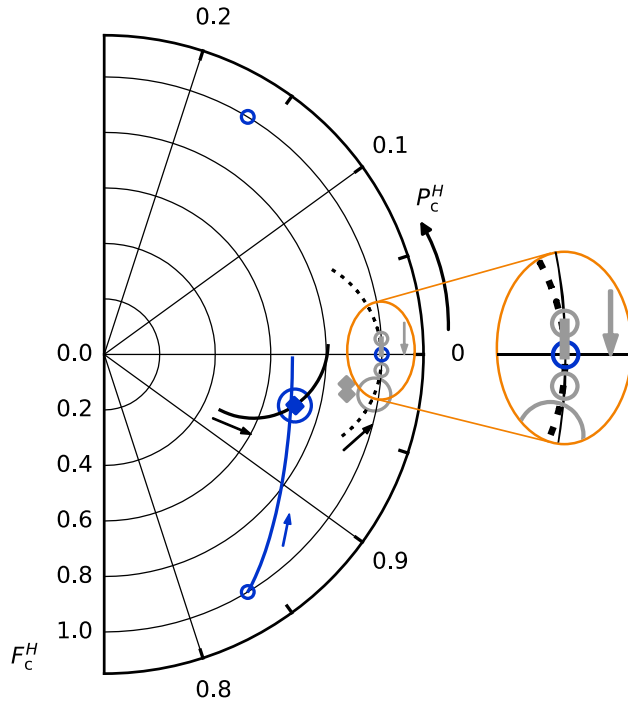


Figure 6.4: Illustration of the NIXSW results of Bi₂Se₃ in an Argand diagram. The data points represent radial vectors (Argand vectors), the lengths and polar angles of which correspond to F_c^H and P_c^H , respectively. Experimental data (all individual NIXSW scans) obtained for photoemission from Se 3s (Bi 5d_{5/2}) are shown as blue (gray) diamonds, numbers listed in Table 6.1 represent their average. Small open circles (three for Se, two for Bi) indicate the Argand vectors calculated for each individual atomic plane within one QL. Averaging the contributions of the individual layers, under variation of the inelastic mean free path λ (from zero to infinity in the direction of the small arrows), results in Argand vectors ending on the blue (gray) curved line for Se (Bi). Note that the gray curved line is very short, located close to $(F_c^H, P_c^H) = (1.0, 0.0)$, and hence also shown in the enlarged inset. Black lines (solid and dotted) indicate the variation of the expected NIXSW results for a relaxation of the uppermost layers of the Se and Bi species, respectively. They are calculated for $\lambda = 65 \text{ \AA}$ and a shift of the Se1 and Bi2 layer from -0.3 to $+0.3 \text{ \AA}$ (also in the direction of the small black arrows). The best agreement with the measured data is obtained for a Se1-Bi2 expansion of 9.7% to $\Delta_{\text{Se1-Bi2}} = 1.73 \text{ \AA}$, as indicated by large open circles.

into account. Any outward (inward) relaxation of an atomic layer increases (decreases) $P_c^{\mathbf{H}}$ of that layer, and hence rotates its Argand vector counter-clockwise (clockwise). A number of reasonable scenarios for layer relaxations were analyzed, e.g., a rigid shift of the entire first QL or a relaxation of the uppermost Bi and Se layers have been analyzed. A relaxation of the uppermost layers Se1 and Bi2 gave the best result. Fig. 6.4 illustrates the effect of Se1-Bi2 relaxation for the averaged NIXSW yield as curved black lines. The solid black line represents the resulting variation of the averaged Argand vector for values of the Se1 relaxation between -0.3 \AA and $+0.3 \text{ \AA}$ (in the direction of the small black arrow), calculated for $\lambda = 65 \text{ \AA}$. The dotted black line represents the result of a similar model calculation for Bi. It can be seen that this additional parameter helps significantly in explaining the experimental results, in particular for $P_c^{\mathbf{H}}$ of Bi.

Finally, all parameters were optimized (that is, the inelastic mean free path and the relaxation parameters for Se1 and Bi2) together in a least-squares fit on $P_c^{\mathbf{H}}$ of both Bi and Se, and $F_c^{\mathbf{H}}$ of Se [183]. This resulted in $\lambda = 65 \text{ \AA}$ and $\Delta_{\text{Se1-Bi2}} = 1.73 \text{ \AA}$, the latter corresponding to a 9.7% expansion of this interlayer spacing. First, the fitted value of λ is in good agreement with calculated values of the electron inelastic mean free path, which shows little variation between different materials at high kinetic energies (55 \AA to 80 \AA for a kinetic energy of about 3.1 keV [196]). Second, although NIXSW is not the best method to determine surface relaxation effects, the results are in qualitative agreement with Roy *et al.*, who found a relaxation of up to 11% for the Se1-Bi2 interlayer distance [197].

6.3.4 Strontium sites in $\text{Sr}_x\text{Bi}_2\text{Se}_3$

In this part, the NIXSW results on the Sr-doped crystal will be discussed, with the goal of identifying the vertical positions of the Sr atoms in the crystal. As can be seen in Table 6.1, the Bi and Se $P_c^{\mathbf{H}}$ differ only slightly from the values obtained for the Bi_2Se_3 crystal, while all $F_c^{\mathbf{H}}$ are smaller for $\text{Sr}_x\text{Bi}_2\text{Se}_3$. One can conclude that in the presence of the Sr dopants, a small amount of Se and Bi atoms are vertically displaced from their position in the Bi_2Se_3 lattice, which leads to a smaller $F_c^{\mathbf{H}}$ compared to the undoped crystal. However, the fact that the profile of the $(0\ 0\ 0\ 15)$ reflection is still very narrow, indicates that a meaningful NIXSW experiment is certainly possible. For the following analysis, it is assumed that the inelastic mean free path that was determined for the undoped crystal ($\lambda = 65 \text{ \AA}$, see Sec. 6.3.3) is unchanged by the doping.

In Fig. 6.5, the calculated NIXSW results (Argand vectors) for Sr are shown, considering all possible Sr positions (heights) in the Bi_2Se_3 unit cell, according to the symmetry of the structure. The full Bi_2Se_3 unit cell exhibits

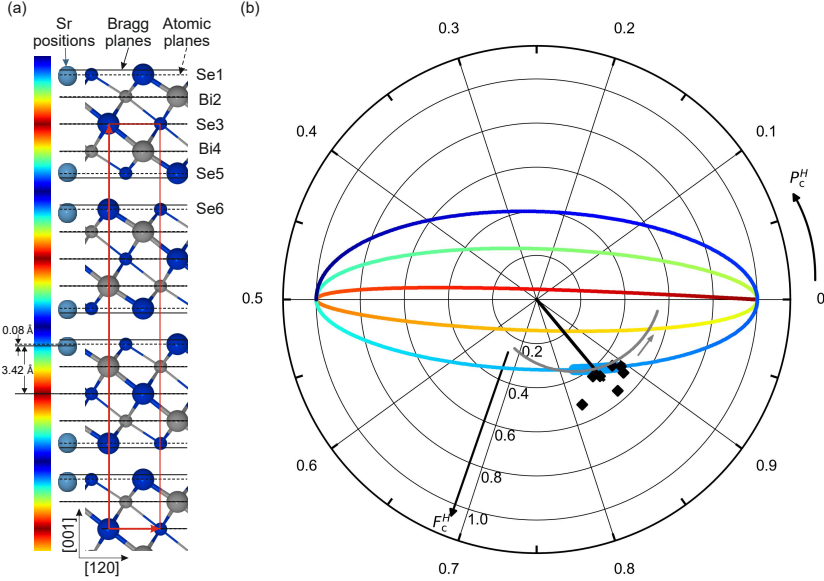


Figure 6.5: Simulation of all possible Sr sites. (a) Atomic model (side view) of the Bi_2Se_3 structure, see also Fig. 6.1. The color bar in the left illustrates all possible (vertical) Sr dopant positions, whereby symmetry equivalent positions are marked in the same color. The positions vary from the center of a vdW gap (dark blue) to the Se3 layer in the center of a QL (dark red). (b) Rainbow-colored spiral-type line: Argand representation of P_c^H and F_c^H as calculated for every possible Sr site, considering the unit cell symmetry. Each point on the line represents the head of the Argand vector (F_c^H, P_c^H) , its color corresponds to the vertical atomic position as shown by the color bar in the left of panel (a). For more details see the text. Black data points and black radial line: Results of seven individual Sr 3d NIXSW measurements and their average, respectively. The experimental data can only be reasonably explained by Sr positions represented by the cyan line section; the region of good agreement of calculated and experimental results is indicated by a thick cyan line. In the left of panel (a), the corresponding atomic positions in the unit cell are indicated by cyan balls. The gray line in (b) considers an additional relaxation of the uppermost Sr atoms and can be used to estimate the experimental uncertainty, see text.

inversion symmetry. Since the NIXSW experiment is only sensitive to vertical coordinates, all species effectively fulfill a mirror symmetry with two mirror planes: one located at the height of the central Se layer in each QL (Se3, 8, ...), the other in the center of the vdW gaps. Hence, any arbitrarily selected (vertical) site for a dopant species is duplicated within one QL by the first mirror plane and multiplied into all other QLs by the second. This is illustrated in Fig. 6.5 (a) by the color coding from dark blue to dark red (see color-bar in the left), representing all equivalent heights between the center of the vdW gap (blue) and the Se3 layer in the middle of the QLs (red). The color scale is multiplied into every other half of a QL according to the mirror planes. Cyan spheres are drawn to illustrate one specific case, a Sr position close to the Se1 and Se5 planes. As discussed in the following, this is the principal dopant position that was found in the NIXSW experiment.

In Fig. 6.5 (b) the simulated NIXSW result [189] for all possible dopant positions is shown. The rainbow-colored spiral-type line indicates the simulation results (the corresponding Argand vectors end on the line) for varying the dopant position, whereby the same color code as in Fig. 6.5 (a) was used. All multiplications of the specific sites (heights) by the mirror symmetry are considered and weighted with their corresponding attenuation factor. The shape of the line can be understood in the following gedankenexperiment:

Positioning the Sr dopants in the center of the vdW gap (dark blue color) results in the calculated Argand vector $(F_c^{\mathbf{H}}, P_c^{\mathbf{H}}) = (1.0, 0.5)$, as indicated by the dark blue color of the line at this position in Fig. 6.5(b). Upon moving the Sr atom through the crystal towards the Se3 plane, the expected Argand vector moves through the upper half of the diagram along the blue line section towards the right, at first reaching $(F_c^{\mathbf{H}}, P_c^{\mathbf{H}}) = (1.0, 0.0)$, close to the position of the Se1 layer. For dopant positions between Se1 and Bi2, it moves back along the lower blue-cyan-green line section to the starting point, and so on along the green-yellow-orange-red path. One full turn of the line (e.g., from $(1.0, 0.0)$ through $(1.0, 0.5)$ and back to $(1.0, 0.0)$), corresponds to moving the Sr atom from one Bragg-plane to the next, a distance that approximately equals the distance between two neighboring layers. The fact that the spiral-type line flattens from blue to red reflects the fact that the two equivalent Sr atoms in one QL move closer to each other, i.e., the difference in photoelectron yield from atoms on both sites becomes smaller due to a reduced inelastic mean free path effect. This reduces the resulting $F_c^{\mathbf{H}}$ after averaging over all equivalent sites. Note that all Argand vectors would end on a straight line connecting $(F_c^{\mathbf{H}}, P_c^{\mathbf{H}}) = (1.0, 0.0)$ and $(1.0, 0.5)$ (the spiral-type line would collapse to straight horizontal lines) if the inelastic mean free path effect was neglected ($\lambda \rightarrow \infty$).

It can clearly be seen that the experimental data (black data points and

black radial line) exclusively agrees with the position color-coded in cyan, corresponding to a dopant position close to those Se layers lying next to the vdW gaps (Se1, 5, 6, 11, ...). The best result is obtained for $(F_c^{\text{H}}, P_c^{\text{H}}) = (0.41, 0.86)$. This corresponds to a distance of only 0.08 Å between the Sr atoms and the Se1/Se5 layers (Sr closer to the center of the QL). The corresponding distance between the Sr atoms and the central Se layer (Se3) of the QL is 3.42 Å, see Fig. 6.5.

It is worth mentioning that this simulation is model-free. The only parameter used is the inelastic mean free path of the escaping photoelectrons, which is fixed to the value obtained from the measurements on the Bi₂Se₃ crystal ($\lambda = 65$ Å). Changing λ would stretch the spiral-type line vertically. However, in order to stretch it so far that the next closest calculated positions, the yellow-orange part of the elliptical curve, come close to the experimental data points, one had to decrease the inelastic mean free path by a factor of ≈ 3 , which appears to be very unrealistic. This result would even hold if a proper correction of the Sr 3*d* yield for non-dipolar effects was possible [183], since the change in F_c^{H} caused by such a correction is expected to be less than 20% [81].

Finally, the aspect of surface relaxation is addressed in a similar way as explained above for the bulk species Se and Bi. It was simulated, how the expected NIXSW result would change if one allows a relaxation of the uppermost Sr layer by $\Delta_{Sr1} = \pm 0.3$ Å, while keeping the position of all other Sr atoms fixed. The result is plotted as a gray line in Fig. 6.5 (b) running through the point $(F_c^{\text{H}}, P_c^{\text{H}}) = (0.41, 0.86)$, that is the center of the region of good agreement between simulation and experiment (thick cyan line). Close to that point (in particular towards the left), the gray line follows closely the cyan part of the spiral-type line, before it starts deviating to smaller F_c^{H} . This indicates that – in a certain range and to some extent – a relaxation of the uppermost Sr atoms can compensate for a slightly different position of all other Sr atoms in the QL, i.e., these parameters are highly correlated in this region. This correlation induces a certain uncertainty in the analysis, which, however, can be quantified: the two relevant parameters are d_{Sr} , the distance of all Sr atoms to the center of the QL, i.e., to the Se3 layer, and Δ_{Sr1} (additional) relaxation of the uppermost Sr atoms (those located close to the Se1 layer), with positive values corresponding to an outward relaxation, i.e., to an increase of the distance to the Se3 layer.

As mentioned above, one obtains the best agreement of experiment and simulation for $d_{Sr} = 3.42$ Å (with $\Delta_{Sr1} = 0$), and the relaxation in the range of $\Delta_{Sr1} = \pm 0.3$ Å (gray line in Fig. 6.5(b)) is simulated. The range, in which these two parameters are highly correlated, is mainly located in the left half of the gray line. On the right side, the line almost immediately deviates signifi-

cantly from the cyan-colored line section. Hence, the interval of correlation is asymmetric and can be estimated to $\Delta_{Sr1} = [-0.2, +0.1] \text{ \AA}$.

The corresponding change of the overall Sr position, which can be compensated by such a relaxation Δ_{Sr1} , is significantly smaller. This is the case simply because a change of d_{Sr} changes the position of many Sr atoms in the crystal, with a much greater effect on P_c^H than the displacement of only the Sr1 atoms. The corresponding interval for a change of d_{Sr} is therefore only $[+0.07, -0.03] \text{ \AA}$ (note the opposite sign of the numbers compared to the Δ_{Sr1} interval). In other words, a change of the overall position of the Sr atoms by $+0.07 \text{ \AA}$, that is from $d_{Sr} = 3.42 \text{ \AA}$ to $d_{Sr} = 3.49 \text{ \AA}$, can be compensated by a relaxation of the uppermost Sr atom by $\Delta_{Sr1} = -0.2 \text{ \AA}$. In the opposite direction, the corresponding shifts are smaller. A change of d_{Sr1} by -0.03 \AA is compensated by $\Delta_{Sr1} = +0.1 \text{ \AA}$. These numbers represent the *maximum* shifts of both parameters that can compensate each other and hence quantify the uncertainty of the result caused by the correlation of these two parameters. The (additional) statistical uncertainty in the measurements is estimated to be $\pm 0.03 \text{ \AA}$.

6.4 Conclusion

To unveil the vertical structure of superconducting $\text{Sr}_x\text{Bi}_2\text{Se}_3$, besides NIXSW, STM measurements were also performed by the collaboration partners from University of Cologne (see Ref. [172]). The identification of the Sr dopants based on their characteristic appearance in STM images leads to rather inconclusive results. NIXSW, however, was able to determine the dopant sites in the (near-surface) bulk crystal unambiguously. Due to the depth-dependent attenuation of the photoelectrons (inelastic mean free path), this method has the resolution to distinguish between otherwise symmetry-equivalent dopant sites in the bulk. The electron inelastic mean free path in matter causes an apparent break of the structure's symmetry and constitutes the backbone of the analysis.

The main result of the NIXSW study on the $\text{Sr}_x\text{Bi}_2\text{Se}_3$ sample is the unambiguous identification of the dopant vertical position: The majority of the Sr dopants are located close to the Se layers Se1 and Se5, vertically displaced towards the center of the QL by only $(0.08_{+0.06}^{-0.10}) \text{ \AA}$. This corresponds to a distance of $d_{Sr} = (3.42_{-0.06}^{+0.10}) \text{ \AA}$ to the Se3 layer in the center of the QL. In particular, this means that any significant amount of Sr atoms within the vdW gap can be excluded unambiguously by this data analysis. If there are dopants in the vdW gap, their occupation is minor and not detectable in NIXSW. The same is valid for the positions closer to the center of the QL, i.e., close to or between the Bi2/4 and Se3 layers. Note that the NIXSW is only sensitive

to the vertical positions of all species, and hence the lateral position of the dopants cannot be resolved. However, steric and chemical bonding conditions suggest that the Sr dopants occupy Se lattice sites in the Se1 and Se5 layers, only slightly relaxed towards the center of the QL.

When comparing this experimental result of the Sr dopant site with previous reports, one finds some agreement with the work by Li *et al.* [57]: These authors also found Sr at similar positions between the Se1 and Bi2 layer, but *not* within the vdW gap. However, the same data also showed some Sr atoms in between all other layers within the QLs. Interestingly, density functional theory calculations by the same group showed that Sr in between Se1 and Bi2 migrates into the vdW gap when the system is allowed to structurally relax. This apparent contradiction is however remedied by the need of quenching the crystals at the end of the crystal growth procedure. Apparently, in this way, Sr atoms are trapped at metastable doping sites, and therefore, these energetically unfavorable dopant sites may indeed be predominantly responsible for the high superconducting volume fraction observed in quenched crystals [58].

Chapter 7

Summary

The main part (chapters 3 to 5) of this work is dedicated to graphene-related stacked layer systems because of the intriguing electronic properties that have been found on such systems [7, 20, 21, 23, 24, 30, 83–85, 112–119]. In particular, twisted bi- and multilayers attracted enormous interest of the scientific community recently. We therefore concentrated on systems containing unconventionally oriented graphene layers and on recipes to grow them epitaxially. The vertical structures of such layered systems is a result of interactions between atomic layers, which in turn can be modified by intercalation, with the goal of producing large scale two-dimensional graphene layers that are fully decoupled from the substrate. Determining the vertical structures of graphene-related stacked systems, in particular the precise layer distances, allows one to judge the coupling and interaction strengths between the layers and hence contributes to the understanding of the growth mechanisms and properties of the stacked layer system.

A smaller part of this work deals with a topological superconductor, namely Sr-doped Bi_2Se_3 crystal. The key question is at which sites the Sr dopant is located in the crystal. This question could be answered in chapter 6. But there is also an interesting technical aspect involved in this part: NIXSW technique is demonstrated to be a powerful tool to investigate not only thin layers located on top of a crystal surface but also dopant positions in a bulk crystal. By considering the inelastic mean free path of electrons in matter, the vertical positions of the Sr dopants in the bulk Bi_2Se_3 crystal could be identified. This new concept of analyzing NIXSW data might open a door for future research on similar systems.

In this work, beside the just mentioned NIXSW method, XPS was applied to determine the chemical compositions as well as the chemical environment of stacked layers. Furthermore, high-resolution LEED and ARPES were performed to determine the lateral and electronic structure of the investigated systems. All these methods average over an area of hundreds of μm^2 . In this

way, local defects will be averaged out and one gains overall information of the measured area. Such measurements are at the same time challenging since they require a certain degree of homogeneity within the measurement footprints.

Epitaxial graphene on SiC

Growing graphene epitaxially in an unconventional orientation (0°) is considered to be a substantial step to 30° -tBLG preparation. This can be done by decomposing SiC by annealing in borazine atmosphere, whereby at first a boron nitride layer occurs. This layer was reported to be hBN [95], however, the finding was based on very weak electronic bands detected in ARPES, and hence not very convincing. For our samples, which were prepared in the same way, we did not see an hBN electronic bandstructure and hence conclude that the layer is actually a non-stoichiometric B_xN_y - $R0^\circ$ layer. With such a preparation route, the stacked system consists of a boron zeroth-layer (ZL) on top of the Si-terminated substrate surface, and a B_xN_y - $R0^\circ$ layer on top of the ZL.

Focusing on the layer properties of the B_xN_y - $R0^\circ$, it was found with NIXSW that the B_xN_y - $R0^\circ$ layer is very flat since boron and nitrogen atoms are found on almost the same height (5.49 Å and 5.47 Å, respectively). These heights correspond to a B_xN_y - $R0^\circ$ to ZL layer distance of 2.94 Å, that is only 77% of the corresponding vdW bonding distance. This shows that the B_xN_y - $R0^\circ$ layer is not freestanding, which may cause the absence of the electronic bandstructure of hBN.

The preparation temperature was found to be a crucial parameter and influences the chemical composition, lateral and vertical structures of each layer in the stacked system. For preparation temperatures from 1100°C to 1150°C , B_xN_y - $R0^\circ$ was found on the sample, with a (5×5) diffraction pattern observed with LEED. From 1175°C to 1250°C , diffraction spots of the B_xN_y - $R0^\circ$ layer are gradually replaced by those of G - $R0^\circ$. Also in XPS, it can be seen that the B_xN_y - $R0^\circ$ component intensity reduces, while that of the C_G component increases with increasing preparation temperature.

Based on the result from the B_xN_y - $R0^\circ$ layer, chapter 4 focuses on the comparison of two preparation routes for G - $R0^\circ$, namely the "template method" and "surfactant method", which prepares T graphene and S graphene, respectively. For the template method, one takes the B_xN_y - $R0^\circ$ sample, anneals it in UHV, and obtains G - $R0^\circ$ (Fig. 4.1). This route, however, produces graphene with low quality. The surfactant method, on the other hand, can produce high-quality G - $R0^\circ$ by annealing the SiC wafer in borazine atmosphere at 1300°C . The quality difference in the G - $R0^\circ$ obtained from these two routes can be observed in Fig. 4.3. A profile analysis of the G - $R0^\circ$ LEED spot, the G - $R0^\circ$ domains were found to have an averaged size smaller than the average SiC ter-

race size and an azimuthal disorder with the standard deviation of $0.458(2)^\circ$.

Using the NIXSW technique, the coverages of the graphene layers in the samples were quantified (Fig. 4.6). T graphene obtained at about 1300°C turned out to be a graphene bilayer system: Above a carbon zeroth-layer, we found two graphene layers both with coverages of approximately 0.6 monolayer (ML) (assuming a full ML coverage for the ZL underneath). S graphene has almost no second graphene layer, whose coverage is only 0.1 ML, while the first layer is almost a closed layer (0.9 ML). Hence, this sample represents a very good $G-R0^\circ$ single layer graphene. High-resolution LEED also showed higher layer quality, larger graphene domain size for S graphene. S graphene is therefore a promising platform for 30° -tBLG preparation, if one succeeds in decoupling the ZL from the substrate, e.g. by intercalation, it would transform into a 1 ML $G-R30^\circ$ layer being located underneath a high-quality $G-R0^\circ$ layer.

Sb-intercalated graphene on SiC

When epitaxial graphene on SiC was prepared, it was found that the graphene has to be decoupled from the SiC to exhibit the desired electronic properties. Intercalation of atomic species has been one of the ways to decouple graphene from the SiC substrate [41, 43, 44, 48, 54]. Wolff *et al.* succeeded to intercalate atomic Sb to decouple the carbon zeroth-layer from the SiC and obtained quasi-freestanding single layer graphene [49]. However, from their work, there was one open remaining question: How many atomic layer does the Sb-intercalation consist of? Since the number of atomic layers of the metal intercalation can impact the electronic properties of the overlaying layers [54], answering this question enables further optimization of the intercalation.

This question could be answered using NIXSW: We found that the Sb layer consists of only one atomic layer, which lies $2.6 \pm 0.2\text{\AA}$ above the SiC surface. This finding refutes the speculation that the intercalated Sb layer may comprise of multiple atomic layers. The graphene layer is located $3.6 \pm 0.2\text{\AA}$ above the Sb-intercalation layer, which corresponds to 96% of the van der Waals bonding distance and therefore indicates that the graphene layer is quasi-freestanding.

Sr-doped bismuth selenide

In the field of topological superconductors, such as $\text{Cu}_x\text{Bi}_2\text{Se}_3$ and $\text{Sr}_x\text{Bi}_2\text{Se}_3$, the origin of the superconductivity has been the main question that many studies tried to answer. In this context, the precise position(s) of the dopants in the Bi_2Se_3 bulk lattice seems to play an important role. So far, DFT

calculations suggest that Cu and Sr are energetically more favorable in the van der Waals gaps between the quintuple layers [56,57]. However, no experimental evidence has been able to support this directly [58–62,181].

In this work, the vertical structure of the topological superconducting $\text{Sr}_x\text{Bi}_2\text{Se}_3$ crystal was determined using the NIXSW technique (see chapter 6). We concluded that the Sr dopants do not reside in the vdW gaps but in the quintuple layer, a result that differs from previous interpretations [57,58,181]. The majority of the Sr atoms were found at $d_{\text{Sr}} = 3.42_{-0.06}^{+0.10}$ Å from the Se3 layer, this is close to the van der Waals gaps but still within the quintuple layers. Beside a moderate relaxation of the topmost atomic layers (9.7% expansion of the Se1-Bi2 layer distance), the structure of the Bi_2Se_3 host crystal is not significantly changed by the dopants. This is also confirmed by soft XPS results that detect no changes in the chemical environment of all species.

It was also found that quenching the sample after the high-temperature doping procedure plays an important role for the topological superconductivity [198–201]. This apparently traps the Sr dopants in metastable sites, which might (i) be responsible for the superconductivity the $\text{Sr}_x\text{Bi}_2\text{Se}_3$ exhibits, and (ii) solve the apparent contradiction between the DFT and our experimental results.

Finally, it should be mentioned that such an investigation of bulk properties with NIXSW is rather unusual. At first sight, the crystal symmetry (mirror planes in the center of both the quintuple layers and the vdW gaps) would have made a NIXSW investigation useless, simply since the signal from symmetry-equivalent positions would cancel out the information on the vertical position of all species. However, the inelastic mean free path of the photoemitted electrons breaks this symmetry, since symmetry-equivalent atoms are located in different depths below the surface, and hence do not contribute equally to the photoelectron yield. Only this effect allowed the determination of the dopants' vertical positions and the detection of the topmost bulk layers relaxation.

Bibliography

- [1] T. Georgiou, R. Jalil, B. D. Belle, L. Britnell, R. V. Gorbachev, S. V. Morozov, Y.-J. Kim, A. Gholinia, S. J. Haigh, O. Makarovskiy, L. Eaves, L. A. Ponomarenko, A. K. Geim, K. S. Novoselov, and A. Mishchenko, Vertical field-effect transistor based on graphene–WS₂ heterostructures for flexible and transparent electronics, *Nature Nanotechnol.* **8**, 100 (2013).
- [2] L. Wang, I. Meric, P. Y. Huang, Q. Gao, Y. Gao, H. Tran, T. Taniguchi, K. Watanabe, L. M. Campos, D. A. Muller, J. Guo, P. Kim, J. Hone, K. L. Shepard, and C. R. Dean, One-Dimensional Electrical Contact to a Two-Dimensional Material, *Science* **342**, 614 (2013).
- [3] K. S. Novoselov, A. Mishchenko, A. Carvalho, A. H. Castro Neto, 2D materials and van der Waals heterostructures, *Science* **353**, 6298 (2016).
- [4] A. K. Geim and I. V. Grigorieva, Van der Waals heterostructures, *Nature* **499**, 419 (2013).
- [5] D. Rhodes, S. H. Chae, R. Ribeiro-Palau, and J. Hone, Disorder in van der Waals heterostructures of 2D materials, *Nature Materials* **18**, 541 (2019).
- [6] K. Roy, M. Padmanabhan, S. Goswami, T. P. Sai, G. Ramalingam, S. Raghavan, and A. Ghosh, Graphene–MoS₂ hybrid structures for multifunctional photoresponsive memory device, *Nature Nanotechnol.* **8**, 826 (2013).
- [7] A. K. Geim, Graphene: Status and Prospects, *Science* **324**, 1530 (2009).
- [8] C. Lee, X. Wei, J. W. Kysar, and J. Hone, Measurement of the Elastic Properties and Intrinsic Strength of Monolayer Graphene, *Science* **321**, 385 (2008).
- [9] G. Tsoukleri, J. Parthenios, K. Papagelis, R. Jalil, A. C. Ferrari, A. K. Geim, K. S. Novoselov, and C. Galotis, Subjecting a Graphene Monolayer to Tension and Compression, *Small* **5**, 2397 (2009).

- [10] A. Rycerz, J. Tworzydło, and C. W. J. Beenakker, Valley filter and valley valve in graphene, *Nat. Phys.* **3**, 172 (2007).
- [11] H. B. Heersche, P. Jarillo-Herrero, J. B. Oostinga, L. M. K. Vandersypen, and A. F. Morpurgo, Bipolar supercurrent in graphene, *Nature* **446**, 56 (2007).
- [12] P. Avouris, Z. Chen, and V. Perebeinos, Carbon-based electronics, *Nat. Nanotechnol.* **2**, 605 (2007).
- [13] M. Burghard, H. Klauk, and K. Kern, Carbon-Based Field-Effect Transistors for Nanoelectronics, *Adv. Mater.* **21**, 2586 (2009).
- [14] P. Recher and B. Trauzettel, Quantum dots and spin qubits in graphene, *Nanotechnology* **21**, 302001 (2010).
- [15] F. Schwierz, Graphene transistors, *Nat. Nanotechnol.* **5**, 487 (2010).
- [16] X. Xu, C. Liu, Z. Sun, T. Cao, Z. Zhang, E. Wang, Z. Liu, and K. Liu, Interfacial engineering in graphene bandgap, *Chem. Soc. Rev.* **47**, 3059 (2018).
- [17] S. Y. Zhou, G.-H. Gweon, A. V. Fedorov, P. N. First, W. A. De Heer, D.-H. Lee, F. Guinea, A. H. Castro Neto, and A. Lanzara, Substrate-induced bandgap opening in epitaxial graphene, *Nat. Mater.* **6**, 770 (2007).
- [18] O. Frank, J. Vejpravova, V. Holy, L. Kavan, M. Kalbac, Interaction between graphene and copper substrate: The role of lattice orientation, *Carbon* **68**, 440 (2014).
- [19] Y. Cao, J. Y. Luo, V. Fatemi, S. Fang, J. D. Sanchez-Yamagishi, K. Watanabe, T. Taniguchi, E. Kaxiras, and P. Jarillo-Herrero, Superlattice-Induced Insulating States and Valley-Protected Orbits in Twisted Bilayer Graphene, *Phys. Rev. Lett.* **117**, 116804 (2016).
- [20] Y. Cao, V. Fatemi, S. Fang, K. Watanabe, T. Taniguchi, E. Kaxiras, and P. Jarillo-Herrero, Unconventional superconductivity in magic-angle graphene superlattices, *Nature* **556**, 43 (2018).
- [21] Y. Cao, V. Fatemi, A. Demir, S. Fang, S. L. Tomarken, J. Y. Luo, J. D. Sanchez-Yamagishi, K. Watanabe, T. Taniguchi, E. Kaxiras, R. C. Ashoori, and P. Jarillo-Herrero, Correlated insulator behaviour at half-filling in magic-angle graphene superlattices, *Nature* **556**, 80 (2018).

-
- [22] M. J. Park, Y. Kim, G. Y. Cho, and S. Lee, Higher-Order Topological Insulator in Twisted Bilayer Graphene, *Phys. Rev. Lett.* **123**, 216803 (2019).
- [23] M. Yankowitz, S. Chen, H. Polshyn, Y. Zhang, K. Watanabe, T. Taniguchi, D. Graf, A. F. Young, and C. R. Dean, Tuning superconductivity in twisted bilayer graphene, *Science* **363**, 2059 (2019).
- [24] H. Yoo, R. Engelke, S. Carr, S. Fang, K. Zhang, P. Cazeaux, S. H. Sung, R. Hovden, A.W. Tsen, T. Taniguchi, K. Watanabe, G.-C. Yi, M. Kim, M. Luskun, E. B. Tadmor, E. Kaxiras, and P. Kim, Atomic and electronic reconstruction at the van der Waals interface in twisted bilayer graphene, *Nature Mater.* **18**, 448 (2019).
- [25] P. Seidel, Applied superconductivity, *Handbook on Devices and Applications*. Wiley Verlag GmbH & Co. KGaA2015ISBN: 978-3-527-67063-5
- [26] J. Shao, and W. Zhu, Emerging Superconductivity and Topological States in Bismuth Chalcogenides, *Superfluids and Superconductors* **Chapter 6**, 989 (2017).
- [27] A. H. Castro Neto, F. Guinea, N. M. R. Peres, K. S. Novoselov, and A. K. Geim, The electronic properties of graphene, *Rev. Mod. Phys.* **81**, 109 (2009).
- [28] R. W. Havener, Y. Liang, L. Brown, L. Yang, and J. Park, Van Hove Singularities and Excitonic Effects in the Optical Conductivity of Twisted Bilayer Graphene, *Nano Lett.* **14**, 3353 (2014).
- [29] W. Yao, E. Wang, C. Bao, Y. Zhang, K. Zhang, K. Bao, C. K. Chan, C. Chen, J. Avila, M. C. Asensio, J. Zhu, and S. Zhou, Quasicrystalline 30° twisted bilayer graphene as an incommensurate superlattice with strong interlayer coupling, *Proc. Natl. Sci. U.S.A.* **115**, 6928 (2018).
- [30] C. Yan, D.-L. Ma, J.-B. Qiao, H.-Y. Zhong, L. Yang, S.-Y. Li, Z.-Q. Fu, Y. Zhang, and L. He, Scanning tunneling microscopy study of the quasicrystalline 30° twisted bilayer graphene, *2D Mater.* **6**, 045041 (2019).
- [31] C. Berger, Z. Song, T. Li, X. Li, A. Y. Ogbazghi, R. Feng, Z. Dai, A. N. Marchenkov, E. H. Conrad, P. N. First, and W. A. de Heer, Ultrathin Epitaxial Graphite: 2D Electron Gas Properties and a Route toward Graphene-based Nanoelectronics, *J. Phys. Chem. B* **108**, 19912 (2004).
- [32] J. Kedzierski, P.-L. Hsu, P. Healey, P. W. Wyatt, C. L. Keast, M. Sprinkle, C. Berger, and W. A. de Heer, Epitaxial Graphene Transistors on SiC Substrates, *IEEE Trans. Electron Devices* **55**, 2078 (2008).

- [33] W. A. de Heer, C. Berger, X. Wua, P. N. First, E. H. Conrad, X. Li, T. Li, M. Sprinkle, J. Hass, M. L. Sadowski, M. Potemski, G. Martinez, Epitaxial graphene, *Solid State Commun.* **143**, 92 (2007).
- [34] T. Seyller, A. Bostwick, K. V. Emtsev, K. Horn, L. Ley, J. L. McChesney, T. Ohta, J. D. Riley, E. Rotenberg, and F. Speck, Epitaxial graphene: a new material, *Phys. Stat. Sol. (b)* **245**, 1436 (2008).
- [35] F. Varchon, R. Feng, J. Hass, X. Li, B. Ngoc Nguyen, C. Naud, P. Mallet, J.-Y. Veuillein, C. Berger, E. H. Conrad, and L. Magaud, Electronic Structure of Epitaxial Graphene Layers on SiC: Effect of the Substrate, *Phys. Rev. Lett.* **99**, 126805 (2007).
- [36] C. Riedl, C. Coletti, and U. Starke, Structural and electronic properties of epitaxial graphene on SiC(0001): a review of growth, characterization, transfer doping and hydrogen intercalation, *J. Phys. D: Appl. Phys.* **43**, 374009 (2010).
- [37] C. Riedl and U. Starke, Structural properties of the graphene-SiC(0001) interface as a key for the preparation of homogeneous large-terrace graphene surfaces, *Phys. Rev. B* **76**, 245406 (2007).
- [38] K. I. Bolotin, K. J. Sikes, Z. Jiang, M. Klima, G. Fudenberg, J. Hone, P. Kim, H. L. Stormer, Ultrahigh electron mobility in suspended graphene, *Solid State Commun.* **146**, 351 (2008).
- [39] J. Jobst, D. Waldmann, F. Speck, R. Hirner, D. K. Maude, T. Seyller, and H. B. Weber, Quantum oscillations and quantum Hall effect in epitaxial graphene, *Phys. Rev. B* **81**, 195434 (2010).
- [40] J. A. Robinson, M. Hollander, M. LaBella, K. A. Trumbull, R. Cavalero, and D. W. Snyder, Epitaxial Graphene Transistors: Enhancing Performance via Hydrogen Intercalation, *Nano Lett.* **11**, 3875 (2011).
- [41] C. Riedl, C. Coletti, T. Iwasaki, A. A. Zakharov, and U. Starke, Quasi-Free-Standing Epitaxial Graphene on SiC Obtained by Hydrogen Intercalation, *Phys. Rev. Lett.* **102**, 246804 (2009).
- [42] S. L. Wong, H. Huang, Y. Wang, L. Cao, D. Qi, I. Santoso, W. Chen, and A. T. S. Wee, Quasi-Free-Standing Epitaxial Graphene on SiC (0001) by Fluorine Intercalation from a Molecular Source, *ACS Nano* **5**, 7662 (2011).
- [43] K. V. Emtsev, A. A. Zakharov, C. Coletti, S. Forti, and U. Starke, Ambipolar doping in quasifree epitaxial graphene on SiC(0001) controlled by Ge intercalation, *Phys. Rev. B* **84**, 125423 (2011).

-
- [44] C. Virojanadara, S. Watcharinyanon, A. A. Zakharov, and L. I. Johansson, Epitaxial graphene on 6H-SiC and Li intercalation, *Phys. Rev. B* **82**, 205402 (2010).
- [45] L. H. de Lima, R. Landers, and A. de Siervo, Patterning Quasi-Periodic Co 2D-Clusters underneath Graphene on SiC(0001), *Chem. Mater.* **26**, 4172 (2014).
- [46] S. Oida, F. R. McFeely, J. B. Hannon, R. M. Tromp, M. Copel, Z. Chen, Y. Sun, D. B. Farmer, and J. Yurkas, Decoupling graphene from SiC(0001) via oxidation, *Phys. Rev. B* **82**, 041411(R) (2010).
- [47] K. Yagyu, K. Takahashi, H. Tochihara, H. Tomokage, and T. Suzuki, Neutralization of an epitaxial graphene grown on a SiC(0001) by means of palladium intercalation, *Appl. Phys. Lett.* **110**, 131602 (2017).
- [48] I. Gierz, T. Suzuki, R. T. Weitz, D. S. Lee, B. Krauss, C. Riedl, U. Starke, H. Höchst, J. H. Smet, C. R. Ast, and K. Kern, Electronic decoupling of an epitaxial graphene monolayer by gold intercalation, *Phys. Rev. B* **81**, 235408 (2010).
- [49] S. Wolff, S. Roscher, F. Timmermann, M. V. Daniel, F. Speck, M. Wanke, M. Albrecht, and T. Seyller, Quasi-Freestanding Graphene on SiC(0001) by Ar-Mediated Intercalation of Antimony: A Route Toward Intercalation of High-Vapor-Pressure Elements, *Ann. Phys. (Amsterdam)* **531**, 1900199 (2019).
- [50] C. Xia, L. I. Johansson, Y. Niu, A. A. Zakharov and E. Janze, High thermal stability quasi-free-standing bilayer graphene formed on 4H-SiC(0001) via platinum intercalation, *Carbon* **79**, 631 (2014).
- [51] Y. Zhang, H. Zhang, Y. Cai, J. Song, and P. He, The investigation of cobalt intercalation underneath epitaxial graphene on 6H-SiC(0001), *Nanotechnol.* **28**, 075701 (2017).
- [52] S. Forti, A. Stöhr, A. A. Zakharov, C. Coletti, K. V. Emtsev, and U. Starke, Mini-Dirac cones in the band structure of a copper intercalated epitaxial graphene superlattice, *2D Mater.* **3**, 035003 (2016).
- [53] G. Kowalski, M. Tokarczyk, P. Dabrowski, P. Ciepielewski, M. Mozdzonek, W. Strupinski, and J. M. Baranowski, New X-ray insight into oxygen intercalation in epitaxial graphene grown on 4H-SiC(0001), *J. Appl. Phys.* **117**, 105301 (2015).

- [54] N. Briggs, Z. M. Gebeyehu, A. Vera, T. Zhao, K. Wang, A. De La Fuente Duran, B. Bersch, T. Bowen, K. L. Knappenberger, Jr., and J. A. Robinson, Epitaxial graphene/silicon carbide intercalation: a minireview on graphene modulation and unique 2D materials, *Nanoscale* **11**, 15440 (2019).
- [55] Y. S. Hor, A. J. Williams, J. G. Checkelsky, P. Roushan, J. Seo, Q. Xu, H. W. Zandbergen, A. Yazdani, N. P. Ong, and R. J. Cava, Superconductivity in $\text{Cu}_x\text{Bi}_2\text{Se}_3$ and its Implications for Pairing in the Undoped Topological Insulator, *Phys. Rev. Lett.* **104**, 057001 (2010).
- [56] Y.-L. Wang, Y. Xu, Y.-P. Jiang, J.-W. Liu, C.-Z. Chang, M. Chen, Z. Li, C.-L. Song, L.-L. Wang, K. He, X. Chen, W.-H. Duan, Q.-K. Xue, and X. C. Ma, Structural defects and electronic properties of the Cu-doped topological insulator Bi_2Se_3 , *Phys. Rev. B* **84**, 075335 (2011).
- [57] Z. Li, M. Wang, D. Zhang, N. Feng, W. Jiang, C. Han, W. Chen, M. Ye, C. Gao, J. Jia, J. Li, S. Qiao, D. Qian, B. Xu, H. Tian, and B. Gao, Possible structural origin of superconductivity in Sr-doped Bi_2Se_3 , *Phys. Rev. Materials* **2**, 014201 (2018).
- [58] Shruti, V. K. Maurya, P. Neha, P. Srivastava, and S. Patnaik, Superconductivity by Sr intercalation in the layered topological insulator Bi_2Se_3 , *Phys. Rev. B* **92**, 020506(R) (2015).
- [59] T. Shirasawa, M. Sugiki, T. Hirahara, M. Aitani, T. Shirai, S. Hasegawa, and T. Takahashi, Structure and transport properties of Cu-doped Bi_2Se_3 films, *Phys. Rev. B* **89**, 195311 (2014).
- [60] M. Wang, Y. Song, L. You, Z. Li, B. Gao, X. Xie, and M. Jiang, A combined method for synthesis of superconducting Cu doped Bi_2Se_3 , *Sci. Rep.* **6**, 22713 (2016).
- [61] T. Fröhlich, Z. Wang, M. Bagchi, A. Stunault, Y. Ando, and M. Braden, Crystal structure and distortion of superconducting $\text{Cu}_x\text{Bi}_2\text{Se}_3$, *Phys. Rev. Materials* **4**, 054802 (2020).
- [62] C. Callaert, M. Bercx, D. Lamoen, and J. Hadermann, Interstitial defects in the van der Waals gap of Bi_2Se_3 , *Acta Cryst. B* **75**, 717 (2019).
- [63] J. Dai, D. West, X. Wang, Y. Wang, D. Kwok, S.-W. Cheong, S. B. Zhang, and W. Wu, Toward the Intrinsic Limit of the Topological Insulator Bi_2Se_3 , *Phys. Rev. Lett.* **117**, 106401 (2016).

-
- [64] M. Wang, D. Zhang, W. Jiang, Z. Li, C. Han, J. Jia, J. Li, S. Qiao, D. Qian, H. Tian, and B. Gao, Growth and structural characterisation of Sr-doped Bi₂Se₃ thin films, *Sci. Rep.* **8**, 2192 (2018).
- [65] M. P. Seah and W. A. Dench, Quantitative electron spectroscopy of surfaces: A standard data base for electron inelastic mean free paths in solids, *Surf. Interface Anal.* **1**, 1 (1979).
- [66] U. Scheithauer, G. Meyer and M. Henzler, A new LEED instrument for quantitative spot profile analysis, *Surf. Sci.* **178**, 441 (1986).
- [67] P. Kury, see WinSPA website, winspa.de/hardware.html.
- [68] M. Horn von Hoegen, Growth of semiconductor layers studied by spot profile analysing low energy electron diffraction, *Z. Kristallogr. Cryst. Mater.* **214**, 591 (1999).
- [69] G. Comsa, Coherence length and/or transfer width?, *Surf. Sci.* **81**, 57 (1979).
- [70] T.-M. Lu and M. G. Lagally, The resolving power of a low-energy electron diffractometer and the analysis of surface defects, *Surf. Sci.* **99**, 695 (1980).
- [71] G.-C. Wang, M. G. Lagally, Quantitative island size determination in the chemisorbed layer W(110) p(2 × 1)-O: I. Instrument response function and substrate perfection, *Surf. Sci.* **81**, 69 (1979).
- [72] C. Klein, Erzeugung, Analyse und Manipulation von Systemen mit spin-aufgespaltenen Zuständen, Dissertation, Universität Duisburg-Essen (2015).
- [73] We used the LEEDLab/LEEDCal software package to correct the LEED patterns for distortions and calibrate them in absolute k -space units, using a reference measurement on the well known Si(111) (7 × 7) reconstruction [74]. The latest version of the software package is available at <https://fritz-sojka-gbr.de/leedlab/>.
- [74] F. Sojka, M. Meissner, C. Zwick, R. Forker, and T. Fritz, Determination and correction of distortions and systematic errors in low-energy electron diffraction, *Rev. Sci. Instrum.* **84**, 015111 (2013).
- [75] S. Hüfner, *Photoelectron Spectroscopy*, Springer, (2003).
- [76] H. Ibach, *Electron Spectroscopy for Surface Analysis*, Springer, Berlin, Heidelberg, New York (1977).

- [77] A. Damascelli, Z. Hussain, and Z.-X. Shen, Angle-resolved photoemission studies of the cuprate superconductors, *Rev. Mod. Phys.* **75**, 473 (2003).
- [78] Shen Laboratory, Stanford University, Angle-Resolved Photoemission Spectroscopy.
- [79] D. P. Woodruff, Surface structure determination using X-ray standing waves, *Rep. Prog. Phys.* **68**, 743 (2005).
- [80] J. Zegenhagen and A. Kazimirov, *The X-ray standing wave technique: principles and applications*, World Scientific Publishing Company (2013).
- [81] G. van Straaten, M. Franke, F. C. Bocquet, F. S. Tautz, and C. Kumpf, Non-dipolar effects in photoelectron-based normal incidence x-ray standing wave experiments, *J. Electron Spectrosc. Relat. Phenom.* **222**, 106 (2018).
- [82] F. C. Bocquet, G. Mercurio, M. Franke, G. van Straaten, S. Weiß, S. Soubatch, C. Kumpf, and F. S. Tautz, TORRICELLI: A software to determine atomic spatial distributions from normal incidence x-ray standing wave data, *Comput. Phys. Commun.* **235**, 502 (2019).
- [83] K. S. Novoselov, A. K. Geim, S. V. Morozov, D. Jiang, M. I. Katsnelson, I. V. Grigorieva, S. V. Dubonos, and A. A. Firsov, Two-dimensional gas of massless Dirac fermions in graphene, *Nature* **438**, 197 (2005).
- [84] J. M. B. Lopes dos Santos, N. M. R. Peres, and A. H. Castro Neto, Graphene Bilayer with a Twist: Electronic structure, *Phys. Rev. Lett.* **99**, 256802 (2007).
- [85] A. V. Rozhkov, A. O. Sboychakov, A. L. Rakhmanov, and F. Nori, Electronic properties of graphene-based bilayer systems, *Phys. Rep.* **648**, 1 (2016).
- [86] R. Frisenda, E. Navarro-Moratalla, P. Gant, D. Perez De Lara, P. Jarillo-Herrero, R. V. Gorbachev, and A. Castellanos-Gomez, Recent progress in the assembly of nanodevices and van der Waals heterostructures by deterministic placement of 2D materials, *Chem. Soc. Rev.* **47**, 53 (2018).
- [87] L. Britnell, R. V. Gorbachev, R. Jalil, B. D. Belle, F. Schedin, M. I. Katsnelson, L. Eaves, S. V. Morozov, A. S. Mayorov, N. M. R. Peres, A. H. Castro Neto, J. Leist, A. K. Geim, L. A. Ponomarenko, and K. S. Novoselov, Electron Tunneling through Ultrathin Boron Nitride Crystalline Barriers, *Nano Lett.* **12**, 1707 (2012).

-
- [88] C. R. Dean, A. F. Young, I. Meric, C. Lee, L. Wang, S. Sorgenfrei, K. Watanabe, T. Taniguchi, P. Kim, K. L. Shepard, and J. Hone, Boron nitride substrates for high-quality graphene electronics, *Nat. Nanotechnol.* **5**, 722 (2010).
- [89] S. Ahn, G. Kim, P. K. Nayak, S. In Yoon, H. Lim, H.-J. Shin, and H. S. Shin, Prevention of Transition Metal Dichalcogenide Photodegradation by Encapsulation with hBN Layers, *ACS Nano* **10**, 8973 (2016).
- [90] F. Cadiz, E. Courtade, C. Robert, G. Wang, Y. Shen, H. Cai, T. Taniguchi, K. Watanabe, H. Carrere, D. Lagarde, M. Manca, T. Amand, P. Renucci, S. Tongay, X. Marie, and B. Urbaszek, Excitonic Linewidth Approaching the Homogeneous Limit in MoS₂-Based van der Waals Heterostructures, *Phys. Rev. X* **7**, 021026 (2017).
- [91] M. Rath, C. Schott, J. Knippertz, M. Franke, Y.-R. Lin, A. Haags, M. Aeschlimann, C. Kumpf, and B. Stadtmüller, Growth, domain structure and atomic adsorption sites of hBN on the Ni(111) surface, *Phys. Rev. Mater.*, submitted (2019).
- [92] W. Auwärter, Hexagonal boron nitride monolayers on metal supports: Versatile templates for atoms, molecules and nanostructures, *Surf. Sci. Rep.* **74**, 1 (2019).
- [93] J. Felter, M. Rath, M. Franke, and C. Kumpf, In-situ Study of Two-Dimensional Dendritic Growth of Hexagonal Boron Nitride, *2D Materials* **6**, 045005 (2019).
- [94] I. Shimoyama, Y. Baba, T. Sekiguchi, and K. G. Nath, Formation of boron nitride ultra-thin films on Si(111), *Phys. Status Solidi C* **9**, 1450 (2012).
- [95] H.-C. Shin, Y. Jang, T.-H. Kim, J.-H. Lee, D.-H. Oh, S. J. Ahn, J. H. Lee, Y. Moon, J.-H. Park, S. J. Yoo, C.-Y. Park, D. Whang, C.-W. Yang, and J. R. Ahn, Epitaxial Growth of a Single-Crystal Hybridized Boron Nitride and Graphene Layer on a Wide-Band Gap Semiconductor, *J. Am. Chem. Soc.* **137**, 6897 (2015).
- [96] Y.-R. Lin, M. Franke, S. Parhizkar, M. Rath, V. W.-z. Yu, T.-L. Lee, S. Soubatch, V. Blum, F. S. Tautz, C. Kumpf, and F. C. Bocquet, Boron nitride on SiC(0001), *Phys. Rev. Materials* **6**, 064002 (2022).
- [97] F. C. Bocquet, Y.-R. Lin, M. Franke, N. Samiseresht, S. Parhizkar, S. Soubatch, T.-L. Lee, C. Kumpf, and F. S. Tautz, Surfactant-Mediated Epitaxial Growth of Single-Layer Graphene in an Unconventional Orientation on SiC, *Phys. Rev. Lett.* **125**, 106102 (2020).

- [98] K. Heinz, J. Bernhardt, J. Schardt, and U. Starke, Functional surface reconstructions of hexagonal SiC, *J. Phys.: Condens. Matter* **16**, S1705 (2004).
J. Zegenhagen and A. Kazimirov, The X-Ray Standing Wave Technique, Principles and Applications, in: Series on Synchrotron Radiation Techniques and Applications, World Scientific, (2013).
- [99] A. Catellani, M. Posternak, A. Baldereschi, and A. J. Freeman, Bulk and surface electronic structure of hexagonal boron nitride, *Phys. Rev. B* **36**, 6105 (1987).
- [100] Z. Liu, Y. Gong, W. Zhou, L. Ma, J. Yu, J. Carlos Idrobo, J. Jung, A. H. MacDonald, R. Vajtai, J. Lou, and P. M. Ajayan, Ultrathin high-temperature oxidation-resistant coatings of hexagonal boron nitride, *Nat. Commun.* **4**, 2541 (2013).
- [101] A. F. Rigosi, A. L. Levy, M. R. Snure, and N. R. Glavin, Turn of the decade: versatility of 2D hexagonal boron nitride, *J. Phys. Mater.* **4**, 032003 (2021).
- [102] J. Sforzini, M. Telychko, O. Krejčí, M. Vondráček, M. Švec, F. C. Bocquet, and F. S. Tautz, Transformation of metallic boron into substitutional dopants in graphene on 6H-SiC (0001), *Phys. Rev. B* **93**, 041302 (2016).
- [103] N. Ooi, V. Rajan, J. Gottlieb, Y. Catherine, and J. B. Adams, Structural properties of hexagonal boron nitride, *Model. Simul. Mater. Sc.* **14**, 515 (2006).
- [104] I. Forbeaux, J.-M. Themlin, and J.-M. Debever, Heteroepitaxial graphite on 6H-SiC(0001): Interface formation through conduction-band electronic structure, *Phys. Rev. B* **58**, 16396 (1998).
- [105] J. Sforzini, P. Hapala, M. Franke, G. van Straaten, A. Stöhr, S. Link, S. Soubatch, P. Jelínek, T.-L. Lee, U. Starke, M. Švec, F. C. Bocquet, and F. S. Tautz, Structural and Electronic Properties of Nitrogen-Doped Graphene, *Phys. Rev. Lett.* **116**, 126805 (2016).
- [106] M. Mantina, A. C. Chamberlin, R. Valero, C. J. Cramer and D. G. Truhlar, Consistent van der Waals Radii for the whole main group, *J. Phys. Chem. A* **113**, 19 (2013).
- [107] K. S. Novoselov, A. K. Geim, S. V. Morozov, D. Jiang, Y. Zhang, S. V. Dubonos, I. V. Grigorieva, A. A. Firsov, Electric Field Effect in Atomically Thin Carbon Films, *Science* **306**, 666 (2004).

-
- [108] L. Huder, A. Artaud, T. Le Quang, G. Trambly de Laissardi'ere, A. G. M. Jansen, G. Lapertot, C. Chapelier, and V. T. Renard, Electronic Spectrum of Twisted Graphene Layers under Heterostrain, *Phys. Rev. Lett.* **120**, 156405 (2018).
- [109] G. G. Naumis, S. Barraza-Lopez, M. Oliva-Leyva, and H. Terrones, Electronic and optical properties of strained graphene and other strained 2D materials: a review, *Prog. Phys.* **80**, 096501 (2017).
- [110] H. Kumar, D. Er, L. Dong, J. Li, and V. B. Shenoy, Elastic Deformations in 2D van der Waals Heterostructures and their Impact on Optoelectronic Properties: Predictions from a Multiscale Computational Approach, *Sci. Rep.* **5**, 10872 (2015).
- [111] T. E. Beechem, T. Ohta, B. Diaconescu, and J. T. Robinson, Rotational disorder in twisted bilayer graphene, *ACS Nano* **8**, 1655 (2014).
- [112] T. Stauber, T. Low, and G. Gómez-Santos, Chiral Response of Twisted Bilayer Graphene, *Phys. Rev. Lett.* **120**, 046801 (2018).
- [113] E. S. Morell, L. Chico, and L. Brey, Twisting dirac fermions: Circular dichroism in bilayer graphene, *2D Mater.* **4**, 035015 (2017).
- [114] C.-J. Kim, A. Sánchez-Castillo, Z. Ziegler, Y. Ogawa, C. Noguez, and J. Park, Chiral atomically thin films, *Nat. Nanotechnol.* **11**, 520 (2016).
- [115] A. O. Sboychakov, A. V. Rozhkov, A. L. Rakhmanov, and F. Nori, Externally Controlled Magnetism and Band Gap in Twisted Bilayer Graphene, *Phys. Rev. Lett.* **120**, 266402 (2018).
- [116] L. A. Gonzalez-Arraga, J. L. Lado, F. Guinea, and P. San-Jose, Electrically Controllable Magnetism in Twisted Bilayer Graphene, *Phys. Rev. Lett.* **119**, 107201 (2017).
- [117] A. V. Rozhkov, A. O. Sboychakov, A. L. Rakhmanov, and F. Nori, Single-electron gap in the spectrum of twisted bilayer graphene, *Phys. Rev. B* **95**, 045119 (2017).
- [118] J.-B. Liu, P.-J. Li, Y.-F. Chen, Z.-G. Wang, F. Qi, J.-R. He, B.-J. Zheng, J.-H. Zhou, W.-L. Zhang, L. Gu, and Y.-R. Li, Observation of tunable electrical bandgap in large-area twisted bilayer graphene synthesized by chemical vapor deposition, *Sci. Rep.* **5**, 15285 (2015).
- [119] A. R. Muniz and D. Maroudas, Opening and tuning of band gap by the formation of diamond superlattices in twisted bilayer graphene, *Sci. Rep.* **5**, 15285 (2015).

- [120] H. K. Pal, S. Spitz, and M. Kindermann, Emergent Geometric Frustration and Flat Band in Moiré Bilayer Graphene, *Phys. Rev. Lett.* **123**, 186402 (2019).
- [121] H. K. Pal, S. Carter, and M. Kindermann, Theory of Twisted Bilayer Graphene Near Commensuration, arXiv:1409.1971.
- [122] P. Moon, M. Koshino, and Y.-W. Son, Quasicrystalline electronic states in 30° rotated twisted bilayer graphene, *Phys. Rev. B* **99**, 165430 (2019).
- [123] M. J. Park, H. S. Kim, and S. Lee, Emergent localization in dodecagonal bilayer quasicrystals, *Phys. Rev. B* **99**, 245401 (2019).
- [124] W.-J. Zuo, J.-B. Qiao, D.-L. Ma, L.-J. Yin, G. Sun, J.-Y. Zhang, L.-Y. Guan, Scanning tunneling microscopy and spectroscopy of twisted trilayer graphene, *Phys. Rev. B* **97**, 035440 (2018).
- [125] Y. Murata, S. Nie, A. Ebnonnasir, E. Starodub, B. B. Kappes, K. F. McCarty, C. V. Ciobanu, and S. Kodambaka, Growth structure and work function of bilayer graphene on Pd(111), *Phys. Rev. B* **85**, 035440 (2012).
- [126] H. Peng, N. B. M. Schröter, J. Yin, H. Wang, T.-F. Chung, H. Yang, S. Ekahana, Z. Liu, J. Jiang, L. Yang, T. Zhang, C. Chen, H. Ni, A. Barinov, Y. P. Chen, Z. Liu, H. Peng, and Y. Chen, Substrate Doping Effect and Unusually Large Angle van Hove Singularity Evolution in Twisted Bi- and Multilayer Graphene, *Adv. Mater.* **29**, 1606741 (2017).
- [127] F. Hu, S. R. Das, Y. Luan, T.-F. Chung, Y. P. Chen, and Z. Fei, Real-Space Imaging of the Tailored Plasmons in Twisted Bilayer Graphene, *Phys. Rev. Lett.* **119**, 247402 (2017).
- [128] C.-C. Lu, Y.-C. Lin, Z. Liu, C.-H. Yeh, K. Suenaga, and P.-W. Chiu, Twisting bilayer graphene superlattices, *ACS Nano* **7**, 2587 (2013).
- [129] Z. Gao, Q. Zhang, C. H. Naylor, Y. Kim, I. H. Abidi, J. Ping, P. Ducos, J. Zauberman, M.-Q. Zhao, A. M. Rappe, Z. Luo, L. Ren, and A. T. C. Johnson, Crystalline bilayer graphene with preferential stacking from Ni-Cu gradient alloy, *ACS Nano* **12**, 2275 (2018).
- [130] S. Nie, A. L. Walter, N. C. Bartelt, E. Starodub, A. Bostwick, E. Rotenberg, and K. F. McCarty, Growth from Below: Graphene Bilayers on Ir(111), *ACS nano* **5**, 2298 (2011).
- [131] T. Iwasaki, A. A. Zakharov, T. Eelbo, M. Waśniowska, R. Wiesendanger, J. H. Smet, and U. Starke, Formation and structural analysis of twisted bilayer graphene on Ni(111) thin films, *Surf. Sci.* **625**, 44 (2014).

-
- [132] D. S. Lee, C. Riedl, T. Beringer, A. H. Castro Neto, K. von Klitzing, U. Starke, and J. H. Smet, Quantum Hall Effect in Twisted Bilayer Graphene, *Phys. Rev. Lett.* **107**, 216602 (2011).
- [133] A. Tejeda, A. Taleb-Ibrahimi, W. de Heer, C. Berger, and E. H. Conrad, Electronic structure of epitaxial graphene grown on the C-face of SiC and its relation to the structure, *New J. Phys.* **14**, 125007 (2012).
- [134] I. Razado-Colambo, J. Avila, J.-P. Nys, C. Chen, X. Wallart, M.-C. Asensio, and D. Vignaud, NanoARPES of twisted bilayer graphene on SiC: absence of velocity renormalization for small angles, *Sci. Rep.* **6**, 27261 (2016).
- [135] S. J. Ahn, P. Moon, T.-H. Kim, H.-W. Kim, H.-C. Shin, E. H. Kim, H. W. Cha, S.-J. Kahng, P. Kim, M. Koshino, Y.-W. Son, C.-W. Yang, and J. R. Ahn, Dirac electrons in a dodecagonal graphene quasicrystal, *Science* **361**, 782 (2018).
- [136] M. Conrad, F. Wang, M. Nevius, K. Jenkins, A. Celis, M. Narayanan Nair, A. Taleb-Ibrahimi, A. Tejeda, Y. Garreau, A. Vlad, A. Coati, P. F. Miceli, and E. H. Conrad, Wide Band Gap Semiconductor from a Hidden 2D Incommensurate Graphene Phase, *Nano Lett.* **17**, 341 (2017).
- [137] T. Schumann, M. Dubsloff, M. H. Oliveira, Jr., M. Hanke, J. M. J. Lopes, and H. Riechert, Effect of buffer layer coupling on the lattice parameter of epitaxial graphene on SiC(0001), *Phys. Rev. B* **90**, 041403 (2014).
- [138] M. S. Nevius, M. Conrad, F. Wang, A. Celis, M. N. Nair, A. Taleb-Ibrahimi, A. Tejeda, and E. H. Conrad, Semiconducting Graphene from Highly Ordered Substrate Interactions, *Phys. Rev. Lett.* **115**, 136802 (2015).
- [139] E. Koren and U. Duerig, Superlubricity in quasicrystalline twisted bilayer graphene, *Phys. Rev. B* **93**, 201404 (2016).
- [140] G. Mercurio, O. Bauer, M. Willenbockel, N. Fairley, W. Reckien, C. H. Schmitz, B. Fiedler, S. Soubatch, T. Bredow, M. Sokolowski, and F. S. Tautz, Adsorption height determination of nonequivalent C and O species of PTCDA on Ag(110) using x-ray standing waves, *Phys. Rev. B* **87**, 045421 (2013).
- [141] N. Fairley, CasaXPS, version 2.3.19PR1.0, Casa Software Ltd, Bay House, 5 Grosvenor Terrace, Teignmouth, Devon TQ14 8NE, United Kingdom

- [142] L. Nemeč, V. Blum, P. Rinke, and M. Scheffler, Thermodynamic Equilibrium Conditions of Graphene Films on SiC, *Phys. Rev. Lett.* **111**, 065502 (2013).
- [143] A. J. Van Bommel, J. E. Crombeen, and A. Van Tooren, LEED and Auger electron observations of the SiC(0001) surface, *Surf. Sci.* **48**, 463 (1975).
- [144] K. V. Emtsev, F. Speck, T. Seyller, L. Ley, and J. D. Riley, Interaction, growth, and ordering of epitaxial graphene on SiC0001 surfaces: A comparative photoelectron spectroscopy study, *Phys. Rev. B* **77**, 155303 (2008).
- [145] J. B. Hannon, M. Copel, and R. M. Tromp, Direct Measurement of the Growth Mode of Graphene on SiC(0001) and SiC(000 $\bar{1}$), *Phys. Rev. Lett.* **107**, 166101 (2011).
- [146] K. V. Emtsev, A. Bostwick, K. Horn, J. Jobst, G. L. Kellogg, L. Ley, J. L. McChesney, T. Ohta, S. A. Reshanov, J. Röhl, E. Rotenberg, A. K. Schmid, D. Waldmann, H. B. Weber, and T. Seyller, Towards wafer-size graphene layers by atmospheric pressure graphitization of silicon carbide, *Nat. Mater.* **8**, 203 (2009).
- [147] A. Mattausch and O. Pankratov, Ab Initio Study of Graphene on SiC, *Phys. Rev. Lett.* **99**, 076802 (2007).
- [148] T. Ohta, A. Bostwick, J. L. McChesney, T. Seyller, K. Horn, and E. Rotenberg, Interlayer Interaction and Electronic Screening in Multilayer Graphene Investigated with Angle-Resolved Photoemission Spectroscopy, *Phys. Rev. Lett.* **98**, 206802 (2007).
- [149] F. Speck, J. Jobst, F. Fromm, M. Ostler, D. Waldmann, M. Hundhausen, H. B. Weber, and T. Seyller, The quasi-free-standing nature of graphene on H-saturated SiC(0001), *Appl. Phys. Lett.* **99**, 122106 (2011).
- [150] J. Ristein, S. Mammadov, and T. Seyller, Origin of Doping in Quasi-Free-Standing Graphene on Silicon Carbide, *Phys. Rev. Lett.* **108**, 246104 (2012).
- [151] S. Mammadov, J. Ristein, R. J. Koch, M. Ostler, C. Raidel, M. Wanke, R. Vasiliauskas, R. Yakimova, and T. Seyller, Polarization doping of graphene on silicon carbide, *2D Mater.* **1**, 035003 (2014).
- [152] J. Sławińska, H. Aramberria, M. C. Muñoz, and J. I. Cerdá, Ab initio study of the relationship between spontaneous polarization and p-type

- doping in quasi-freestanding graphene on H-passivated SiC surfaces, *Carbon* **93**, 88 (2015).
- [153] G. Profeta, M. Calandra, and F. Mauri, Phonon-mediated superconductivity in graphene by lithium deposition, *Nat. Phys.* **8**, 131 (2012).
- [154] Y. Sohn, S. W. Jung, F. Göhler, W. J. Shin, S. Cha, T. Seyller, and K. S. Kim, Electronic band structure of Bi-intercalate layers in graphene and SiC(0001), *J. Korean Phys. Soc.* **78**, 157 (2021).
- [155] C. Xia, S. Watcharinyanon, A. A. Zakharov, R. Yakimova, L. Hultman, L. I. Johansson, and C. Virojanadara, Si intercalation/deintercalation of graphene on 6H-SiC(0001), *Phys. Rev. B* **85**, 045418 (2012).
- [156] P. Rosenzweig, H. Karakachian, S. Link, K. Küster, and U. Starke, Tuning the doping level of graphene in the vicinity of the Van Hove singularity via ytterbium intercalation, *Phys. Rev. B* **035445**, 100 (2019).
- [157] S. Runte, P. Lazić, Chi V.-V., J. Coraux, J. Zegenhagen, and C. Busse, Graphene buckles under stress: An x-ray standing wave and scanning tunneling microscopy study, *Phys. Rev. B* **89**, 155427 (2014).
- [158] C. C. Silva, M. Iannuzzi, D. A. Duncan, P. T. P. Ryan, K. T. Clarke, J. T. Küchle, J. Cai, W. Jolie, C. Schlueter, T.-L. Lee, and C. Busse, Valleys and Hills of Graphene on Ru(0001), *J. Phys. Chem. C* **122**, 18554 (2018).
- [159] C. C. Silva, J. Cai, W. Jolie, D. Dombrowski, F. H. Farwick zum Hagen, A. J. Martínez-Galera, C. Schlueter, T.-L. Lee, and C. Busse, Lifting Epitaxial Graphene by Intercalation of Alkali Metals, *J. Phys. Chem. C* **123**, 13712 (2019).
- [160] S. Weiß, D. Gerbert, A. Stein, A. K. Schenk, X. Yang, C. Brülke, R. Kremring, S. Feldmann, F. C. Bocquet, M. Gille, S. Hecht, M. Sokolowski, P. Tegeder, S. Soubatch, and F. S. Tautz, Dependence of the adsorption height of graphenelike adsorbates on their dimensionality, *Phys. Rev. B* **98**, 075410 (2018).
- [161] J. Sforzini, L. Nemeč, T. Denig, B. Stadtmüller, T.-L. Lee, C. Kumpf, S. Soubatch, U. Starke, P. Rinke, V. Blum, F. C. Bocquet, and F. S. Tautz, Approaching Truly Freestanding Graphene: The Structure of Hydrogen-Intercalated Graphene on 6H-SiC(0001), *Phys. Rev. Lett.* **114**, 106804 (2015).
- [162] Y.-R. Lin, S. Wolff, P. Schädlich, M. Hutter, S. Soubatch, T.-L. Lee, F. S. Tautz, T. Seyller, C. Kumpf, and F. C. Bocquet, Vertical structure of

- Sb-intercalated quasifreestanding graphene on SiC(0001), *Phys. Rev. B* **106**, 155418 (2022).
- [163] M. Ostler, F. Speck, M. Gick, and T. Seyller, Automated preparation of high-quality epitaxial graphene on 6H-SiC(0001), *Phys. Status Solidi B* **247**, 2924 (2010).
- [164] The latest version of the open-source software TORRICELLI is available at www.torricelli-software.com.
- [165] I. A. Vartanyants and J. Zegenhagen, Theory of photoelectron emission from an X-ray interference field: The X-ray Standing Wave Technique, WorldScientific, pp. 181–215, (2013)
- [166] T. J. Reber, N. C. Plumb, J. A. Waugh, and D. S. Dessau, Effects, determination, and correction of count rate nonlinearity in multi-channel analog electron detectors, *Rev. Sci. Instrum.* **85**, 043907 (2014).
- [167] P. Pyykkö and M. Atsumi, Molecular Single-Bond Covalent Radii for Elements 1–118, *Chem. Eur. J.* **15**, 186 (2008).
- [168] G. Becker, H. Freudenblum, and C. Witthauer, Trimethylsilylverbindungen der Vb-Elemente. VI. Synthese, Molekül- und Kristallstruktur des Tetrakis(trimethylsilyl)distibans im Vergleich mit Tetraphenyldistiban, *Z. Anorg. Allg. Chem.* **492**, 37 (1982).
- [169] M. Mantina, A. C. Chamberlin, R. Valero, C. J. Cramer, and D. G. Truhlar, Consistent van der Waals Radii for the Whole Main Group, *J. Phys. Chem. A* **113**, 5806 (2013).
- [170] C.-H. Hsu, V. Ozolins, and F.-C. Chuang, First-principles study of Bi and Sb intercalated graphene on SiC(0001) substrate, *Surf. Sci.* **616**, 149 (2013).
- [171] S. Nakatani, A. Saito, Y. Kuwahara, T. Takahashi, M. Aono, and S. Kikuta, Study of the Si(111) $\sqrt{3} \times \sqrt{3}$ -Sb Structure by X-Ray Diffraction, *Jpn. J. Appl. Phys.* **31**, L426 (1992).
- [172] Y.-R. Lin, M. Bagchi, S. Soubatch, T.-L. Lee, J. Brede, F. C. Bocquet, C. Kumpf, Y. Ando, and F. S. Tautz, Vertical position of Sr dopants in the $Sr_xBi_2Se_3$ superconductor, *Phys. Rev. B* **104**, 054506 (2021).
- [173] L. Fu and E. Berg, Odd-Parity Topological Superconductors: Theory and Application to $Cu_xBi_2Se_3$, *Phys. Rev. Lett.* **105**, 097001 (2010).

-
- [174] K. Matano, M. Kriener, K. Segawa, Y. Ando, and G. Zeng, Spin-rotation symmetry breaking in the superconducting state of $\text{Cu}_x\text{Bi}_2\text{Se}_3$, *Nat. Phys.* **12**, 852 (2016).
- [175] R. Tao, Y.-J. Yan, X. Liu, Z.-W. Wang, Y. Ando, Q.-H Wang, T. Zhang, and D.-L. Feng, Direct Visualization of the Nematic Superconductivity in $\text{Cu}_x\text{Bi}_2\text{Se}_3$, *Phys. Rev. X* **8**, 041024 (2018).
- [176] S. Yonezawa, K. Tajiri, S. Nakata, Y. Nagai, Z. Wang, K. Segawa, Y. Ando, and Y. Maeno, Thermodynamic evidence for nematic superconductivity in $\text{Cu}_x\text{Bi}_2\text{Se}_3$, *Nat. Phys.* **13**, 123 (2017).
- [177] A. Y. Kuntsevich, M. A. Bryzgalov, V. A. Prudkoglyad, V. P. Martovitskii, Y. G. Selivanov, and E. G. Chizhevskii, Structural distortion behind the nematic superconductivity in $\text{Sr}_x\text{Bi}_2\text{Se}_3$, *New J. Phys.* **20**, 103022 (2018).
- [178] S. Yonezawa, Nematic Superconductivity in Doped Bi_2Se_3 Topological Superconductors, *Condens. Matter* **4**, 2 (2019).
- [179] M. Sato and Y. Ando, Topological superconductors: a review, *Reports on Progress in Physics* **80**, 076501 (2017).
- [180] L. Andersen, A. Ramires, Z. Wang, T. Lorenz, Y. Ando, Generalized Anderson's theorem for superconductors derived from topological insulators, *Sci. Adv.* **6**, eaay6502 (2020).
- [181] Z. Liu, X. Yao, J. Shao, M. Zuo, L. Pi, S. Tan, C. Zhang, and Y. Zhang, Superconductivity with Topological Surface State in $\text{Sr}_x\text{Bi}_2\text{Se}_3$, *J. Am. Chem. Soc.* **137**, 10512 (2015).
- [182] S. Urazhdin, D. Bilc, S. H. Tessmer, S. D. Mahanti, T. Kyratsi, and M. G. Kanatzidis, Scanning tunneling microscopy of defect states in the semiconductor Bi_2Se_3 , *Phys. Rev. B* **66**, 161306(R) (2002).
- [183] Note that a proper correction of non-dipolar effects in XSW can only be performed for PE from an s-state [79, 81, 165]. Therefore, only for the Se 3s photoemission yield was this correction performed, using the correction parameters $\gamma = 0.104$ and $\Delta = -1.008$. For Bi 5d and Sr 3d, values which are only corrected for the polarization factor that differs slightly from unity due to the deviation from exact normal incidence (by $\xi = 3.5^\circ$) were given. The angle between the direction of photoelectron emission and the incident synchrotron beam was $\phi = 80.9^\circ$. For details on the calculation of non-dipolar correction factors S_R and S_I (see Eq. 2.21) from the parameters γ and Δ , see van Straaten *et al.* [81].

- [184] R. A. J. Woolley, C. P. Martin, G. Miller, V. R. Dhanak, P. J. Moriarty, Adsorbed molecular shuttlecocks: An NIXSW study of Sn phthalocyanine on Ag(111) using Auger electron detection, *Surface Science* **601**, 1231 (2007).
- [185] S. Duhm, C. Bürker, J. Niederhausen, I. Salzmann, T. Hosokai, J. Duvernay, S. Kera, F. Schreiber, N. Koch, N. Ueno, and A. Gerlach, Pentacene on Ag(111): Correlation of Bonding Distance with Intermolecular Interaction and Order, *Appl. Mater. Interfaces* **5**, 9377 (2013).
- [186] B. Stadtmüller, D. Lüftner, M. Willenbockel, E.M. Reinisch, T. Sueyoshi, G. Koller, S. Soubatch, M.G. Ramsey, P. Puschnig, F.S. Tautz, C. Kumpf, Unexpected interplay of bonding height and energy level alignment at heteromolecular hybrid interfaces, *Nature Communications* **5**, 3685 (2014).
- [187] B. Stadtmüller, S. Schröder, C. Kumpf, Heteromolecular metal-organic interfaces: Electronic and structural fingerprints of chemical bonding, *J. Electron Spectrosc. Relat. Phenom.* **204 A**, 80 (2015).
- [188] E. Goiri, M. Matena, A. El-Sayed, J. Lobo-Checa, P. Borghetti, C. Rogero, B. Detlefs, J. Duvernay, J. E. Ortega, and D. G. de Oteyza, Self-Assembly of Bicomponent Molecular Monolayers: Adsorption Height Changes and Their Consequences, *Phys. Rev. Lett.* **112**, 117602 (2014).
- [189] G. Mercurio, R. J. Maurer, S. Hagen, F. Leyssner, J. Meyer, P. Tegeder, S. Soubatch, K. Reuter, and F. S. Tautz, X-ray standing wave simulations based on Fourier vector analysis as a method to retrieve complex molecular adsorption geometries, *Front. Phys.* **2**, 2 (2014).
- [190] A. Baby, M. Gruenewald, C. Zwick, F. Otto, R. Forker, G. van Straaten, M. Franke, B. Stadtmüller, C. Kumpf, G.-P. Brivio, G. Fratesi, T. Fritz, E. Zojer, Fully Atomistic Understanding of the Electronic and Optical Properties of a Prototypical Doped Charge-Transfer Interface, *ACS Nano* **11**, 10945 (2017).
- [191] B. Stadtmüller, J. Seidel, N. Haag, L. Grad, C. Tusche, G. van Straaten, M. Franke, J. Kirschner, C. Kumpf, M. Cinchetti, M. Aeschlimann, Modifying the Surface of a Rashba-Split Pb-Ag Alloy Using Tailored Metal-Organic Bonds, *Phys. Rev. Lett.* **117**, 096805 (2016).
- [192] P.J. Blowey, A. Haags, L.A. Rochford, J. Felter, D.A. Warr, D.A. Duncan, T.-L. Lee, G. Costantini, C. Kumpf, D.P. Woodruff, Characterization of growth and structure of TCNQ phases on Ag(111), *Phys. Rev. Materials* **3**, 116001 (2019).

-
- [193] B. P. Klein, N. J. van der Heijden, S. R. Kachel, M. Franke, C. K. Krug, K. K. Greulich, L. Ruppenthal, P. Müller, P. Rosenow, S. Parhizkar, F. C. Bocquet, M. Schmid, W. Hieringer, R. J. Maurer, R. Tonner, C. Kumpf, I. Swart, and J. M. Gottfried, Molecular Topology and the Surface Chemical Bond: Alternant Versus Nonalternant Aromatic Systems as Functional Structural Elements, *Phys. Rev. X* **9**, 011030 (2019).
- [194] G. J. Paez, C. N. Singh, M. J. Wahila, K. E. Tirpak, N. F. Quackenbush, S. Sallis, H. Paik, Y. Liang, D. G. Schlom, T.-L. Lee, C. Schlueter, W.-C. Lee, and L. F. J. Piper, Simultaneous Structural and Electronic Transitions in Epitaxial VO₂/TiO₂(001), *Phys. Rev. Lett.* **124**, 196402 (2020).
- [195] J. S. Gibson, K. L. Syres, M. Buckley, T.-L. Lee, P. K. Thakur, and R. G. Jones, Thin film structural analysis using variable-period x-ray standing waves, *Phys. Rev. B* **98**, 165402 (2018).
- [196] H. Shinotsuka, S. Tanuma, C. J. Powell, and D. R. Penn, Calculations of electron inelastic mean free paths. XII. Data for 42 inorganic compounds over the 50 eV to 200 keV range with the full Penn algorithm, *Surf. Interface Anal.* **51**, 427 (2019).
- [197] S. Roy, H. L. Meyerheim, K. Mohseni, A. Ernst, M. M. Otrokov, M. G. Vergniory, G. Mussler, J. Kampmeier, D. Grützmacher, C. Tusche, J. Schneider, E. V. Chulkov, and J. Kirschner, Atomic relaxations at the (0001) surface of Bi₂Se₃ single crystals and ultrathin films, *Phys. Rev. B* **90**, 155456 (2014).
- [198] T. Komatsu, K. Imai, K. Matusita, M. Takata, Y. Iwai, A. Kawakami, Y. Kaneko, and T. Yamashita, Liquid Quenched Superconductor Ba-Y-Cu-O with $T_{C,zero} = 88$ K and AC Josephson Effect at 77 K, *Jpn. J. Appl. Phys.* **26**, L1148 (1987).
- [199] T. Komatsu, K. Imai, K. Matusita, M. Ishii, M. Takata, and T. Yamashita, Crystalline Phases in Superconductor Ba-Y-Cu-O with High T_c Prepared by Melting Method, *Jpn. J. Appl. Phys.* **26**, L1272 (1987).
- [200] T. Komatsu, K. Imai, R. Sato, K. Matusita, and T. Yamashita, Preparation of High-T_c Superconducting Bi-Ca-Sr-Cu-O Ceramics by the Melt Quenching Method, *Jpn. J. Appl. Phys.* **27**, L533 (1988).
- [201] T. Komatsu, R. Sato, K. Imai, K. Matusita, and T. Yamashita, High-T_c Superconducting Glass Ceramics Based on the Bi-Ca-Sr-Cu-O System, *Jpn. J. Appl. Phys.* **27**, L550 (1988).

Band / Volume 85

Dynamical and statistical structure of spatially organized neuronal networks

M. Layer (2022), xiii, 167 pp

ISBN: 978-3-95806-651-9

Band / Volume 86

Persistent firing and oscillations in the septo-hippocampal system and their relation to locomotion

K. Korvasová (2022), 111 pp

ISBN: 978-3-95806-654-0

Band / Volume 87

Sol-Gel-Synthese, Tintenstrahldruck und Blitzlampentemperung von Tantaloxid-Dünnschichten zur pH-Messung

C. D. Beale (2022), xlix, 339 pp

ISBN: 978-3-95806-656-4

Band / Volume 88

Diversity of chiral magnetic solitons

V. Kuchkin (2022), xiv, 155 pp

ISBN: 978-3-95806-665-6

Band / Volume 89

Controlling the electrical properties of oxide heterointerfaces through their interface chemistry

M.-A. Rose (2022), vi, 162 pp

ISBN: 978-3-95806-667-0

Band / Volume 90

Modeling and Suppressing Unwanted Parasitic Interactions in Superconducting Circuits

X. Xu (2022), 123, XVIII pp

ISBN: 978-3-95806-671

Band / Volume 91

Activating molecular magnetism by controlled on-surface coordination.

Cojocariu (2022), xi, 169 pp

ISBN: 978-3-95806-674-8

Band / Volume 92

Computational study of structural and optical properties of two-dimensional transition-metal dichalcogenides with implanted defects

S. H. Rost (2023), xviii, 198 pp

ISBN: 978-3-95806-682-3

Band / Volume 93

DC and RF characterization of bulk CMOS and FD-SOI devices at cryogenic temperatures with respect to quantum computing applications

A. Artanov (2023), xv, 80, xvii-liii pp

ISBN: 978-3-95806-687-8

Band / Volume 94

HAXPES study of interface and bulk chemistry of ferroelectric HfO₂ capacitors

T. Szyjka (2023), viii, 120 pp

ISBN: 978-3-95806-692-2

Band / Volume 95

A brain inspired sequence learning algorithm and foundations of a memristive hardware implementation

Y. Bouhadjar (2023), xii, 149 pp

ISBN: 978-3-95806-693-9

Band / Volume 96

Characterization and modeling of primate cortical anatomy and activity

A. Morales-Gregorio (2023), ca. 260 pp.

ISBN: 978-3-95806-698-4

Band / Volume 97

Hafnium oxide based memristive devices as functional elements of neuromorphic circuits

F. J. Cüppers (2023), vi, ii, 214 pp

ISBN: 978-3-95806-702-8

Band / Volume 98

Simulation and theory of large - scale cortical networks

A. van Meegen (2023), ca. 250 pp

ISBN: 978-3-95806-708-0

Band / Volume 99

Structure of two-dimensional multilayers and topological superconductors: surfactant mediated growth, intercalation, and doping

Y.-R. Lin (2023), x, 111 pp

ISBN: 978-3-95806-716-5

Information

Band / Volume 99

ISBN 978-3-95806-716-5

Mitglied der Helmholtz-Gemeinschaft

